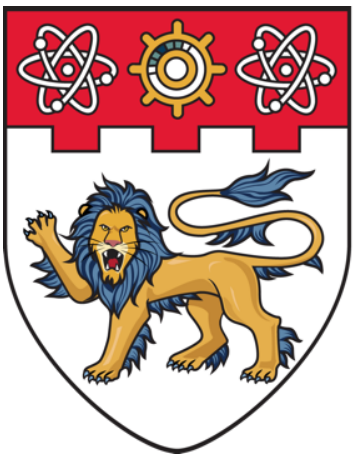

NANYANG TECHNOLOGICAL UNIVERSITY

SINGAPORE

INVESTIGATIONS INTO HIGH RESOLUTION IMAGING OF THE AQUEOUS OUTFLOW SYSTEM AND CORNEA

HONG XUN JIE JESMOND

SCHOOL OF MECHANICAL AND AEROSPACE ENGINEERING

2017

INVESTIGATIONS INTO HIGH RESOLUTION IMAGING OF THE AQUEOUS OUTFLOW SYSTEM AND CORNEA

HONG XUN JIE JESMOND

School of Mechanical and Aerospace Engineering

A thesis submitted to the Nanyang Technological University
in partial fulfilment of the requirement for the degree of
Doctor of Philosophy

2017

Acknowledgements

This research project is the culmination of years of hard work and dedication. The journey albeit tough has been a fruitful one and is only achievable with the assistance and kind support of many individuals.

My deepest gratitude goes out to my supervisor, Associate Professor Murukeshan Vadakke Matham, for giving me the opportunity to work on this project. He presented me with numerous learning opportunities and also gave me the autonomy to work. Under his guidance, I have gained immense knowledge and exposure on the various optical systems. For his mentorship, I will always be grateful.

Special mention goes out to every member of the research group for I am thankful for their advice and constructive criticism. Their support throughout the course of this research project has made the process more enjoyable.

I would also like to express my sincere gratitude to the collaborators from Singapore Eye Research Institute and A*STAR Institute for Infocomm Research for their patience and hard work in entertaining my requests. I am appreciative for their truthful and illuminating views on issues related to the project. In addition, it is important to acknowledge the financial support received through the A*STAR-SERC grant (No. 112 148 0003), and the research manpower and facilities provided through the COLE-EDB funding at the Center for Optical and Laser Engineering, Nanyang Technological University.

Honorary mentions to my family and friends for their unwavering support and encouragement. Their belief allowed me to stay unfazed even in the most arduous of situations.

Last but not least, my heartfelt appreciation to Sherlyn for being my co-pilot in life, for all deviations that life may present.

Abstract

Advance imaging modalities are necessary for the accurate and early detection of glaucoma and corneal diseases. It enables vision researchers and clinicians to understand the disease state fundamentals and pathology, which are critical for follow-up and subsequent treatment. Timely and definitive diagnosis of ocular diseases, coupled with the mobilization of public health resources to create an increase in awareness for its prevention through innovative programs, is believed to have a positive impact on the global burden of visual disability. This is especially true in the case of glaucoma, where the aim of the treatment is to preserve the remaining vision.

This thesis in this context aims to investigate the potential of Bessel beam and light sheet fluorescence microscopy for ocular disease diagnosis. The main objectives of this thesis are hence directed towards the research and development of novel concepts and methodologies using Bessel beam microscopy and light sheet fluorescence microscopy for high resolution diagnostic monitoring of open and close angle in glaucoma patients. With innovative optical engineering of the light sheet configuration, the illumination arm can be used for high resolution imaging and characterization of cornea. A flexible ocular imaging probe to record, capture, and display images of the iridocorneal angle region and fundus is also looked into.

A flexible ocular imaging probe with uniform near field irradiance is conceptualized and developed based on a geometric model that simplifies the complex non-rotational symmetric irradiance distribution of light emitting diodes tilted at an angle. The imaging probe is an assembly of a circular ring array of four light emitting diodes tilted at an angle and a micro color charged coupled device camera. Its distal end is optimized and custom fabricated, following a

theoretical analysis and modelling of the design parameters. It can be used to image critical anatomical structures of the aqueous outflow system and fundus. The imaging probe has resolutions of 10.08 line pairs per mm (~49.61 μm) at the iridocorneal angle region and 5.04 line pairs per mm (~99.21 μm) at the fundus. The use of near infrared sources for dark room provocation test enables a predictive and objective evaluation for detecting iridocorneal angle closure. The flexible ocular imaging probe can differentiate an open angle from a closed angle and note other pathological conditions, hence allowing proper classification and appropriate management. It has a better safety profile, is easier to implement, and reduces image acquisition time and patient discomfort as compared to conventional photographic methods such as gonioscopy and RetCam.

A digitally scanned Bessel-Gauss light sheet fluorescence microscopy system to image the trabecular meshwork is proposed and developed. It is able to overcome the trade-off between the length and thickness of Gaussian light sheet to give better imaging performance. It has adequate spatial resolution to resolve the trabecular meshwork structures, thereby providing objective information about the aqueous outflow system and critical anatomical structures inside the eye. The higher axial resolution of this prototype is due to the thinner light sheet, and the ability of the Bessel-Gauss beam to reconstruct through scattering media. Images acquired are in sharp focus since the light sheet is thinner than the depth of field of the detection objective. The unique ability of the Bessel-Gauss beam to reconstruct itself also increases the image contrast at the trabecular meshwork, and minimizes the scattering and shadowing artifacts. The use of fluorescein sodium as a contrast agent further increases the anatomical discrimination and image contrast in the optical sections. The digitally scanned Bessel-Gauss light sheet fluorescence

microscopy system has cellular/ subcellular spatial resolution, good optical sectioning, high imaging speed, and low photobleaching and photodamage. An indirect axicon assisted gonioscopy imaging system is also proposed and developed by integrating the concept of Bessel beam microscopy with conventional gonioscopy imaging. The proposed system can image with a spatial resolution of 3 μm and can reveal critical details of the trabecular meshwork. It is expected to aid the management of glaucoma by providing information complementary to angle photography and gonioscopy. Assessment and evaluation of trabecular meshwork pigmentation is critical in many protocols and grading techniques for glaucoma. Theoretical modelling, simulations, and experimental studies were performed for both configurations.

Further, a methodology and integrated apparatus for the sequential imaging of the cornea and aqueous outflow system is configured, based on a Gaussian beam epi-illumination configuration and a Bessel-Gauss beam plane illumination configuration, respectively. The cornea imaging module has a spatial resolution of ~2.19 μm and can be used for high resolution imaging and characterization of cornea. Corneal topography is achieved by moving the scanning spot across eye in a raster fashion. The ability of the proposed configuration to provide cellular level resolution potentially enables identification and characterization of infectious agent during an inflammatory response. Vision researchers and clinicians can therefore classify the disease states without the need to mechanically remove samples from the cornea. The clinical significance of the proposed study is validated by performing imaging of the New Zealand white rabbit's cornea infected with *Pseudomonas*.

It is envisaged that the original contributions and major findings of this thesis can contribute towards the diagnosis, prognosis, and management of glaucoma and corneal diseases.

Table of contents

List of figures

List of tables

List of symbols

Symbols	Description
α	Illumination angle of light emitting diode
β	Numerical aperture of plano-convex axicon lens
γ	Physical angle of plano-convex axicon lens
λ	Wavelength
δ	Light sheet thickness
θ	Angular substense
θ_{LED}	LED viewing angle
$\theta_{LED\ 1/2}$	Half viewing angle of light emitting diode
A_{LED}	Light emitting diode emitting area
b	Confocal parameter
D	Degree to which the point spread function is focused or defocused
D_a	Aperture diameter
d_{min}	Minimum resolvable distance between two point sources
d_{PSF}	Diameter of point spread function
$d_{spot\ size}$	Diffraction limited spot size of a single lens system
$d^{\infty}_{spot\ size}$	Diffraction limited spot size of an infinity corrected system
E	Irradiance
$f^{\#}$	*f*-number

I	Light intensity
I_E	Radiant intensity
I_V	Luminous intensity
J_0	Zero-order Bessel beam
L	Distance between plano-convex axicon lens and camera
L_{LED}	Radiance of light emitting diode
l	Working distance of circular ring array of light emitting diode
M	Magnification
n	Refractive index
R	Radius of curvature
R_{ill}	Radius of illumination beam
R_{det}^{axial}	Axial resolution of detection objective lens
R_{LSFM}^{axial}	Axial resolution of light sheet fluorescence microscopy
$R_{LSFM}^{lateral}$	Lateral resolution of light sheet fluorescence microscopy
r	Circular ring array radius
r_0	Maximally flat condition for circular ring array
s	Distance between two linear light emitting diodes
s_i	Image distance
s_o	Object distance
w_0	Beam waist radius
x	Spatial coordinate
y	Spatial coordinate

z	Spatial coordinate
z_D	Depth of focus of plano-convex axicon lens
z_R	Rayleigh range

List of abbreviations

Abbreviation	Explanation
2D	Two dimensional
3D	Three dimensional
ACA	Anterior chamber angle
ACD	Anterior chamber depth
ACV	Anterior chamber volume
AOD	Angle opening distance
AOS	Aqueous outflow system
ARA	Angle recess area
AS-OCT	Anterior segment optical coherence tomography
ATA	Angle-to-angle
CBB	Ciliary body band
CC	Collector channels
CCD	Charge-coupled device
CCT	Central corneal thickness
CLR	Crystalline lens rise
CT	Computerized tomography
DOF	Depth of field
DSLM	Digitally scanned laser light sheet fluorescence microscopy
FD-OCT	Fourier domain optical coherence tomography

FOV	Field of view
GRIN	Gradient-index
ICA	Iridocorneal angle
IOP	Intra-ocular pressure
ITC	Iris-trabecular contact
LSCM	Laser scanning confocal microscopy
LSFM	Light sheet fluorescence microscopy
LSM	Laser scanning microscopy
MPE	Maximum permissible exposure
MPM	Muiti-photon microscopy
MRI	Magnetic resonance imaging
NA	Numerical aperture
NIR	Near infrared
OCPI	Objective-coupled planar illumination
OCT	Optical coherence tomography
OPFOS	Orthogonal-plane fluorescence optical sectioning microscopy
OPM	Oblique plane microscopy
OTF	Optical transfer function
PA	Photoacoustic
ROI	Region of interest
SC	Schlemm’s canal
sCMOS	scientific complementary metal-oxide semiconductor

SD-OCT	Spectral domain optical coherence tomography
SL	Schwalbes' line
SNR	Signal-to-noise ratio
SPIM	Selective plane illumination microscopy
SS	Scleral spur
SS-OCT	Swept source optical coherence tomography
TICL	Trabecular-iris contact length
TISA	Trabecular-iris space area
TLSM	Thin laser light sheet microscopy
TM	Trabecular meshwork
UBM	Ultrasound biomicroscopy

Chapter 1: Introduction

This chapter begins with the background and motivation for undertaking this research project. It consists of a brief review on the various types of ocular imaging instruments for the diagnosis and management of glaucoma and corneal diseases. A short note on the limitations of the current state of art medical technology will be discussed. The main objectives of this doctoral research will then be identified. The scope of this project is defined in contemplation of fulfilling the desired objectives and is summarized in a research roadmap. This chapter concludes with the organization of the thesis.

1.1 Background

Biomedical research focuses mainly on the diagnosis, prognosis and management of diseases, which ultimately enhances the patients' quality of life, and reduces the disease burden. Super-resolution imaging and ultra-sensitive detection methodologies are changing the treatment landscape into an era of cutting-edge technologies. In clinical ophthalmology for example, advance imaging modalities based on confocal, interferometry, Scheimpflug imaging, slit-scanning, and ultrasound generally allow early and accurate detection of ocular related diseases such as glaucoma and corneal diseases. These imaging modalities are capable of providing vision researchers and clinicians with quantitative and qualitative data, which are essential for subsequent treatment and follow-up procedures. Each of these imaging modalities has particular benefits and associated drawbacks in obtaining reliable and repeatable measurements. These imaging modalities are valuable and complement each other in clinical practice, particularly when one technique is hard to apply or the obtained results are doubtful.

Amongst the imaging methodologies, non-ionizing radiation based optical techniques for measurements are considered to be the most sensitive. They are more appealing because of its obvious advantages of being non-ionizing, non-invasive, highly accurate, resistance to electromagnetic interference, and the ability for whole field measurements. These attributes make them indispensable for the different kinds of measurements in biomedical research. The visualization capabilities of the various optical imaging techniques for glaucoma and corneal assessment can be broadly classified into medical photographic and optical tomographic methods as shown in Table 1.1.

Table.1.1: Ocular instruments for glaucoma and corneal assessment.

Instrument	**Scan source**	**Measuring principle**
Optical tomographic method		
Optical coherence tomography (OCTs) [1-3]	SLD 840 nm - 1310 nm	Interferometry
Scanning laser ophthalmoscopy [4]	Laser diode at 670 nm	Confocal
Ultrasound biomicroscopy (UBM) [5]	Ultrasound (50 MHz)	Ultrasound
Medical photographic method		
Gonioscopy [6]	Visible light	Goniophotography
Pentacam [7]	Blue LED 470 nm	Scheimpflug imaging
Orbscan II [7]	White flash light	Slit-scanning imaging

Glaucoma is an eye disease with characteristic optic nerve damage, resulting in the irreversible loss of vision. Most, but not all of these diseases are characterized by an increased in the intra-ocular pressure (IOP) [8]. Based on a global study on visual impairment, glaucoma is one of the leading causes of blindness, second only to cataracts [9]. Critical clinical hallmarks of glaucoma include an increase in IOP, visual field defects, and the irreversible loss of vision. Glaucoma therapeutic intervention primarily aims at the lowering of IOP and subsequent investigation into the related abnormalities in the aqueous outflow system (AOS). Hence, the ability to visualize the iridocorneal angle (ICA) region comprising the Schlemm's canal (SC),

trabecular meshwork (TM), and collector channel (CC), in high resolution, is extremely valuable to clinicians and vision researchers towards understanding the disease condition. It can allow the effective evaluation and management of glaucoma. Corneal disease is also one of the leading causes of blindness worldwide, together with cataract and glaucoma [9, 10]. It has a complicated epidemiology which includes an extensive variation of infectious and inflammatory eye diseases such as viral, bacterial, or fungal keratitis that result in corneal scarring, eventually leading to functional blindness. The risk factors associated with corneal inflammation include daily activities such as the wearing of contact lens, conditions of the eye such as eyelid misalignment, ocular surface diseases, ocular trauma, previous ocular surgery, corneal sutures, application of topical steroids, and even diseases that are not related to the eye such as diabetes mellitus [11]. Its severity can vary from a moderate, self-limiting condition, to a vision-threatening complication. Surgical intervention after corneal blindness has developed moderate success rate, where graft rejections and other post-operative complications pose a great challenge [12, 13]. Similar to any other diseases, early diagnosis and prevention is therefore the most cost effective and successful method in reducing the prevalence of blindness. A study conducted in a population of Central African Republic by Schwartz et al. in 1997 estimated that up to 90% of all blindness was in fact curable or avoidable [14, 15]. With the current state of the art medical technology, this number is believed to be much higher. Table 1.2 and 1.3 summarize the clinical observations, problem identification, and the *Need Statements* for glaucoma and corneal disease respectively.

Table 1.2 *Need Statement* addressing glaucoma.

Clinical observation	Despite the current state of the art medical technology, *in vivo* imaging of the anatomical structures of the anterior chamber of the eye still remains a challenge. Critical anatomical landmarks such as the scleral spur, Schwalbes' line, and TM are inaccessible to vision researchers and clinicians, and thus, they are not able to give objective information in the detection and evaluation of glaucoma.
Problem identification	With no all-round, foolproof concept and methodology for imaging angles, clinicians tend to use individualized approach for the assessment of glaucoma. Although it is true that any test is better than no test, this approach consequently means higher cost incurred by the patients.
Need Statement	There is a need for novel high resolution imaging methods for imaging the AOS and TM inside eye that have sophisticated data analysis strategies, are non-invasive, and have similar safety profile.

Table 1.3 *Need Statement* addressing corneal diseases.

Clinical observation	Corneal imaging systems in clinical ophthalmology are associated with limitations such as insufficient resolutions, operator requirement, risk of epithelial injuries, and speed of image acquisition.
Problem identification	There is no single instrument that is non-contact, has fast image acquisition speed, image the entire corneal layers and structures, and classify the disease state. Multiple testing means more stress on the patients.
Need Statement	There is a need for simple, non-contact, clinician and patient friendly optical imaging probe system for evaluation of corneal diseases.

1.2 Motivation

Despite the current state of the art medical technology, *in vivo* imaging of the anatomical structures of the anterior chamber of the eye still remains a challenge. Critical anatomical landmarks such as the scleral spur (SS), Schwalbes' line (SL) and TM are inaccessible to vision researchers and clinicians, and thus, they are not able to give objective information in the detection and evaluation of glaucoma. With no all-round, foolproof concept and methodology for imaging angles, clinicians tend to use individualized approach for the assessment of glaucoma. For example, some clinicians use the anterior segment optical coherence tomography (AS-OCT) as a first-pass method to detect eyes with narrow angles, as well as to obtain quantitative

information about the depth of the angle before proceeding to gonioscopy. OCTs are also used to observe pathological changes overtime and are the preferred patient education tools to help patients better understand their conditions in the clinical settings. Those with the technical capabilities choose to perform gonioscopy on all glaucoma suspects, since it is the gold standard for the assessment and evaluation of glaucoma. Ultrasound biomicroscopy (UBM) may also be employed, if the clinicians suspect something posterior to the iris. Although it is true that "any test is better than no test", this approach consequently means higher cost incurred by the patients. Undoubtedly, there is a need for novel high resolution imaging methods for imaging the AOS and TM inside eye that have sophisticated data analysis strategies, are non-invasive, and have similar safety profile.

In the context of corneal imaging, the *in vivo* laser scanning confocal microscopy (LSCM) [16, 17] is the most advanced imaging system that provides resolution of up to the cellular level. LSCM allows vision researchers and clinicians to image the entire corneal layers and structures, classify the disease state, and hence evaluate the treatment response without mechanically sectioning of the cornea. However, there is a risk of epithelial injury and the introduction of artefacts as a result of the applanation. The UBM [5, 18], despite being the standard reference for corneal pachymetry, and its ability to image the anterior segment through edematous or scarred corneal tissue, is impractical in many clinical situations because of the contact nature of the procedure, which makes it unsuitable for post-operative eyes and patients with prior ocular injuries. Moreover, image acquisition is time consuming and this further creates discomfort to the patient. The supine positioning of the patient during image acquisition may also cause distortion to the eye anatomy, especially the angle configuration [19]. All these indicate that

UBM is neither standardized nor in agreement with other non-contact methodologies. In addition, both of these contact procedures require a skilled and experienced operator in order to obtain high quality images and to minimize the risk of corneal abrasions and infections. AS-OCT [1-3, 20] is advantageous over the UBM because of its higher spatial resolution and speed of image acquisition, ability for standardization of scans, non-contact nature, and minimal requirements for expertise. Deep tissue imaging and imaging through corneal opacities are however not possible with light as an analysis medium. While the AS-OCT is unable to characterize and identify the infectious agent in the case of an inflammatory response, it is able to detect small changes in the microarchitecture of the cornea, and it is possible to monitor treatment response. Emerging technology based on multi-photon microscopy (MPM) is promising, offering a greater depth of penetration and lower phototoxicity compared to conventional confocal system. Nonetheless, there is still an extensive amount of translational and clinical investigation before its integration into clinical ophthalmology.

1.3 Objectives

Till date, gonioscopy remains as the gold standard for ICA evaluation. It is the fundamental part of eye examination and is needed to differentiate an open angle from a closed angle, and to note other pathological conditions. It is no wonder that vision researchers and clinicians are looking into novel imaging techniques that integrate gonioscopy or alternative imaging techniques that provide objective evaluation. The integration of non-diffracting Bessel beam with selective plane illumination microscopy (SPIM) has also open doors to a wide range of biomedical imaging applications [21-23]. From these perspectives, the main objectives of this thesis are directed towards the research and development of novel concepts and methodologies

for the high resolution diagnostic monitoring of open and close angle in glaucoma patients. This thesis also investigates into an optical method to examine and characterize the cornea. The main objectives of this research include:

(i) To design and optically engineer a flexible ocular imaging probe with specifications to capture the ICA images and posterior segment images. The imaging probe should have resolutions of ~50 µm at the ICA region and ~100 µm at the fundus.

(ii) Investigations into trans-corneal ICA imaging systems to resolve critical anatomical structures such as the TM, thereby enabling objective information about the AOS. The targeted spatial resolution is between 1 to 5 µm.

(iii) Investigation into simple and non-contact optical imaging probes for corneal imaging. The probes are expected to have spatial resolutions of lesser than 5 µm.

This proposed research includes the development of novel concepts and methodologies, theoretical modelling and simulations, instrumentations, and experimental validations.

1.4 Scope

This section details the different research tasks to be carried out for meeting the objectives. The research roadmap is illustrated using a flowchart shown in Fig. 1.1.

(i) ICA and fundus imaging with flexible ocular imaging probe.

   a. Design, theoretical analysis and modelling, and custom fabrication of a flexible ocular imaging probe.

   b. Characterization of the micro ScoutCam™ 3.0 and experimental investigations with eye model and *ex vivo* porcine eye samples.

   c. Preclinical imaging of small laboratory animals, *in vivo*.

d. Contact lens assisted imaging with *ex vivo* porcine eye samples.

e. Comparison with imaging systems in clinical ophthalmology.

(ii) Trans-corneal imaging of TM using Gaussian and Bessel-Gauss beam.

a. Conceptualization and development of a static Gaussian light sheet configuration and a digitally scanned Bessel-Gauss plane illumination configuration for ICA imaging.

b. Zemax simulations to compare digitally scanned Gaussian and Bessel-Gauss beams.

c. Conceptualization and development of an indirect axicon lens assisted gonioscopy imaging system.

d. Optical modelling and investigations into its imaging capabilities.

e. Theoretical and experimental validations with enucleated porcine eye samples.

f. Comparison with imaging systems in clinical ophthalmology.

(iii) Non-contact optical imaging probes for corneal imaging.

a. Conceptualization and development of non-contact optical imaging probes for corneal imaging.

b. Theoretical investigations into the optimization of infinity optics and scanning optics.

c. Experimental validations with *ex vivo* porcine eye samples and small laboratory animals, *in vivo*.

d. Clinical significance validation with *Pseudomonas* infected cornea.

(iv) Investigation into an optical configuration for the non-contact sequential imaging of the cornea and AOS.

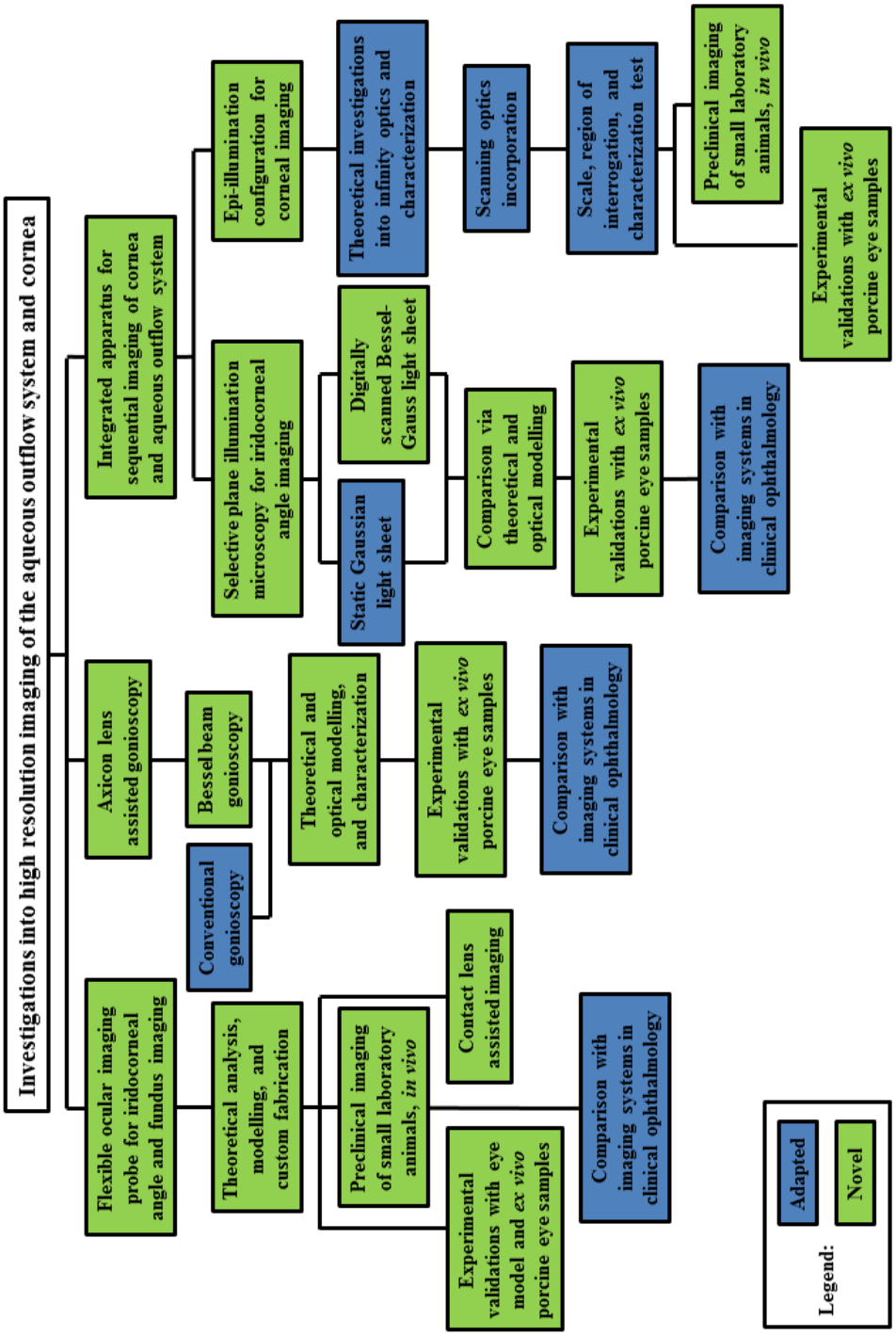

Fig. 1.1 Research roadmap.

1.5 Organization of thesis

This thesis is organized into six chapters. Each chapter begins with an outline of the chapter.

Chapter 1 is an introductory chapter which gives an overview of the *Need Statements* addressing glaucoma and corneal diseases. The *Need Statements* are based on clinical observations and problem identifications. This is followed by the objectives and scope of this thesis. The research roadmap is presented in the form of a block diagram. This chapter concludes with the organization of the thesis.

Chapter 2 begins with the disease state fundamentals of glaucoma, with particular focus on its anatomy, physiology, pathophysiology, clinical presentation, clinical outcomes, and epidemiology. The literature review that follows consists of three major sections. The first section discusses the progress in anterior chamber angle imaging for glaucoma risk prediction. It gives a review on clinical equipment, practice, and research. The next section reviews the optical imaging techniques for *in vivo* corneal imaging. These two sections are categorized into medical photographic and optical tomographic methods. The last section reviews SPIM in detail. This chapter ends with an outcome of the literature review which uncovers an important gap in the treatment landscape and validates the *Need Statements* that have already been defined.

Chapter 3 presents a methodology to design and theoretically analyze an imaging probe to evaluate the ICA structures using geometrical optics. Using Snell's law, an analytical analysis on light propagation from the anterior chamber of the eye to the exterior medium is first performed. This is followed by adopting a strategy to achieve uniform near field irradiance by simplifying the complex non-rotational symmetric irradiance distribution of light emitting diodes (LEDs) tilted at an angle. The optimization is based on the geometric design considerations of a circular

ring array of four LEDs tilted at an angle. The design equation gives insights on variable parameters such as the illumination angle of the LEDs, ring array radius, viewing angle of the LEDs, and the working distance. A micro color CCD video camera that has sufficient resolution to resolve the ICA and fundus structures at the required working distance is then chosen. Contact lens assisted imaging is also presented in this chapter, as an alternative method to overcome the phenomenon of total internal reflection at the tear-air interface. It serves as a better mechanical protective barrier against epithelial injury, as compared to the conventional ophthalmic gel or saline solution, which is commonly used in contact procedures such as gonioscopy and RetCam. The imaging capability of the developed probe and its variations are demonstrated using eye models, *ex vivo* porcine samples, and naturally occurring glaucoma models such as the New Zealand white rabbit and cynomolgus monkey, with high reproducibility and repeatability.

Chapter 4 presents two imaging systems for the high resolution *ex vivo* studies of the AOS inside porcine eye, based on a Gaussian illuminated and a digitally scanned Bessel-Gauss bean light sheet fluorescence configurations. The Bessel-Gauss beam is generated with the on axis illumination of an axicon lens. The digitally scanned Bessel-Gauss bean is able to overcome the trade-off between the length and thickness of the Gaussian light sheet to give better imaging performance. It has adequate spatial resolution to resolve critical anatomical structures such as the TM, thereby enabling objective information about the AOS. This non-contact and non-invasive imaging methodology with excellent safety profile is expected to be well received by vision researchers and clinicians in the evaluation and management of glaucoma. An indirect axicon lens assisted gonioscopy imaging system using white light illumination is also demonstrated. This imaging system integrates the concept of Bessel beam microscopy with

conventional gonioscopy imaging. The proposed concepts and methodologies are validated through theoretical modelling, simulations, and experiments with *ex vivo* porcine samples.

Chapter 5 demonstrates an optical method to examine and characterize the different layers of the cornea. Two initial lab prototypes are developed based on NIR epi-illumination configuration. The proposed concepts and methodologies are validated through spatial resolution characterization tests and experiments with *ex vivo* porcine samples. The probes possess high spatial resolutions and are non-dependent on coupling medium, which are significant for a clinician and patient friendly investigation. The clinical significance of the proposed study is validated by performing imaging of the New Zealand white rabbit's cornea infected with *Pseudomonas*.

Chapter 6 concludes this thesis. It highlights the major contributions, and provides the guidelines and recommendations for future research work.

Chapter 2: Literature review

This chapter begins with the disease state fundamentals of glaucoma, with particular focus on its anatomy, physiology, pathophysiology, clinical presentation, clinical outcomes, and epidemiology. The literature review that follows consists of three major sections. The first section discusses the progress in anterior chamber angle imaging for glaucoma risk prediction. It gives a review on clinical equipment, practice, and research. The next section reviews the optical imaging techniques for in vivo corneal imaging. These two sections are categorized into medical photographic and optical tomographic methods. The last section reviews selective plane illumination microscopy (SPIM) in detail. This chapter ends with an outcome of the literature review which uncovers an important gap in the treatment landscape and validates the Need Statements that have already been defined.

2.1 Glaucoma – A brief review

The eye [24, 25] is an asymmetrical fluid-filled sphere enclosed within three layers of tissues. The outermost layer consists of the white fibrous sclera and transparent cornea. The middle layer composes the iris and ciliary body at the anterior, and choroid at the posterior. The innermost layer is the retina. It is also the sensory part of eye that contains photoreceptors and other processing machinery for visual pathways.

The eye is divided into three distinct chambers filled with intra-ocular fluid. These chambers are bounded by various anatomical structures. The anterior chamber is the area of space between the posterior cornea and anterior side of the lens. The posterior chamber is the region between the iris and posterior of the lens. The vitreous chamber extends from the posterior of the lens to the retina. The anterior and posterior chambers are filled with aqueous humour, whereas the vitreous chamber is filled with vitreous humour. Aqueous humour is a nutritive fluid that is actively produced in the posterior chamber by ciliary processes. It gains entry into the anterior

chamber via the pupil. In contrast to aqueous humour which is clear and watery, the vitreous humour is viscous and gelatin-like. It makes up to about 80% of the volume of eye and functions to maintain the shape of eye. The vitreous humour also contains phagocytic cells with "housekeeping abilities" to ensure that there is minimal interference with light transmission. Fig. 2.1 shows the anatomy of human eye.

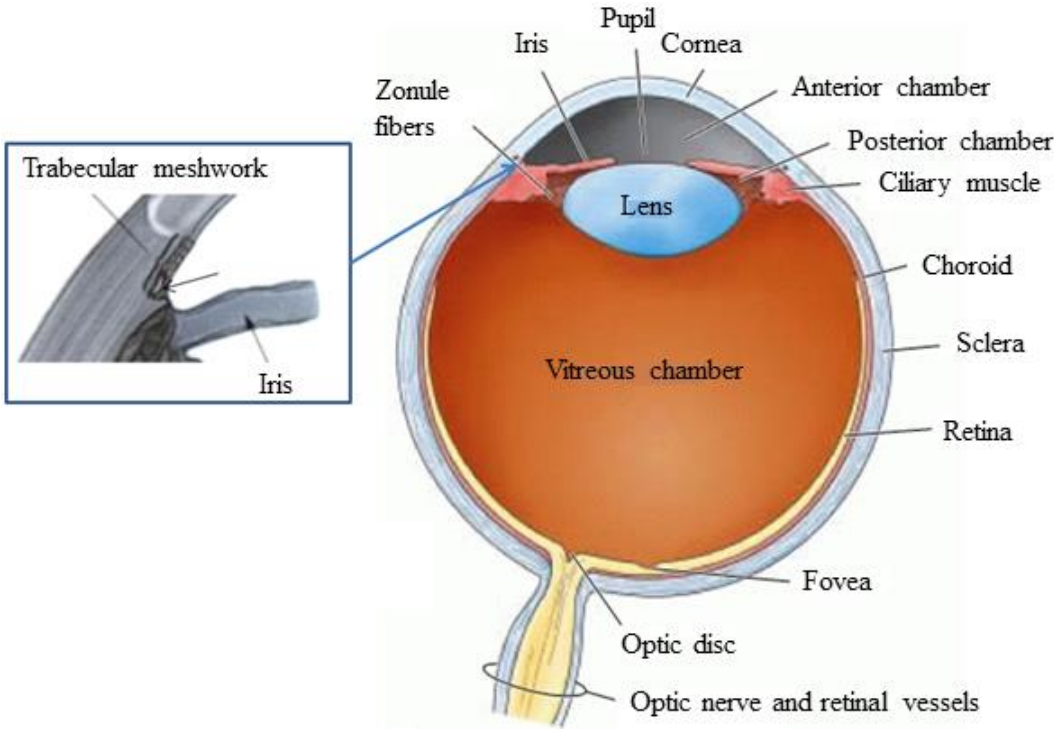

Fig. 2.1 Anatomy of human eye [25].

Aqueous humour exits the anterior chamber through the trabecular meshwork (TM), a specialized meshwork of cells at the junction of iris and cornea. It then passes through Schlemm's canal (SC) and collector channels (CC) before draining into aqueous veins and episcleral vessels [26]. Aqueous humour exits the anterior chamber of the eye at an approximate rate of 2.75 µl per minute. Abnormalities in the TM such as marked loss of TM cells, fusion and thickening of the trabecular lamellae, and increased deposition of sheath-derived plaques in

comparison to age-matched normal, can alter the aqueous humour flow rate. Under normal physiological condition, the rate of production and drainage of aqueous humour is at equilibrium, thus maintaining constant intra-ocular pressure (IOP). The width of the iridocorneal angle (ICA) is associated with the drainage of aqueous humor from the eye's anterior chamber. A wide angle permits adequate drainage of aqueous humour through the TM region, provided that the TM is not obstructed [27]. A narrow angle may obstruct the drainage system and lead to acute angle-closure glaucoma. Closed-angle or angle-closure glaucoma is related to the closure of ICA, corresponding to the area between the iris and cornea [28]. Primary angle-closure glaucoma and acute angle closure glaucoma are characterized by the anatomical predisposition of narrow angles with iridocorneal contact. In the latter, eye pressure may be in the range of 30 to 80 mm Hg and is an ophthalmic emergency [29-31]. The normal eye pressure is between 12 mm Hg and 22 mm Hg. The risk factors associated with glaucoma include an elevated IOP, age, chronic diseases, ethnic background, extreme near sightedness or shortsightedness, eye injuries, family history of glaucoma, and the long term use of corticosteroid [32-37]. Biometric characteristics of primary angle closure glaucoma include high central cornea thickness (CCT) value [38], shallow anterior chamber depth (ACD) [39], small corneal diameter and radius of curvature, anterior lens position, thick lens, and short axial length [40-42]. Fig. 2.2 illustrates the pathophysiology of various glaucoma related conditions.

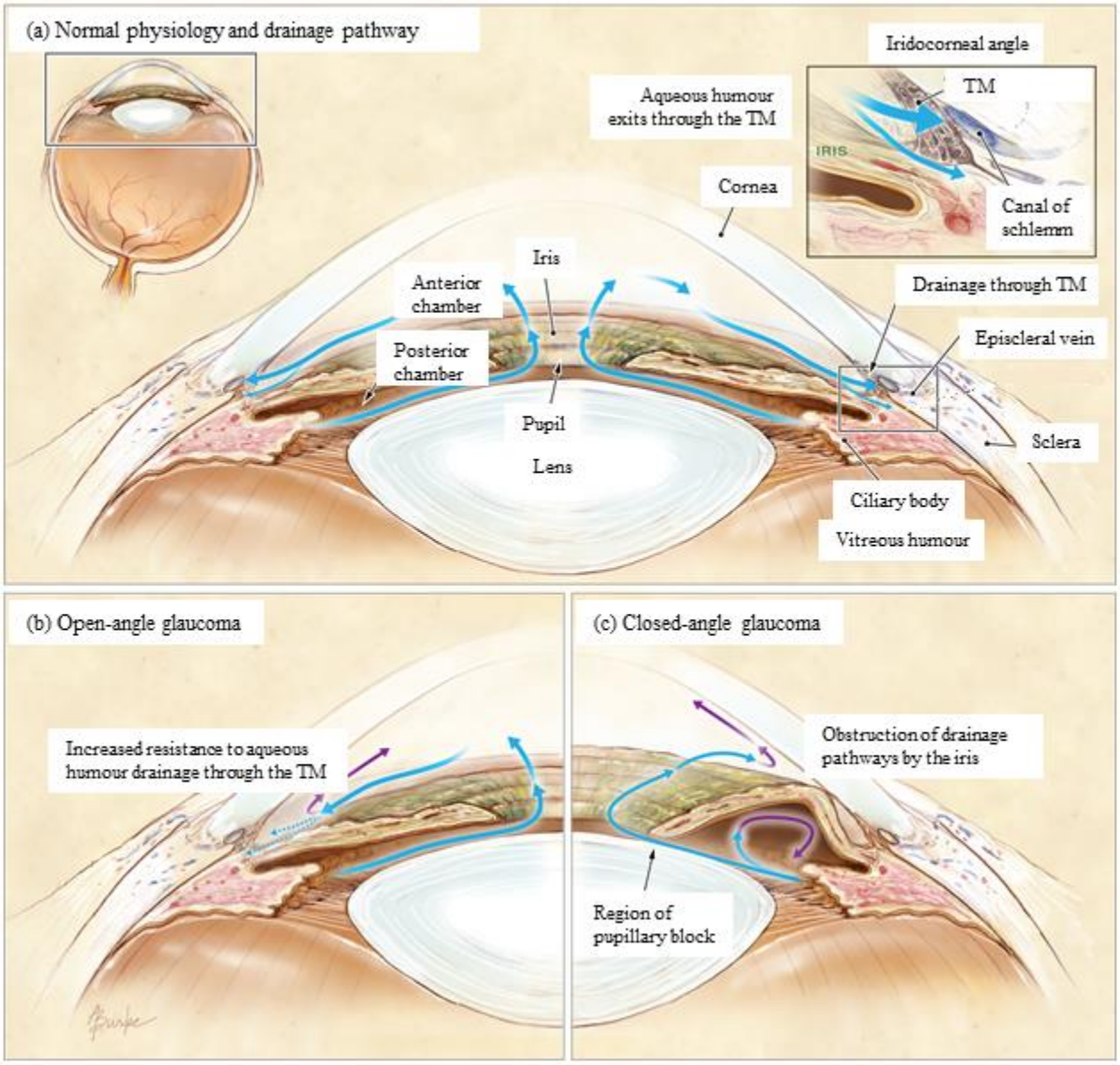

Fig. 2.2 (a) Normal physiology, (b) open-angle, and (c) angle-closure glaucoma [43].

The clinical presentation of glaucoma describes how the disease has an impact on the patient. It is usually represented by a range of signs and symptoms. The symptoms of glaucoma may vary among various clinical subtypes, or even between individuals with same condition. In primary open-angle glaucoma, the symptoms may not even be presented until permanent damage

has occurred. It is therefore advisable to go for regular eye examination even if one is not exposed to any risk factors. Table 2.1 shows some of the signs and symptoms of glaucoma.

Table 2.1 Signs and symptoms of glaucoma.

Symptoms	**Signs**
Blurred vision	High intra-ocular pressure (IOP)
Gradual loss of peripheral vision	Narrow iridocorneal angle
Halos around lights	Retinal nerve fiber layer damage
Nausea and vomiting	
Reddening of the eye	
Severe eye pain	
Sudden onset of visual disturbance, often in low light	

Clinical outcomes of glaucoma address the hard data points associated with the disease, and are usually measured in term of morbidity and mortality. Fortunately, glaucoma is not associated with an increased risk of death. It however, has certain lifestyle implications and severe complications which can ultimately lead to irreversible blindness if left untreated. Glaucoma is a chronic condition that requires life-long review even after successful control of IOP. Regular monitoring is required and this consequently has a direct impact on cost.

Based on a global study on visual impairment, glaucoma is one of the leading causes of blindness, second only to cataracts [9]. In 2010, the number of people affected by angle-closure and open-angle glaucoma was estimated to be 60.5 million. This number is expected to increase by about 30% to 79.6 million in 2020 [44]. The different clinical subtypes of glaucoma also show specific geographical distributions. While those of African derivation are more susceptible to open-angle glaucoma, primary angle-closure glaucoma is more prevalent in Asian countries, such as China, India, and Singapore [44-47]. Overall, the visual impairment due to glaucoma was

also found to be more common in women [9, 34, 44] due to the shallower anterior chamber and higher prevalence of angle-closure glaucoma.

Treatment for glaucoma includes pharmacologic or biologic therapy, energy based therapy, and surgery. Table 2.2 shows the range of treatments available for glaucoma. The choice of treatment is dependent on the clinical subtypes and its severity. For example, the management of narrow angles differs from open-angle glaucoma, with a possibility of prevention of progression using laser treatment in the former. The most common type of laser glaucoma management is laser iridotomy, where a small opening is made in the peripheral iris in an attempt to "open" the narrow angle, thus equalizing the pressure between the eye chambers. The need for surgical glaucoma management only arises if medications or laser fail to lower IOP to a safe level.

Table 2.2 Treatments available for glaucoma.

Glaucoma therapeutics	**Laser glaucoma management**	**Surgical glaucoma management**
Alpha agonists	Laser peripheral iridotomy	Glaucoma drainage devices
Beta-blockers	Laser iridoplasty	Goniosynechiolysis
Carbonic anhydrase inhibitors	Laser suturelysis post-trabeculectomy	Goniotomy
Cholinergic agonists	Selective laser trabeculoplasty	Trabeculectomy
Fixed combination drugs	Trans-scleral cyclophotocoagulation	Bled needling
Prostaglandin analogues		

Since glaucomatous damage is mostly irreversible, it is crucial to identify precisely eyes with early structural changes. The earlier glaucoma is identified and treated, the greater the possibility that medical or surgical management can be useful in preventing severe visual loss [8, 48]. The imaging of the region associated with the ICA has created immense interest among scientific community as if facilitate the diagnosis and monitoring of progressing eye conditions associated with glaucoma [30]. The sclera extending into the cornea near the ICA however obstructs any

direct view of the angle. Nonetheless, the assessment of anterior chamber angle is an essential part in the detection and diagnosis of angle closure glaucoma. Traditional imaging techniques to assess the drainage angle inside eye can generally be classified into medical photographic and optical tomographic methods. The following sections review the recent progress in anterior chamber angle imaging techniques for angle-closure glaucoma detection and follow-up procedures. The detailed description and classification of each technique are also given. Some definitions of anterior segment parameters can be found in Appendix A.

2.2 Anterior chamber angle imaging techniques

2.2.1 Medical photographic method

In photographic methods, the ICA region is captured using a camera and the images are stored in a database. It allows the monitoring of treatment responses overtime, and tracks anatomical changes in the angle structures as the disease progresses. Different types of medical photographic methods for evaluating angle closure condition are discussed in the following subsections.

2.2.1.1 Pentacam

Pentacam is based on Scheimpflug's photography principle [49, 50], where an obliquely tilted object is imaged with least distortion and maximum depth of focus under given conditions. Fig. 2.3 shows an illustration of the Scheimpflug principle. It shows the orientation of the plane of focus in an optical system where the lens plane is not parallel to the image plane. If the object plane is not parallel to the image plane, the lens focuses along the line where it intersects the plane of focus. Scheimpflug principle is employed in Pentacam and utilized in ophthalmology through a rotating measurement to obtain the optical sections of the entire anterior segment of

eye. It images the anterior segment from the cornea to the posterior surface of the lens in three dimensions. A Pentacam image of the anterior segment of a human eye is shown in Fig. 2.4.

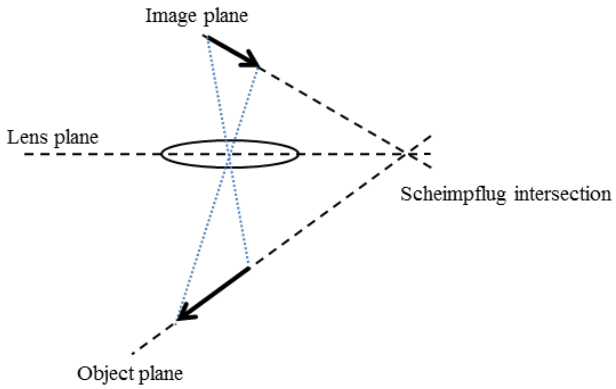

Fig. 2.3 Illustration of the Scheimpflug principle.

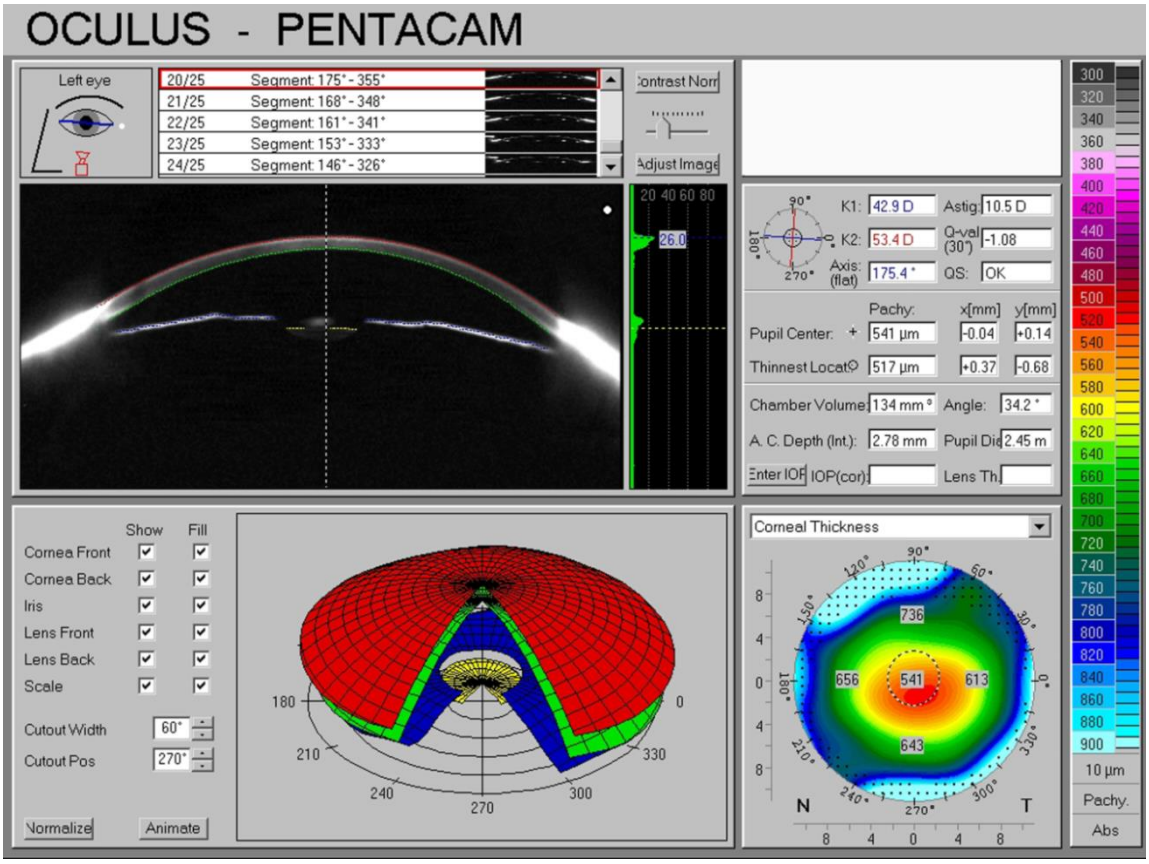

Fig. 2.4 Pentacam image and measurements of anterior segment in human eye.

This non-contact device offers rapid 3D analysis of the anterior chamber and can be used to measure corneal pachymetry, corneal diameter, radius of curvature, lens position, anterior chamber angle, depth and volume [51]. The imaging lasts less than 2 s and the center of cornea; its anterior and posterior surfaces can be measured accurately. It can be used as the primary assessment tool to evaluate angle-closure disease condition. However, the direct visualization of angle recess is not possible. This is because of the inability of the visible light to penetrate deep into the issues. In addition, the iris plane in Pentacam is defined using a straight line, rather than a curved plane. This results in inaccurate measurement of the angle width.

2.2.1.2 Gonioscopic photography

Gonioscopy is the fundamental part of eye examination. It is needed to differentiate an open angle from a closed angle, and to note other pathological conditions. Direct examination of the angle is not possible due to the total internal reflection of light emerging from the angle of the eye into the air. Gonioscopy utilizes a lens or prism with a different refractive index to overcome this problem. At any time, a quadrant of the anterior chamber angle can be visualized using conventional gonioscopy instruments. The angle structures are documented to make a decision regarding openness or closure of the angle. The structures seen include, from posterior to anterior – iris root (IR), ciliary body band (CBB), scleral spur (SS), TM (divided into pigmented posterior and non-pigmented anterior TM), and Schwalbes' line (SL). Commonly used definition for angle closure is the non-visibility of the posterior pigmented TM in at least two quadrants. Fig. 2.5(a) and Fig. 2.5 (b) correspond to open and close angle of a human eye using gonioscopic approach.

Gonioscopy is a subjective methodology whereby the ICA is documented by various grading procedures. The fundamental drawbacks of gonioscopy are physician compliance and patient

discomfort [52]. An earlier study has revealed that 50% of optometrists and ophthalmologists do not perform gonioscopy in clinical diagnosis [53]. This is because gonioscopy requires time-consuming expertise and methods, and is cumbersome. The interpretation of angle images is subjected to substantial disagreement among vision researchers and clinicians. Moreover, the use of coupling gel and multiple reflections from gonioscopic mirrors or lens reduce the quality of the angle images [54]. Nonetheless, gonioscopy is the clinical reference standard because it is able to make note of significant pathological findings by allowing the observation of angle structures using a cost-effective instrument. A cheaper alternative which can permanently document the angle findings through a photographic imaging technique with good quality images will be an important adjunct requirement in clinical ophthalmology.

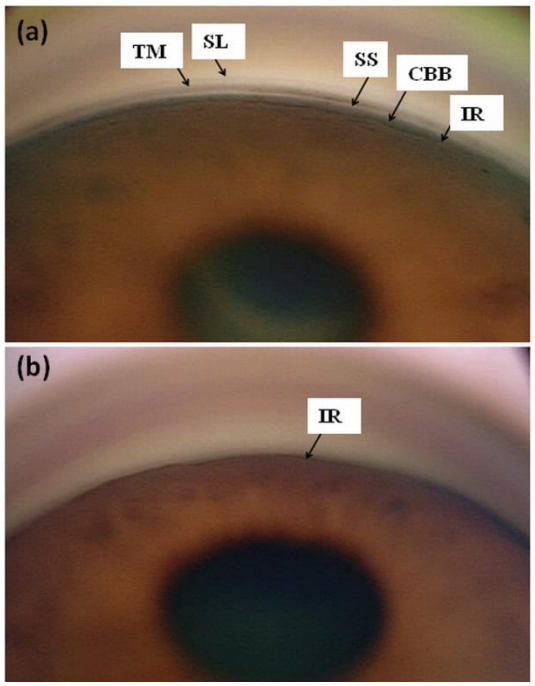

Fig. 2.5 Gonioscopic results showing (a) an open angle and (b) a closed angle.

2.2.1.3 RetCam

RetCam (Clarity Medical Systems Inc., Pleasanton, California, USA) is a fundus camera system originally designed to capture retina images for the diagnosis and monitoring of posterior segment diseases. It can be used to image structures of the anterior chamber with proper modifications [55]. For angle imaging, the patient is required to be in a supine position and a coupling gel (e.g. Vidisic gel) is applied between the patient's cornea and camera's lens. The gel functions as an optical interface to eliminate total internal reflection at the corneal tear film-air interface. This will allow the rays reflecting from the ICA region to be captured. The coupling gel is applied at the tip of the lens, and is placed at the opposite limbus to image the opposite angle. Fig. 2.6 shows images of an open angle obtained using the RetCam system from the nasal, inferior, superior and temporal sides of a human eye.

Clinicians can easily interpret the images produced by RetCam because the angle appears similar to those obtained from gonioscopy [56, 57]. RetCam has its advantages over standard gonioscopy. Since the patient is in a supine position, he cannot pull away from the distal end of the RetCam. This is one issue in the case of gonioscopy. Moreover, the distal end of the RetCam does not hold back the lower eyelid, and is smaller than the standard goniolens. Unlike gonioscopic photography, illumination from the RetCam is swept across the patient's pupils. This minimizes the discomfort as a result of the light intensity, and also minimizes angle related artifact. However, imaging of ICA using RetCam takes about 5 to 10 min per eye, much longer than gonioscopy [58].

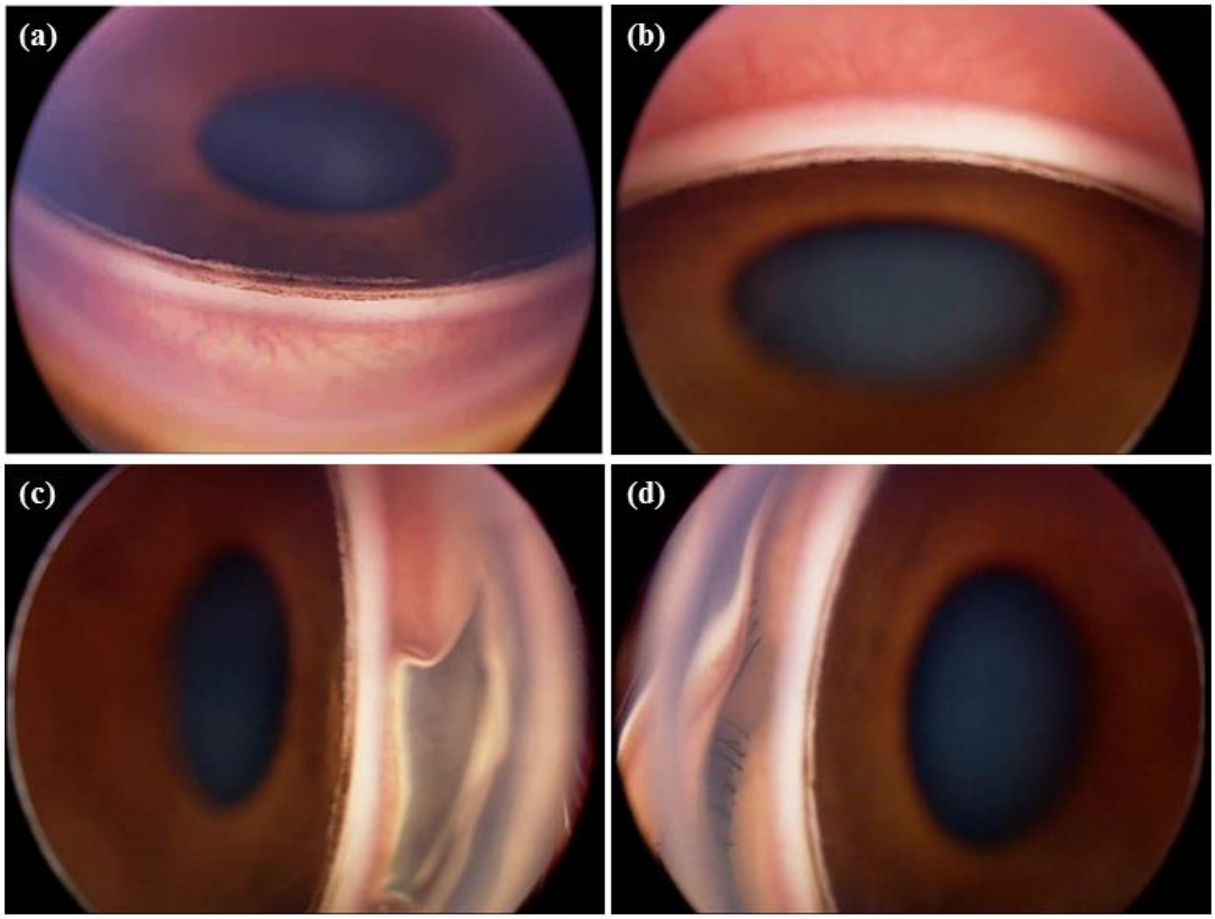

Fig. 2.6 RetCam images of (a) inferior, (b) superior, (c) nasal, and (d) temporal quadrant.

2.2.1.4 Gel-assisted imaging probe

Recently, a gel based probe prototype for imaging the ICA region of eye was designed and demonstrated [59]. The light transmission from the anterior chamber to the exterior of eye is analytically considered. A fiber-optic broadband light source is collimated and redirected to illuminate the iridocorneal region. The light reflected from the ICA region is collected through a long working distance objective lens and directed to a charge-coupled device (CCD) camera. A mirror is used to redirect the beam to the objective lens. The region between the mirror and eye model is filled with coupling gel (e.g. Vidisic gel). The mirror can be rotated to have a clear view of the ICA region. A schematic of the experimental setup and the result obtained after

highlighting the angle region of an eye model are shown in Fig. 2.7. The width of the ICA region in Fig. 2.7(b) is indicated using arrows between the margin of cornea and base of iris.

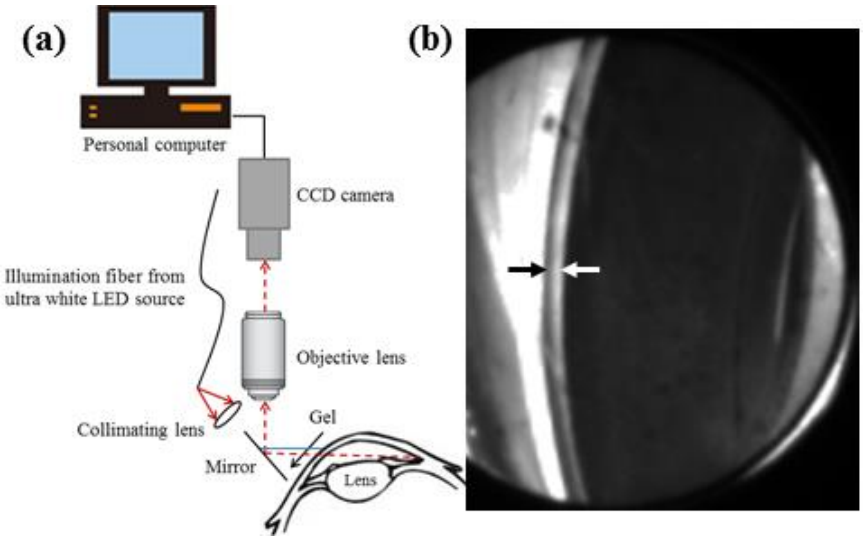

Fig. 2.7 (a) Schematic of gel-assisted imaging probe and (b) ICA image of model eye.

2.2.2 Optical tomographic imaging methods

Optical tomographic imaging techniques are non-invasive imaging techniques that allow visualization of the internal structures of an eye without the superposition of over- and under-lying structures. Different optical tomographic imaging techniques based on ultrasound biomicroscopy (UBM), optical coherence tomography (OCT), and photoacoustic (PA) are studied for imaging the anterior chamber of eye as given in the following subsections.

2.2.2.1 Ultrasound biomicroscopy (UBM)

In this method, the depth of the ocular tissue structures is determined by measuring the time delay of returning ultrasound signal which the computer assembles to provide a magnified high resolution image. Ultrasound biomicroscopy (UBM) requires the transducer to be in contact with the eye and the scanning is performed through an immersion bath. UBM provides two dimensional (2D) gray scale images of the various anterior segment structures, and can be used

to measure the depth of the anterior and posterior chambers, as well as the anterior chamber angle. UBM has been extensively used in various clinical and experimental applications on glaucoma for diagnostic purposes. Image acquisition time depends upon the cooperation of the patient and the experience of the examiner. Axial resolution of up to 20 μm is possible at operating frequency of 50 MHz [51]. Fig. 2.8 shows the UBM image of the anterior chamber, chamber angle and angle parameters. ACD, angle opening distance (AOD) and trabecular-iris space area (TISA) can be measured using UBM.

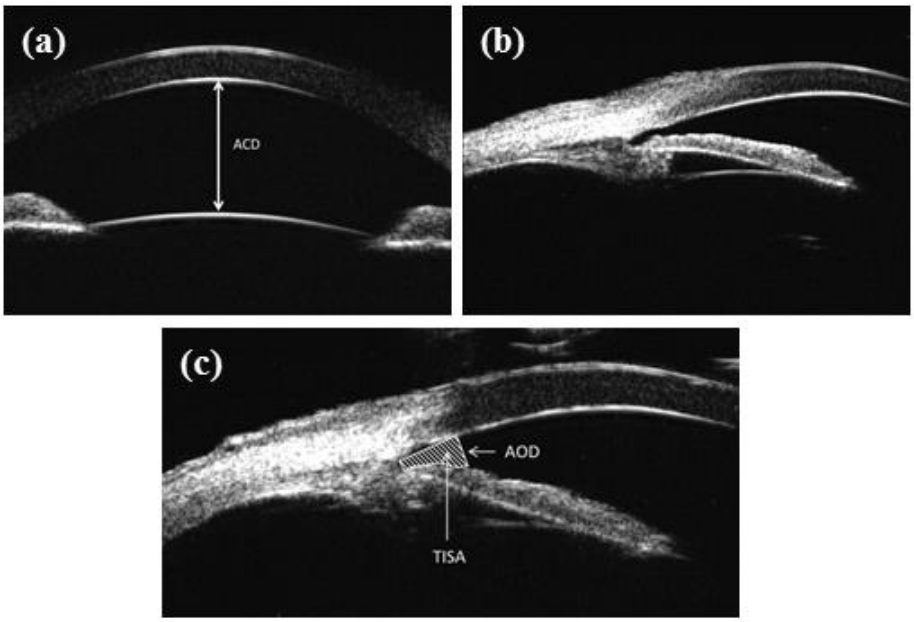

Fig. 2.8 UBM images of (a) anterior chamber, (b) open-angle, and (c) angle parameters.

Narrow angle can be easily noted and confirmed with UBM. The angle can be assessed either in dark or bright light condition. Under dark condition, the pupil dilates and the angle tends to narrow. The posterior chamber, anterior lens surface, ciliary body, iris, angle, anterior chamber, and cornea can be easily visualized [5]. Since this technique helps in the evaluation of the underlying mechanisms of angle-closure, it is useful in deciding the appropriate form of treatment. It is also useful in the evaluation of open-angle glaucoma such as pigment dispersion

syndrome. The structures surrounding the posterior chamber can be imaged and evaluated using UBM. However, contact of the transducer with eye is necessary, and this creates discomfort to the patient with risks of corneal abrasions and infections. A skilled and experienced operator is needed and the procedure is time-consuming. Requirement for the patient to be in a supine position may cause an artifactual widening of the anterior chamber angle [19]. Another disadvantage is the lack of standardization between UBM scans.

2.2.2.2 Optical coherence tomography (OCT)

Optical coherence tomography (OCT) is analogous to UBM, but light is used instead of sound. The working mechanism of the OCT is based on low-coherence tomography and it uses the principle of a Michelson Interferometer to detect optical backscatter. The ability of the OCT to provide good repeatability and reproducibility for quantitative and qualitative analyses of the angle recess makes it a valuable diagnostic instrument for disease documentation of angle closure glaucoma, disease progression, and therapeutic outcomes. Higher spatial resolution, high speed image acquisition, ability for standardization of scans, non-contact nature and the minimal requirements for expertise make OCT method advantageous over UBM.

2.2.2.2.1 Visante OCT

The Visante OCT (Carl Zeiss Meditec, Dublin, California, USA) is a time-domain, anterior segment OCT system that uses a longer wavelength of 1310 nm. It allows deeper penetration and cross-sectional imaging of the anterior chamber, as well as visualization of the ICA [60]. Low-coherence light beam in the near infrared (NIR) region is split, and simultaneously directed onto the tissue and the reference mirror. The relative location of the backscattered light from the image tissue can be obtained based on the information from the internal reference mirror.

Following data acquisition, the scanned images are processed by a geometric computational process that converts the optical distance to physical distance, prior to scan review and analysis. The geometric computational process takes into consideration the refraction index variations at the corneal air/ tissue interface and the tissue/ aqueous interface. Light at this wavelength has lower scattering loss and can penetrate deeper through the ocular structures. In addition, this wavelength is strongly absorbed by the vitreous humour, and only an approximated 10% of the incident light reaches the retina. The increase in retinal protection enables high power illumination which in turn results in high speed imaging. These two properties of the NIR light allow clinicians to obtain a more detailed morphology of the anterior segment and minimize image distortion and motion artifacts. Interference is measured by a photodetector when the backscattered light from both sources combined.

The Visante OCT is able to make 2000 A-scans per second, with a scan acquisition time of 0.125 s per line (8 frames per second) for the Anterior Segment Scans, and 0.25 s per line (4 frames per second) for High Resolution Cornea Scans. The 6 mm deep scan range and 16 mm wide field scanning allow the entire anterior chamber to be imaged in a single frame. As in the case of conventional microscopy, the transverse resolution of 60 μm is determined by the focusing parameter, the diffraction properties of light, and the spot size of the focusing beam. Good axial resolution of 18 μm is possible due to the small numerical aperture focusing and a large depth of focus using low-coherence tomography. The quality of the images is also influenced by pixel intensity (analogous to pixel density in digital photography) and the speed of acquisition. Details on the basic principles of the Visante OCT have already been covered extensively in previous literatures [20, 61, 62]. The area of the choroid and sulcus cannot be

imaged since the infrared light is unable to pass through the posterior layer of the iris. Area of the ciliary body is not entirely visible unlike that seen in UBM, due to the absorption of infrared light through the sclera [30, 63]. The location of the TM is also undetermined. Angle closure with the Visante OCT is determined by any contact between the iris and the angle wall anterior to the SS whereas for gonioscopy, the quadrant would still be considered open unless the apposition reached the posterior of the TM. The Visante OCT therefore overestimates the frequency of angle closure in the superior and inferior quadrants with respect to gonioscopy [6], the gold standard for angle evaluation.

In addition, there are no built-in analytical tools to analyze pachymetry maps or to detect an angle measurement and indicate "narrow angles" to the user. The SS, which is the anatomical landmark for angle imaging, has to be determined manually and is not detectable in up to 28% of the patients in a particular study [58]. Since the time-domain Visante OCT involves the sliding of a mirror along the reference arm, it is relatively time consuming as compared to the Fourier-domain OCT (FD-OCT). Fig. 2.9 shows a quantitative assessment of a patient's cornea after partial thickness corneal transplant. Measurements were taken at different points (approximately $\pm$ 2.6 mm) from the center of the cornea. The image was taken using the High Resolution Corneal Scan mode of the Visante OCT. Fig. 2.10 shows the measurement of angle parameters of a patient using the iridocorneal tools set and chamber tool of the Visante OCT.

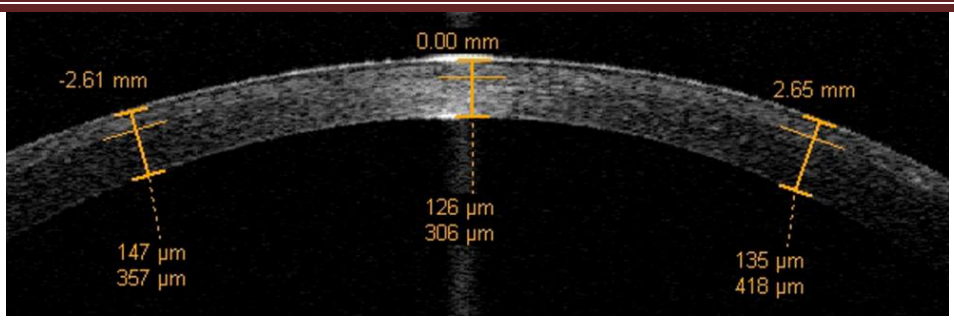

Fig. 2.9 High Resolution Corneal Scan of a patient.

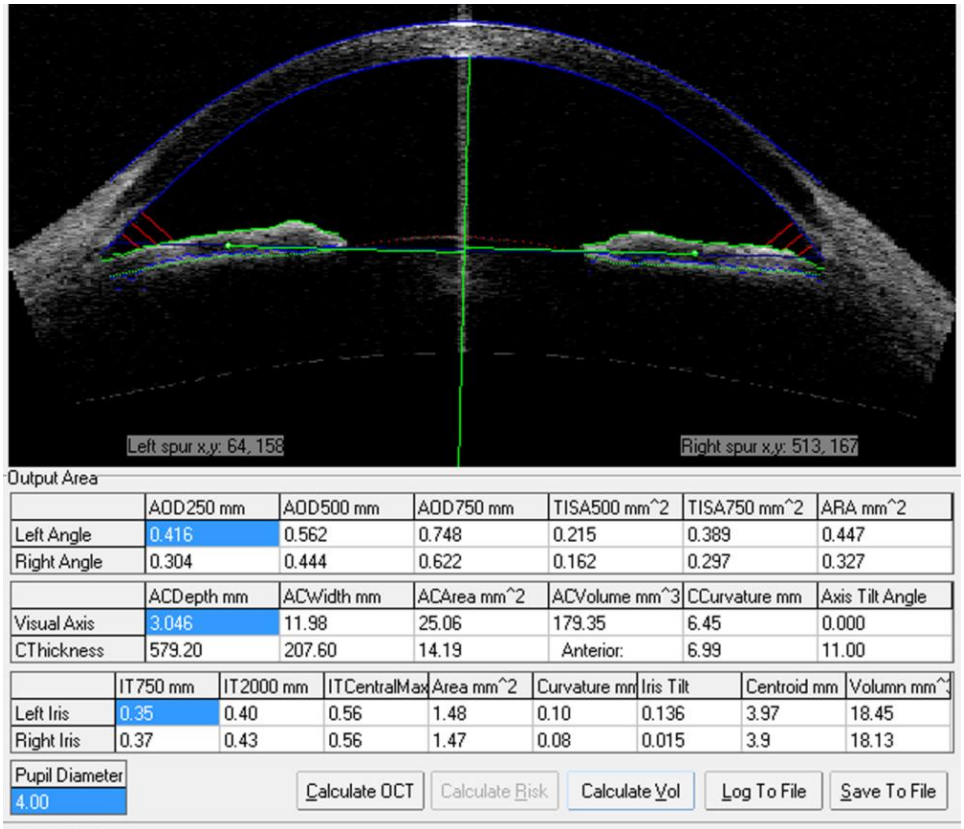

Fig. 2.10 Measurement of angle parameters using Visante OCT.

2.2.2.2.2 Slit lamp OCT (SL-OCT)

The slit lamp OCT (SL-OCT) (Heidelberg Engineering, Dossenheim, Germany), as its name suggests, is a combination of the slit lamp technology with the OCT. It is another diagnostic device that is used for the non-invasive imaging and measurement of the anterior segment of the eye [64, 65]. It is a time-domain instrument that operates on a low-coherence super-luminescent

light source at 1310 nm wavelength. The SL-OCT has A-scan frequency of 200 Hz, an axial resolution of lesser than 25 μm, and a transverse resolution of 20-100 μm. The system's built-in software is able to automatically identify the SS. This physical landmark is subsequently confirmed by the user, in order to calculate the anterior chamber angle (ACA), the AOD, angle-recess area (ARA), trabecular-iris contact length (TICL) and TISA. The Digital Gonioscopy tab measures the ACA, AOD, and the TISA whereas the Auto-Biometry tab measures the CCT, anterior and posterior corneal radii, ACD, estimated anterior chamber volume (ACV), pupil diameter, and the spur-to-spur distance. The ACV is another important parameter that is used to identify individuals that are susceptible to developing primary angle closure [66, 67]. A study by CK Leung et al. concluded that even though the Visante OCT and the SL-OCT have excellent inter-observer reproducibility, their agreement was poor [1], suggesting that the results cannot be used interchangeably. There are several factors resulting in this difference and they include the scan location, state of accommodation, the algorithms for imaging dewarping, and the choice of refractive indexes. The details have been explained by Leung et al..

2.2.2.2.3 Cirrus or spectral-domain OCT (SD-OCT)

The Cirrus OCT (Carl Zeiss Meditec, Dublin, California, USA) is another commercially available optical instrument that is non-invasive. Unlike the time-domain Visante and SL-OCT systems, the Cirrus OCT is a spectral-domain instrument (also known as SD-OCT) that uses NIR light of 840 nm wavelength. This system is designed primarily for retinal imaging but also supports several modes, including iris, cornea, and angle evaluation by using an anterior segment lens adapter. The images of the angle region as well as the cornea of human eye using Cirrus HD-OCT is shown in Fig. 2.11. Since the SD-OCT obtains the detected interferometric signal as

a function of optical frequencies, its imaging speed is 50-60 times faster than the Visante OCT [68]. It has an axial resolution of 5 µm, and a transverse resolution of 15 µm. The Cirrus OCT enables user to identify the SL (solid line), SS (asterisk), and TM (broken line). The improved resolution of SD-OCT also allows user to identify the interface between the epithelial/ Bowman's layer and corneal stroma.

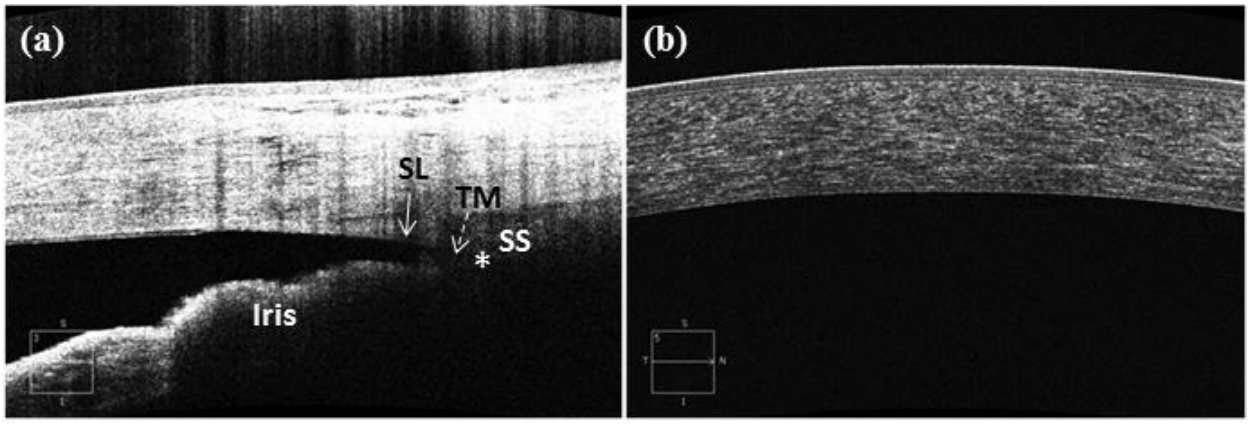

Fig. 2.11 Cirrus OCT images of the (a) anterior chamber and (b) cornea.

The higher resolution of SD-OCT means improved visualization of the cornea and angle, as well as the ability to image ocular substructures such as the TM, the SS, and the SL [69-71]. Comparing with Fig. 2.9, the High Resolution Cornea Scan with the Visante OCT does not allow differentiation of the cornea layers. Contrary to the Visante OCT, the Cirrus OCT tends to underestimate the frequency of angle closure compared to gonioscopy. This discrepancy arises because the SD-OCT does not allow a wide field view of the anterior segment, thus making it difficult to assess the angle recess.

2.2.2.2.4 Casia SS-1000 OCT

The CASIA SS-1000 OCT (Tomey Corporation, Nagoya, Japan) is a novel, non-invasive imaging instrument that is used for the diagnosis of the anterior chamber of the eye [3]. It is

based on Fourier-domain, and is operated with a swept laser source at 1310 nm wavelength. This swept-source OCT (SS-OCT) has A-scan frequency of 30,000 Hz, an axial resolution of 10 µm, and a transverse resolution of 30 µm. It has a wide scanning range and depth of 16 mm and 6 mm respectively, similar to that of the Visante OCT. These values mean that the system is able capture the entire cross-section of the anterior segment simultaneously. In addition, the entire circumference of the ACA can be analyzed by performing multiple radial scans, using the low density 3D angle analysis scan which can render 3D renderings as shown in Fig. 2.12.

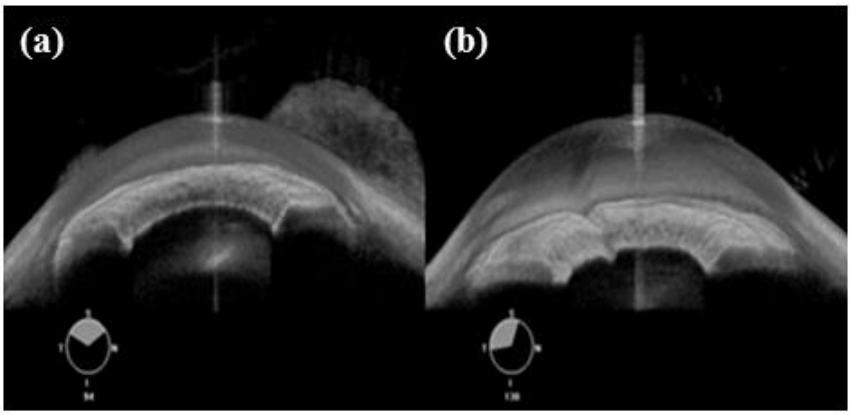

Fig. 2.12 CASIA SS-OCT images of (a) a closed angle and (b) an open angle.

With this unique feature, the system's in-built software is able to perform a 360° analysis of the iris-trabecular contact (ITC). The ITC index is a new parameter that was introduced to semi-quantitatively analyze angle closure using the CASIA SS-1000 OCT [72]. Good inter- and intra-observer reproducibility of the ITC index and conventional angle parameters have been reported by Ho et al. [72] and Liu et al. [73]. Lastly, the SS-OCT also reported a higher rate of angle closure compared to gonioscopy [3]. Table 2.3 shows a comparison of the properties and differences between the Visante OCT, Slit Lamp OCT, Cirrus OCT, and CASIA SS-1000 OCT.

Table 2.3 Comparison of Visante , Slit Lamp, Cirrus, and CASIA SS-1000 OCT.

OCT type	Optical Source	Axial resolution (μm)	Transverse resolution (μm)	Scan speed (A-scans per second)	Scan depth (mm)	Scan width (mm)
Visante OCT[1]	SLD 1310 nm	18	60	2,000	6	16
Slit Lamp OCT[1]	SLD 1310 nm	< 25	20-100	200	7	15
Cirrus OCT[2]	SLD 840 nm	5	15	27,000	2	6
CASIA SS-1000 OCT[3]	Swept source laser at 1310 nm	10	30	30,000	6	16

2.2.2.3 Photoacoustic imaging

Photoacoustic (PA) imaging is a potential imaging modality that is particularly advantageous for imaging optically deep structures with good spatial resolution [74, 75]. Here, a diffused, short monochromatic light pulse is illuminated at the sample and absorbed by pigments at emitted wavelength. The absorbed energy is converted to heat that in turn leads to thermoelastic expansion of the sample. The rise in pressure forms sound waves which can be detected. The magnitude of the PA signal is directly related to the optical absorption coefficient of the illuminated sample at a given wavelength. This differ PA imaging from other imaging modality such as UBM or OCT. Since optical scattering is much stronger than acoustic scattering and optical absorption occurs with either scattered or ballistic photons, PA imaging can image much deeper structures than OCT. PA imaging has a scalable spatial resolution from several microns to millimeter, which makes it a promising tool for broad applications in biomedicine.

The major light-absorbing biomolecules present in the eye are hemoglobin and melanin. The optic nerve and posterior pole of eye have high volume of hemoglobin with peak absorption of about 580 nm [76]. Melanin has maximum absorption in the ultraviolet and near-ultraviolet region and is almost completely attenuated for wavelengths longer than 700 nm [77]. It is found in the uvea, comprising of the ciliary body, choroid, and iris. Ultrasound and PA imaging can be

carried out concurrently since the ultrasound transducer is able to function in receive mode for PA or pulse and echo for ultrasound mode. Hence complementary information such as optical absorption and acoustic impedance discontinuity can be obtained from the tissue at the same time. Ultrasound and PA imaging of the anterior segment of eye using a 20 MHz transducer and a 532 nm pulsed laser is carried out [78]. The anterior surface of the iris, cornea and crystalline lens are much sharper in PA image due to the stronger absorption of melanin at this wavelength. PA imaging is performed for imaging blood distribution in the eye and was able to collect signals from the deep layers in the eye including the choroid, sclera, and optic nerve [79]. PA imaging of porcine eye sample is carried out and the result obtained is shown in Fig. 2.13. Both anterior and posterior structures are visible here. No investigation has been made to image the TM region using PA technique and exogenous contrast agents till date.

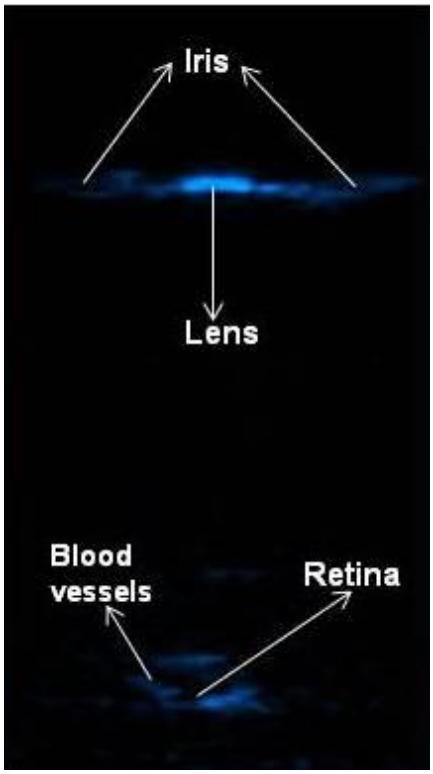

Fig. 2.13 PA imaging of enucleated porcine eye.

2.3 *In vivo* corneal imaging techniques

2.3.1 Medical photographic methods

2.3.1.1 Orbscan IIz

Orbscan IIz (Bausch & Lomb Surgical Inc., San Dimos, California, USA) is a non-contact anterior segment imaging tool that integrates slit scanning technology with Placido disc [80, 81]. The slit scanning system assesses surface elevation of the anterior and posterior cornea, anterior lens surface, and iris, whereas the Placido disc measures the anterior corneal curvature directly by analyzing specularly reflected images of the rings on cornea. The high resolution digital video camera captures 40 light slits (20 on the left, and 20 on the right) projected onto cornea at a fixed angle of 45° along the instrument axis. The dimensions of the slits are measured, and the data points are combined and analyzed to reconstruct the topographic information, corneal thickness, and other anterior chamber parameters [80-82]. Image acquisition with Orbscan IIz does not require much technical expertise and wavefront analysis is also possible with a Zyoptix workstation. The Orbscan IIz however, has limited uses in cases of corneal opacities or abnormalities because it tends to show a thinner cornea and topographic data of the posterior cornea can even suggest a post-operative ectasia. Moreover, it is unable to detect interfaces accurately, and image acquisition and processing require a longer time frame in comparison to conventional Placido-based techniques.

2.3.1.2 Pentacam

The working principle of Pentacam has been explained in Section 2.2.1.1. The Pentacam has two cameras. The rotating Scheimpflug camera is used to perform corneal scans and it can image the cornea from different angles [83]. The second camera is static and it measures and detects the

pupil. This camera functions as orientation and fixation. Elevation data obtained from the photographs are used to reconstruct the corneal topographies and calculate other parameters. Operation of the Pentacam does not require much expertise since image acquisition is automated. Though the Pentacam demonstrates high repeatability in the measurement of corneal parameters in pre- and post-operative eyes, there are discrepancies with results obtained from ultrasonic pachymetry or Orbscan IIz, especially in keratoconus and refractive surgery. The absence of a reference device for topography measurements often leads to conflicting information in a clinical setting.

2.3.2 Optical tomographic imaging methods

2.3.2.1 Ultrasound biomicroscopy (UBM)

The working principle of UBM has been explained in Section 2.2.2.1. The penetration depth and resolution of UBM is dependent on the operating frequency of the transducer. While a higher frequency enhances the tissue resolution, the penetration depth is reduced, vice versa. For corneal imaging, axial and transverse resolution of 25 μm and 50 μm is possible at operating frequency of 50 MHz. At this resolution, it is possible to image the fine structures of LASIK flaps, characterize the corneal layers, and define the 3D structure of cornea.

2.3.2.2 Anterior segment optical coherence tomography (AS-OCT)

The working principle of AS-OCT has been explained in Section 2.2.2.2. AS-OCT is highly sensitive, and can detect reflected signals that are several orders smaller than the incident optical power. Light sources are usually in the NIR region, for better tissue penetration in scattering media. Deep tissue imaging and imaging through corneal opacities are not possible with light as an analysis medium. While the AS-OCT is unable to characterize and identify the infectious

agent in the case of an inflammatory response, it is able to detect small changes in the microarchitecture of the cornea, and it is possible to monitor treatment response.

2.3.2.3 *In vivo* laser scanning confocal microscopy (LSCM)

The *in vivo* laser scanning confocal microscopy (LSCM) is the most advanced confocal system that provides resolution of up to the cellular level, allowing vision researchers and clinicians to image the entire corneal layers and structures, classify the disease state, and hence evaluate the treatment response without mechanically sectioning of the cornea. However, there is a risk of epithelial injury and the introduction of artifacts as a result of the applanation. The Heidelberg Retina Tomograph III, Rostock Cornea Module (HRTIII-RCM) (Heidelberg Engineering Gmbh, Dossenheim, Germany) operates with a diode laser at 670 nm wavelength for illumination. It uses a Zeiss water immersion objective to enhance performance in terms of resolution and aberration correction [84]. During image acquisition, the objective is covered by a polymethylmetacrylate Tomo-Cap (Heidelberg Engineering GmbH, Dossenheim, Germany) and an ophthalmic gel (Vidisic Gel, Bausch & Lomb GmbH, Berlin, Germany) is used as a coupling agent between the applanating lens cap and cornea. A small digital camera is employed to assess and document the alignment of eye with laser beam. The controller is adjusted such that the center of Tomo-Cap is applanated onto center of cornea. The digital micrometer gauge is set at zero, at the point where the digital image of the first superficial cells is seen. Sequence images are recorded by gradually moving the focal plane forward into the corneal stroma.

In confocal microscopy, the pinhole at the conjugate of focal plane acts as a stop to eliminate out-of-focus blurs, by preventing light emanating from regions above and below the focal plane from contributing to the images. Illumination is therefore restricted to the focal plane and

generation of 3D images is possible via optical sectioning [85, 86]. Elimination of stray light from imaging system not only improves contrast, but also increases signal-to-noise ratio [87]. Specular reflected images of cornea are obtained based on reflected light imaging modality. Two in-built scanning mirrors are used to perform a raster scan over the region of interrogation. The 2D images consist of 384 X 384 picture elements, and cover an area of 400 µm X 400 µm. This means that multiple sections and hence, a longer image acquisition process is necessary in order to evaluate larger region of interest (ROI). Lateral and axial resolutions were quoted at 1 µm/ pixel and 2 µm/ pixel respectively by the manufacturer. The amount of light reflected changes with respect to the difference in refractive indices of various structures in cornea. A large difference in the refractive indices between structures corresponds to a larger reflectance and hence, a higher contrast. One advantage of reflected light LSCM over fluorescent confocal microscopy is that no fluorescent dyes are required for imaging. Consequently, problems associated with photobleaching and photosaturation need not be considered. In addition, the intensity of signal in reflected mode is much higher than intensity obtained from fluorescence modality. Table 2.4 shows the technical specifications of various tomography systems used in clinical ophthalmology for the evaluation and management of corneal diseases.

Table 2.4 Technical specifications of tomography systems in clinical ophthalmology.

Instrument	Scan source	Measuring principle	Axial resolution (µm)	Transverse resolution (µm)	Coupling medium	Patient position	Operator requirement
Orbscan II [7]	White flash light	Slit-scanning	N.A.	N.A.	No	Upright	Simple, non-contact
Pentacam [7]	Blue LED 470 nm	Scheimpflug imaging	N.A.	N.A.	No	Upright	Simple, non-contact
Paradigm P60 UBM [5]	Ultrasound (50 MHz)	Ultrasound	25 µm	50 µm	Yes	Supine	Skilled, contact
Visante™ OCT [1]	SLD 1310 nm	Interferometry	18 µm	60 µm	No	Upright	Simple, non-contact
Slit Lamp OCT [1]	SLD 1310 nm	Interferometry	< 25 µm	20-100 µm	No	Upright	Simple, non-contact
Cirrus OCT [2]	SLD 840 nm	Interferometry	5 µm	15 µm	No	Upright	Simple, non-contact
CASIA SS-1000 OCT [3]	Swept source laser at 1310 nm	Interferometry	10 µm	30 µm	No	Upright	Simple, non-contact
Heidelberg Retina Tomograph III Rostock Cornea Module [4]	Laser diode at 670 nm	Confocal	2 µm	1 µm	Yes	Upright	Skilled, contact

2.4 Light sheet fluorescence microscopy (LSFM)

There are many implementations of light sheet fluorescence microscopy (LSFM) since its conceptualization in the 1900s. Some of these examples, developed in chronological order, are ultramicroscopy [88], orthogonal-plane fluorescence optical sectioning microscopy (OPFOS) [89], thin laser light sheet microscopy (TLSM) [90], selective plane illumination microscopy (SPIM) [91], objective-coupled planar illumination (OCPI) [92], oblique plane microscopy (OPM) [93], and digital scanned laser light sheet microscope (DSLM) [94]. Qualitative features that are common to the LSFM family include low photobleaching rate and energy load, and high imaging speed and signal-to-noise ratio. These characteristics are due to the confined plane of excitation which maximized the illumination efficiency, and the use of high photon efficiency detectors, respectively. There are also quantitative differences in functionality between these implementations. For example, while OPFOR, SPIM and DSLM are intended for biological

applications, TLSM is not developed for tissue sectioning microscopy. SPIM and DSLM are the preferred choice for *in vivo* imaging of biological specimens since the Spalteholz clearing method [95] in OPFOR is not suitable for living samples.

Amongst the non-destructive tomographic instruments, LSFM have faster image speed and higher resolution as compared to instruments such as magnetic resonance imaging (MRI) and computerized tomography (CT). When comparing with two-photon microscopy and confocal microscopy, LSFM can image thicker samples with least phototoxicity and photobleaching. In addition, the cost of construction is significantly lower as compared to these microscopes. Table 2.5 shows a comparison of several non-destructive tomographic instruments.

Table 2.5 Comparison of non-destructive tomographic instruments.

Instrument	**Excitation signal**	**Resolution**	**Imaging time**	**Specimen size**	**Contrast agent**	**Photobleaching**
Computerized tomography [96]	Radioactive	< mm	min	Large	Non-fluorescent	Not applicable
Magnetic resonance imaging [97]	Magnetic	mm	hr	Large	Non-fluorescent	Not applicable
Confocal microscopy [87]	Laser	< µm	ms	µm	Fluorescent	Yes
Two-photon microscopy [98]	Laser	< µm	ms	mm	Fluorescent	Yes, but lesser than confocal
Light sheet fluorescence microscopy [89]	Laser	µm	ms	> cm	Fluorescent	Yes, but lesser than 2-photon

LSFM is an optical fluorescent method. This implies that the specimen under test should be transparent and bio-compatible fluorophores or fluorescent molecules have to be applied to the sub-cellular features of interest. A typical LSFM system consists fundamentally of a laser source for illumination and fluorescence excitation, a cylindrical lens for generating a static light sheet, orthogonal illumination and detection axes, and specimen movement for focusing, positioning, and *z*-stack volume rendering. Movement along the *x*, *y*, and *z*-axes produces a focused specimen across the full width, positions the specimen within the objective's focal plane, and produces

serial optical sections across the specimen respectively. Fig. 2.14 shows a simple schematic of a conventional LSFM using a combination of cylindrical optics and objective lens.

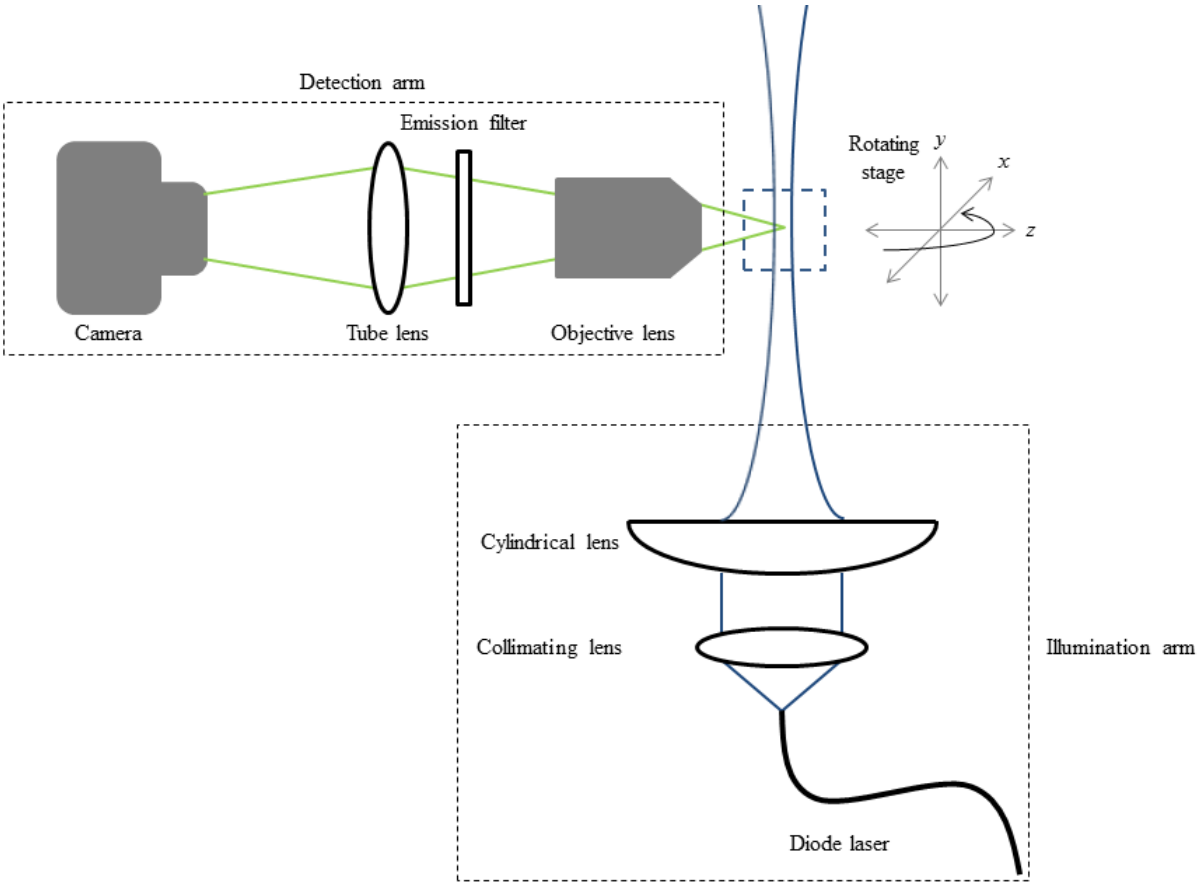

Fig. 2.14 Schematic of a conventional LSFM using cylindrical optics.

This technique was first demonstrated a century ago [88], and has evolved rapidly in recent years because of the following reasons. LSFM has the potential to overcome challenges associated with 3D live fluorescence imaging such as the need for low photobleaching and photodamage, high imaging speed, good optical sectioning capability, and cellular/ subcellular spatial resolution. Here, a thin sheet of light with a Gaussian profile is projected into the field of view (FOV) of the objective lens at the detection axis. The light sheet has minimum thickness at

the focal point, and the distance where the beam waist remains relatively constant is known as the confocal parameter b, which is given as [99]

$$b \leq |z_R| \text{ or } b = 2z_R. \tag{2.1}$$

z_R is the Rayleigh range and can be expressed as a function of beam waist radius w_0 and wavelength λ, where [99]

$$z_R = \frac{\pi w_0^2}{\lambda}. \tag{2.2}$$

Image sharpness is maximized while background noise is minimized when the light sheet is thinner than the depth of field (DOF) of the detection objective. No fluorescence is generated beyond the illumination plane and out-of-focus background is automatically rejected, giving LSFM an intrinsic optical sectioning capability. The theoretical thickness of the illumination light sheet, δ, is approximated as [23]

$$\delta = \frac{\lambda_0}{2\,NA_{ill}}, \tag{2.3}$$

where λ_0 is the wavelength of the illumination source in vacuum, and NA_{ill} is the numerical aperture of the illumination objective lens. Axial resolution of conventional LSFM, R_{LSFM}^{axial}, can be calculated using the following equation [23]

$$R_{LSFM}^{axial} = \left(\frac{1}{\delta} + \frac{n\,(1-\cos\theta_{\text{det}})}{\lambda_{fl}}\right)^{-1}, \tag{2.4}$$

where λ_{fl} is the fluorescence emission wavelength, n is the refractive index of the medium, and θ_{det} is the half angle of the light collection in the detection plane. R_{det}^{axial} is the axial resolution of the detection objective and is given as

$$R_{det}^{axial} = \frac{\lambda_{fl}}{n\,(1-\cos\theta_{\text{det}})}. \tag{2.5}$$

Clearly, from Eq. (2.3) and Eq. (2.4), a high NA_{ill} generates thinner light sheet and results in higher axial resolution. In cases where low NA lenses are used, the axial resolution is defined by the light sheet thickness [100]. Fig. 2.15 illustrates the focusing limits of high and low NA, and the trade-off between depth of focus and thickness of Gaussian light sheet.

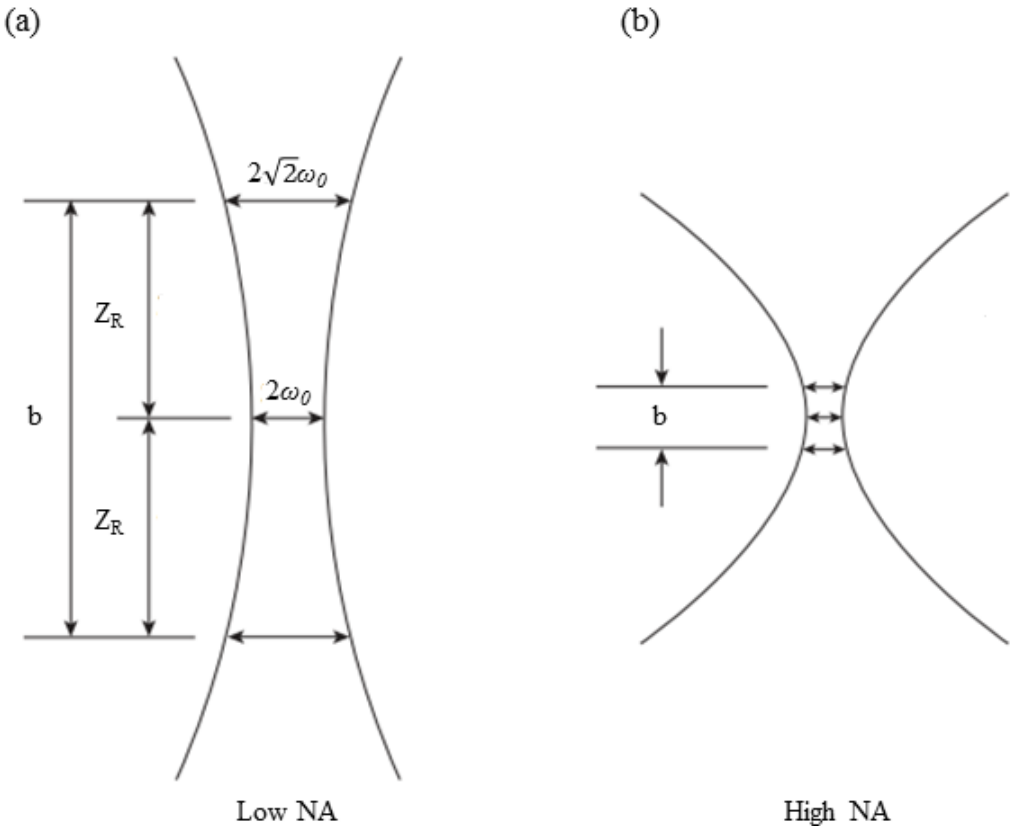

Fig. 2.15 Focusing limits, b and δ, of (a) low NA and (b) high NA objectives.

The lateral resolution of LSFM, $R_{LSFM}^{lateral}$, matches that of wide field microscopy. It is bounded by the excitation wavelength λ_{ex}, refractive index of the imaging medium n, and one-half of the angular aperture of the light cone captured by the objective lens θ. It is given by

$$R_{LSFM}^{lateral} = \frac{\lambda_{ex}}{2\, n(\sin\theta)}. \tag{2.6}$$

Since $n(\sin\theta)$ is an indication of light-gathering ability of the objective lens. The conventional diffraction limit of wide field microscopy as a function of NA is therefore [23]

$$R_{LSFM}^{lateral} = \frac{\lambda_{fl}}{2\,NA_{det}}. \tag{2.7}$$

In practice, detection objectives with low NA and large DOF are preferred for large FOV. However, it should be noted that as the thickness of the light sheet increases, resolution in the lateral direction and optical sectioning capability are compromised.

While axial resolution measures the smallest distance in the axial direction where two features can be clearly resolved where there is negligible noise, optical sectioning capability assesses the ability of the imaging system to reject out-of-focus fluorescence signal. These two parameters are related such that an increasing fluorescence signal from poor optical sections will result in an axial resolution that is lower than the ideal theoretical value given in Eq. (2.4). The axial resolution and optical sectioning capability of LSFM is defined by the convolution of conventional wide-field detection optical transfer function (OTF). The inherent disadvantage of conventional wide-field detection methodology is that the detection OTF has a "missing cone" of axial information. This results in poor optical sectioning capability and a considerable out-of-focus background. Excitation OTF of LSFM is determined by the microscope's mode of operation and the excitation beam. The OTF of the excitation plane is able to fill up this missing axial information in the detection OTF, hence enhancing the practical limit of the axial resolution and reducing out-of-focus background. One limiting factor is the deterioration of illumination quality as a result of sample-induced aberration or scattering, which undermines the image resolution. In order to achieve uniform axial resolution and optical sections, the thickness of the light sheet should be constant throughout the imaging field. From Fig. 2.15 and Eq. (2.2), it is

seen that thickness of a Gaussian light sheet varies by a factor of $\sqrt{2}$ over z_R. The diffraction phenomenon of Gaussian illuminated light sheet results in a compromise between b and δ. This sets a limitation to the axial resolution when Gaussian illumination is employed. In such cases, based on Eq. (2.4), R_{LSFM}^{axial} is dominated by R_{det}^{axial}, and subcellular features are not resolved in the axial direction. The system's resolution and optical sectioning capability can be enhanced through instrumental modifications.

In LSFM, beam-shaping apertures may be used to define the parameters of light sheet while irises and zoom optics can be used to alter its properties. However, a significant portion of the excitation light is lost at these optical components. DSLM is able to provide a flexible and high quality excitation beam using high quality optical components and a scanning approach. The advantages of DSLM over static light sheet are as follows. A virtual or digitally scanned light sheet allows more control over the intensity profile and size of the illumination sheet since the laser intensity and scan length can be digitally modulated, respectively. It should be noted that the dimensions of the light sheet, and hence the resolution, is governed by the laws of diffraction, and remains the limiting factor regardless of the light sheet generated by cylindrical optics or DSLM. Since each line in the specimen is illuminated with the same intensity, quantitative imaging is possible. The ability to scan the virtual light sheet through the specimen implies that the specimen under test can be kept at the same position throughout data acquisition for *z*-stack volume rendering. Lastly, the higher laser power in DSLM does not necessarily increase the rate of photobleaching because the integrated amount of illumination light energy used to obtain the images of the same brightness is the same [94]. Furthermore, the system operates in a linear photobleaching regime. In some implementations of LSFM, dual-sided or multi-views

illuminations [101, 102] are employed to reduce shadow artifacts and provide better illumination. 2D images acquired from the various views are combined or registered to reveal the 3D anatomy and structures that were initially occluded due to the opaque features of the specimen. Morphometric parameters can then be determined from the reconstructed rendered structures. However, it is challenging to perfectly align the light sheets in 3D space and this often result in poor optical sections that are not well focused. One promising solution to the generation of a thinner light sheet and reduction of shadowing artifacts is to employ Bessel beam [103, 104] illumination.

2.5 Outcome of literature survey

Glaucoma is also known as the "silent thief of sight" because initial vision loss is mainly peripheral and not readily noticeable. Understanding the disease state fundamentals of glaucoma is pertinent in validating the *Need Statement* that has been previously identified, and is essential for the biodesign innovation process. For example, knowledge on anatomy and physiology of the eye's drainage system helps establish a baseline against which abnormalities are understood. Pathophysiology studies how glaucoma disturbs the normal structure and function, and identifies risk factors that characterize the disease. It also allows one to understand the disease progression. Clinical presentation and clinical outcomes refer to signs and symptoms as a result of glaucoma, and hard data points that can be measured, respectively. Assessment of epidemiology reveals the incidence and prevalence of glaucoma worldwide.

The next step in innovation is then to gain an understanding on the existing and emerging treatment options, and to uncover the gap in the treatment landscape. A comprehensive profile on the assessment of glaucoma and its related parameters is developed while looking into the

effectiveness of various instrumentations in glaucoma management, and the research gap becomes apparent. Glaucoma therapeutic intervention primarily aims at the lowering of IOP and subsequent investigation into the related abnormalities in the aqueous outflow system (AOS). Hence, the ability to visualize the ICA region comprising SC, TM, and CC, in high resolution, is extremely valuable to clinicians and vision researchers towards understanding the disease condition and could allow for the effective evaluation and management of glaucoma. Current diagnostic techniques include Pentacam, gonioscopic photography, RetCam, UBM, and AS-OCTs. The current state of the art is however, unable to resolve the TM structures with high resolution. A spatial resolution of approximately 1 to 5 μm is necessary, to resolve the TM structures [105]. Two key challenges to consider are the anatomical location of TM in the anterior chamber of eye, and the phenomenon of total internal reflection at the tear-air interface. Among photographic methods, Pentacam allows non-contact, fast and easy quantification of anterior chamber parameters. However, the ICA cannot be evaluated in detail because the angle recess cannot be visualized directly. Gonioscopy remains as the clinical reference standard because it is able to make note of significant pathological findings by allowing the observation of angle structures. Imaging of ACA using Retcam gives a direct and colored image with excellent optical quality. As in the case of gonioscopy, it can give a 360° view of the ACA by imaging the four quadrants. However, it does not give quantitative information about the angle. Compression artifacts are circumvented by the fluid based optical coupling, which relieves the pressure exerted on the cornea. RetCam requires additional space for the supine positioning of patients and is more expensive compared to gonioscopy. There may also be widening of the ICA as a result of gravity on the lens-iris diaphragm. Alternative such as the gel assisted probe that can

permanently document the angle findings through digital imaging technique was also presented in this review. This technique requires further translational studies before integration into clinical ophthalmology. UBM can visualize structures behind the iris, which is important for detection of angle closure caused by iridociliary cysts. Some of the disadvantages of UBM include the requirement for contact of transducer with eye and the associated discomfort, the need for experienced personal, and the lack of standardization between scans. Conversely, the Visante OCT is easy to use and cross-sectional images of the anterior segment can be obtained. Besides, it identifies key features related to angle closure glaucoma such as increased iris thickness and area, and smaller anterior chamber width, area and volume. But time-domain OCT is time consuming and gives lower resolution images when compared to SD-OCT. Image acquisition with SD-OCT is faster, and has higher resolution which allows superior visualization of the cornea and angle, as well as the ability to image ocular substructures such as the TM, SS, and SL. Nonetheless, it is unable to get a wide FOV of the anterior segment and this makes it difficult to assess the angle recess. The next generation OCT devices will combine the advantages of both OCTs, giving an enhanced depth and field of image at higher resolution. While the OCT is clinically effective in the assessment of the ICA to indicate angle closure, and is able to image up to the micrometer scale, the spatial resolution required for imaging TM structure is still demanding because of the lack of image contrast in the acquired images. Alternatively, PA imaging method provides details that are independent of information obtained from OCT or UBM. With suitable exogenous contrast agent, this technique offers huge potential for imaging the angle region.

Despite being the gold standard for ICA evaluation and a fundamental part of eye examination, a previous study revealed that gonioscopy was not performed on 50% of glaucoma patients in clinical examination. Its main drawbacks include physician compliance and patient discomfort. Other disadvantages include the subjective interpretations of gonioscopic images, time-consuming and cumbersome procedure, and low quality images. This research project adopts a two-pronged approach to mitigate these issues. The first method explore into novel imaging technique that integrates gonioscopy whereas the second method investigate into alternative imaging techniques that provide objective evaluation. These methodologies should have good safety profile, be easy to implement, reduce image acquisition time and patient discomfort. In addition, they must be able to reveal critical details of the TM, hence providing information complementary to angle photography and gonioscopy.

Table 2.6 summarizes the challenges associated with *in vivo* imaging of eye. These challenges include cellular/ sub-cellular spatial resolution, optical sectioning capability, and imaging speed. Photobleaching and photodamage should also be considered if fluorescent molecules or fluorophores are used. Fluorescence imaging modality is a powerful imaging technique for biological sample because of its ability to specifically image sub-cellular features of interest by attaching fluorescent labels to the ROI. Intravenous, oral, or topical administration of exogenous contrast agent such as fluorescein sodium can increase the anatomical discrimination and image contrast of optical sections in eye. Amongst the imaging methodologies that make use of fluorescence contrast, wide-field imaging techniques have limitation in the in-focus and out-of-focus light. Though conventional epi-illumination laser point scanning microscopic techniques [106, 107] can image at cellular and sub-cellular

resolution and have intrinsic optical sectioning capabilities, the constant irradiation results in cumulative photodamage within the sample when taking an image stack.

Table 2.6 Challenges associated with *in vivo* imaging of eye.

Challenges	Description
Cellular/sub-cellular spatial resolution	Cellular/sub-cellular structures in the AOS require spatial resolution of a few microns/ few hundred nanometers to resolve.
Optical sectioning	Excellent optical sectioning minimizes out-of-focus background and collects images with high signal-to-noise ratio (SNR).
Imaging speed	High imaging speed that matches with spatial resolution allows sharp images of the cellular/ subcellular dynamics to be captured.
Photobleaching and photodamage	Photobleaching and photodamage should be as low as possible so that the sample can be examined over a long period of time, thus revealing the true physiological process in an undisturbed state.

In the context of corneal imaging, the subjective evaluation by slit lamp biomicroscopy is slowly giving way to new imaging technologies that are capable of performing high resolution *in vivo* imaging in research and clinical ophthalmology. Imaging techniques based on slit-scanning, Scheimpflug imaging, ultrasound, interferometry, and confocal microscopy, are capable of providing clinicians and vision researchers with qualitative and quantitative data. These imaging techniques can reconstruct the entire 3D structure of cornea from 2D cross sectional images. The generic performance metric of these reported imaging modalities are shown in Table 2.4. High resolution imaging is critical because visualization of cell morphology in an inflamed eye can give indications on the disease state fundamentals whereas an objective quantification of inflammatory cells allows proper classification of the severity of disease. High speed of acquisition reduces motion artifacts and patient discomfort. Non-contact procedures eliminate the risk of corneal abrasions and infections, and are suitable for pre- and post-operative eyes and patients with prior ocular injuries. Current clinical practice assesses cornea status through a

combination of techniques that still do not adequately visualize the layered structure. Therefore, this research project also aimed to look into potential non-contact and non-invasive optical probes for the high resolution imaging and characterization of the cornea.

This literature review critically analyzed the different optical imaging schemes based on photographic and tomographic methods for the evaluation of angle closure glaucoma and corneal diseases. Undoubtedly, there is a need for novel high resolution imaging methods for imaging the AOS and cornea that have sophisticated data analysis strategies, are non-invasive, and have similar safety profile. This review forms the platform for embarking on untapped research domains for high resolution, clinician friendly and patiently friendly device innovation. The following chapters describe the research work carried out to fulfil the objectives of this research project.

Chapter 3: Iridocorneal angle and fundus imaging with flexible ocular imaging probe

In this chapter, the methodology to design and theoretically analyze an imaging probe to evaluate the iridocorneal angle (ICA) and fundus is discussed. A strategy to achieve uniform near field irradiance with light emitting diodes (LEDs) tilted at an angle is proposed. The optimization is based on the geometric design considerations of a circular ring array of four LEDs tilted at an angle. The design equation gives insights on variable parameters such as the illumination angle of the LEDs, ring array radius, viewing angle of the LEDs, and the working distance. A micro color charged-coupled device (CCD) video camera that has sufficient resolution to resolve the ICA and fundus structures is then chosen. Contact lens assisted imaging is also presented in this chapter. The imaging capability of the developed probe and its variation are demonstrated using eye models, ex vivo porcine samples, and naturally occurring glaucoma models such as the New Zealand white rabbit and cynomolgus monkey, with high reproducibility and repeatability.

3.1 Light transmission from the anterior chamber to air

Snell's law states that when light travel from a medium of higher optical density to a medium of lower optical density, it will bend or refract away from the normal. The phenomenon of total internal reflection has to be taken into account when considering light transmission from the iridocorneal angle (ICA) region, through the cornea, to the outside medium. Under normal conditions, light from the ICA region is incident onto the tear-air interface at an angle smaller than the critical angle, and hence all of it will be reflected. Direct visualization of the ICA structures is therefore not possible. A schematic illustration of light transmission from the anterior chamber to air is shown in Fig. 3.1.

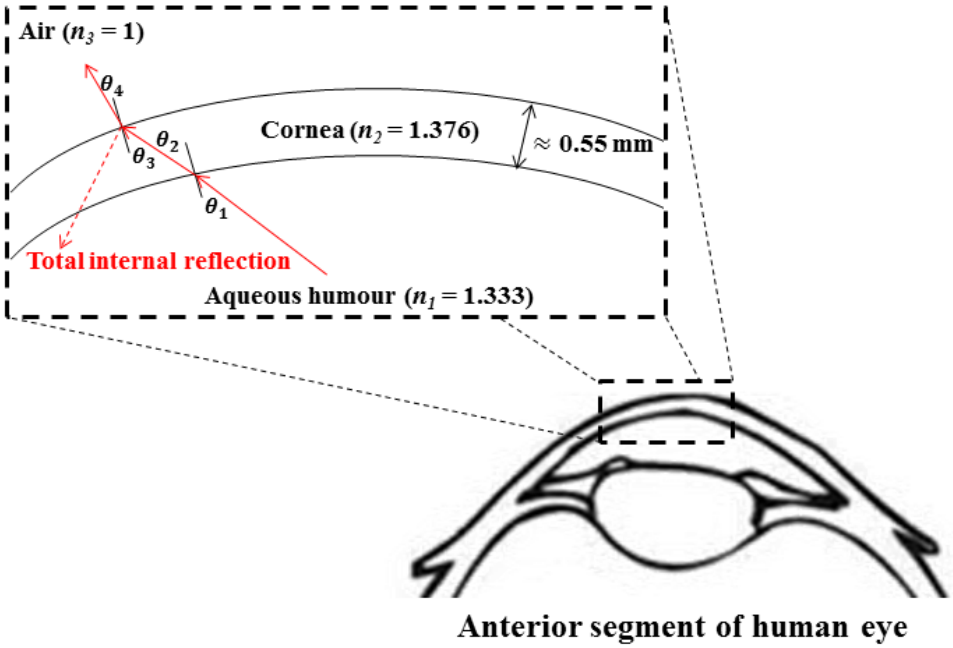

Fig. 3.1 Schematic illustration of light transmission from anterior chamber to air.

Total internal reflection at the tear-air interface can be analyzed using Snell's Law as illustrated in Fig. 3.1 where:

$$n_1 \sin\theta_1 = n_2 \sin\theta_2; \tag{3.1}$$

$$n_2 \sin\theta_3 = n_3 \sin\theta_4. \tag{3.2}$$

Here, n_1, n_2, and n_3 are the refractive indices of the aqueous humour, cornea, and air respectively. θ_1 is the angle of incident onto the posterior cornea; θ_2 is the angle of refraction in cornea; θ_3 is the angle of incident onto the anterior cornea, and θ_4 is the angle of refraction in air. Corneal thickness is comparatively small and $\theta_2 = \theta_3$. Hence,

$$\theta_3 = \sin^{-1}\left(\left(\frac{n_2}{n_3}\right)\sin\left(\sin^{-1}\left(\left(\frac{n_1}{n_2}\right)\sin\theta_1\right)\right)\right);$$

$$\theta_4 = \sin^{-1}\left(\left(\frac{n_1}{n_3}\right)\sin\theta_1\right). \tag{3.3}$$

Fig. 3.2 shows the variations in the real and imaginary values of θ_4 as a function of the incident angle on the posterior cornea, θ_1, at different values of n_3. The MATLAB® script is shown in Appendix B.

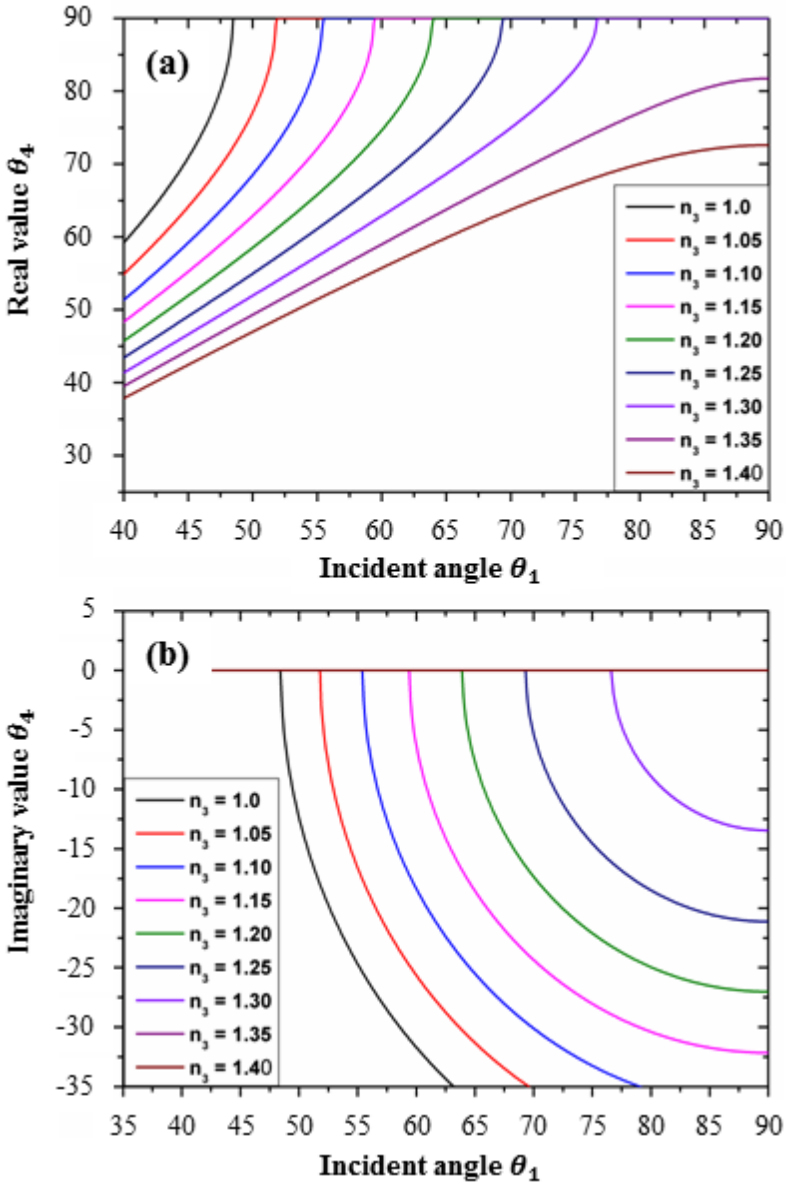

Fig. 3.2 Real and imaginary values of θ_4 as a function of θ_1 and n_3.

From Fig. 3.2, θ_1 should be around 50° to 65° in order to have a good and direct view of the ICA region. Also, when n_3 is close to or equal 1.0, total internal reflection occurs at the tear-air

interface, and θ_4 becomes imaginary. Since n_1 is a constant, total internal reflection can only be avoided by changing n_3 or θ_1.

3.2 Optical model of single light emitting diode (LED) source

There are a wide range of light emitting diodes (LEDs) with varying radiation patterns. Spherically encapsulated white light LEDs with Lambertian radiation pattern are chosen for this investigation because they emit more radiation along the optical axis. The LEDs can be approximated as imperfect Lambertian emitters since their chip size are small compared to the radius of the encapsulating lenses [108]. Hence, the irradiance distribution of such LED source in watts per meters squared ($W\ m^{-2}$), can be approximated as an imperfect Lambertian distribution function given by [108]

$$E(r, \theta_{LED}) = E_0(r) \cos^m \theta_{LED}. \tag{3.4}$$

Here, $E_0(r)$ is the on axis irradiance at distance r from the source, and θ_{LED} is the viewing angle of the LED. An ideal LED source is a perfect Lambertian emitter where $m = 1$. In this case, $E(r, \theta_{LED})$ is simply a cosine function of θ_{LED}. For an imperfect Lambertian emitter, the value m is dependent on the semiconductor region shapes and the encapsulant. The parameter m, can be expressed in terms of the half viewing angle of the LED, $\theta_{LED\,1/2}$, which is the view angle when irradiance is half of the value at 0°

$$m = \frac{-\ln 2}{\ln(\cos \theta_{LED\,1/2})}. \tag{3.5}$$

In Cartesian coordinates, the irradiance distribution over every point on a xy planar surface at distance z from the LED array is written as [109]

$$E(x, y, z) = \frac{z^m L_{LED} A_{LED}}{[(x - x_1)^2 + (y - y_1)^2 + z^2]^{(m+2)/2}}, \tag{3.6}$$

where, L_{LED} is the radiance in watts per meters squared per steradian ($W\ m^{-2}\ sr^{-1}$), and A_{LED} is the LED emitting area in meters squared (m^2). High luminous white LEDs (LM520A, Seoul Semiconductor Co., Ltd) are used for this investigation. The specifications of LM520A can be found in Appendix C.

3.3 Circular ring array of four LEDs at the desired angle

Based on the single LED model of Eq. (3.6), the irradiance of a circular ring array of four LEDs at 0° illumination angle and radius r_0 can be written as the sum of the irradiances for $N \geq 3$ LEDs [108]. Since the *z*-axis in the Cartesian coordinates is essentially the working distance, l, of the imaging system, E can be expressed as

$$E(x,y,l) = l^m L_{LED} A_{LED} \sum_{n=1}^{4} \left\{ \left[x - r_0 \cos\left(\frac{2\pi n}{4}\right) \right]^2 + \left[y - r_0 \sin\left(\frac{2\pi n}{4}\right) \right]^2 + l^2 \right\}^{-(m+2)/2}. \tag{3.7}$$

The variable r_0 can be optimized in order to achieve uniform irradiance distribution over the central region, particularly along the directions of $\cos\left(\frac{2\pi n}{4}\right)$ and $\sin\left(\frac{2\pi n}{4}\right)$. The concept here is same as the Sparrow's criterion in imaging resolution [108, 110]. The aim is to separate the irradiance patterns of the four LEDs, such that the irradiance slope variation is minimal over the central region (i.e. eliminating the implicit second-order term of Eq. (3.7)). The LED chips in the ring array should be coplanar, so that the symmetrical arrangement reduces the problem to one dimension. The maximally flat condition along the radial axis that crosses a LED can then be calculated without any loss of generality. In order to achieve the maximally flat condition [111] for r_0, E is partially differentiated twice with respect to x, and set $\frac{\partial^2 E}{\partial x^2} = 0$ at $x = 0$ and $y = 0$. Therefore,

$$r_0 = \sqrt{\frac{2}{m+2}}\, l. \tag{3.8}$$

The detailed derivation can be found in Appendix D.

It is noted from Eq. (3.8) that the maximally flat condition for r_0 is not dependent on the number of LEDs in the ring array. Eq. (3.7) and Eq. (3.8) are however not valid as practical optical model for circular ring array of LEDs at desired illumination angle. This is because the complex non-rotational symmetric irradiance pattern of the individual LEDs have to be considered. The problem can be simplified using a geometrical model shown in Fig. 3.3 where l is the working distance, r_0 is the maximally flat condition, r is the ring array radius, and α is the illumination angle.

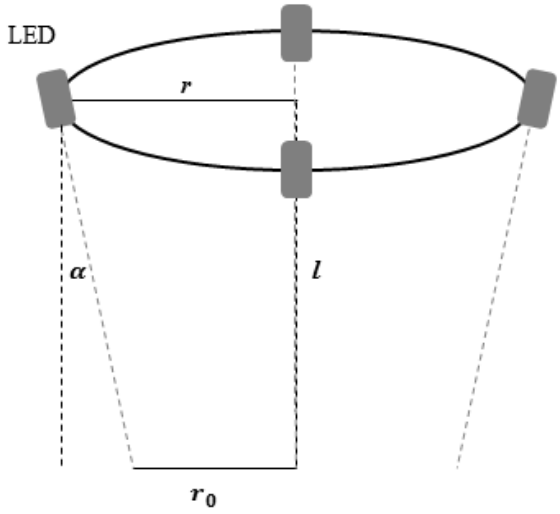

Fig. 3.3 Geometry of a circular ring array of four LEDs at desired illumination angle, α.

From Fig. 3.3,

$$\tan\alpha = \frac{(r - r_0)}{l}, \tag{3.9}$$

and by substituting r_0 from equation 8,

$$r = l\left(\tan\alpha + \sqrt{\frac{2}{m+2}}\right). \quad (3.10)$$

As seen from Eq. (3.10), the design equation for circular ring array of LEDs at an angle is bounded by four parameters α, r, and l and m. Fig. 3.4 shows plots of r as a function of α and l, at various values of m. LEDs with viewing angles of 20°, 30°, and 40° were considered for this analysis. The MATLAB® script is shown in Appendix E.

Because the viewing angle and hence m, cannot be continuously adjusted, it is more convenient to consider only three variables for optimization. Therefore, for a given value of m, the parameters α, r, and l have to be carefully considered in order to achieve uniform irradiance. The plots reveal some fundamental laws in the design of the ocular imaging probe. For example, a longer working distance corresponds to a larger ring array radius. Also, for a specific working distance, the ring array radius increases with increasing illumination angle. This increase in ring array radius is more dramatic when illumination angle is large. Taking in considerations the size of the probe, and the distance from the limbal region to the opposite ICA region, a three-dimensional (3D) model was designed and fabricated with specifications stated in Table 3.1.

Table 3.1 Critical design parameters for circular ring array of four LEDs at an angle.

Design parameters
LED viewing angle, $\theta_{LED} = 20°$
Working distance, $l = 10\ mm$
Illumination angle, $\alpha = 19°$
Ring array radius, $r = 5.5\ mm$

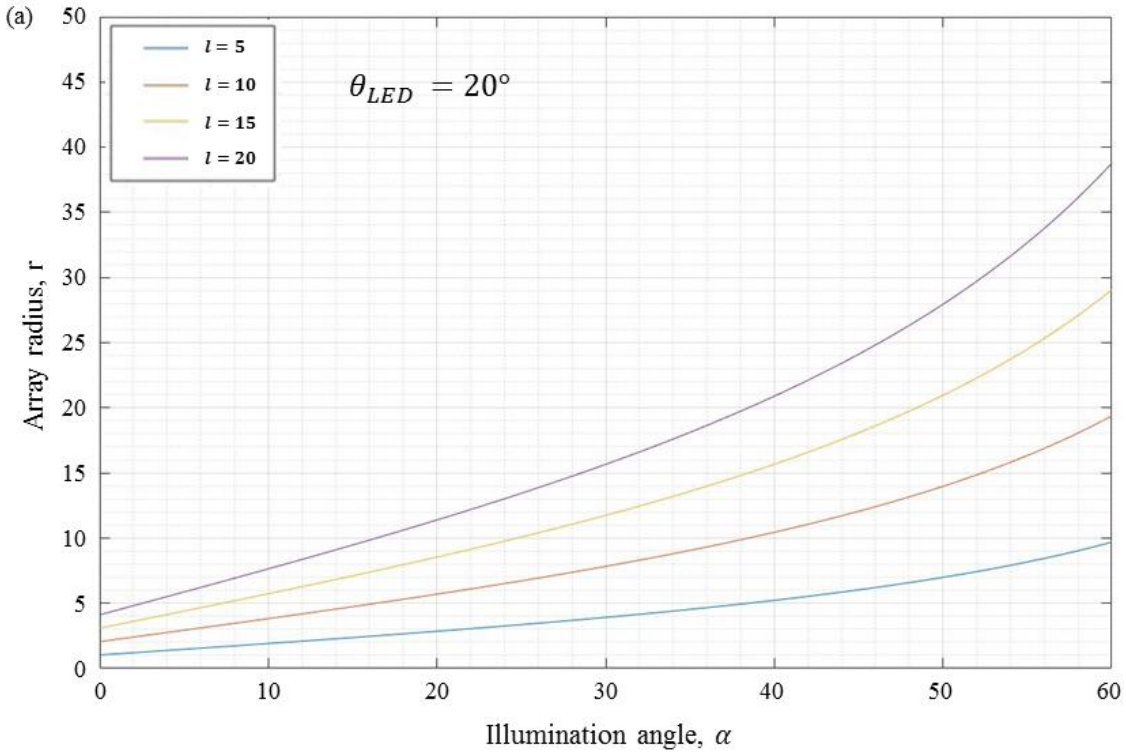
(a)
$l = 5$
$l = 10$
$l = 15$
$l = 20$
$\theta_{LED} = 20°$
Array radius, r
Illumination angle, α
0
5
10
15
20
25
30
35
40
45
50
0
10
20
30
40
50
60

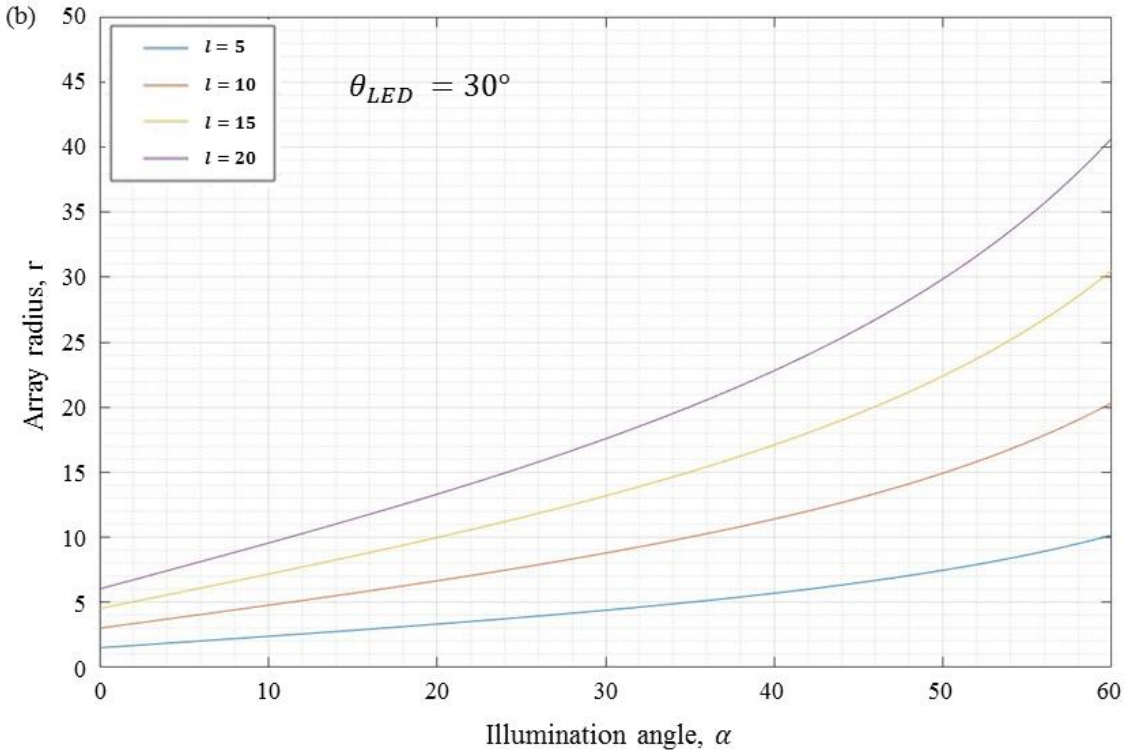
(b)
$l = 5$
$l = 10$
$l = 15$
$l = 20$
$\theta_{LED} = 30°$
Array radius, r
Illumination angle, α
0
5
10
15
20
25
30
35
40
45
50
0
10
20
30
40
50
60

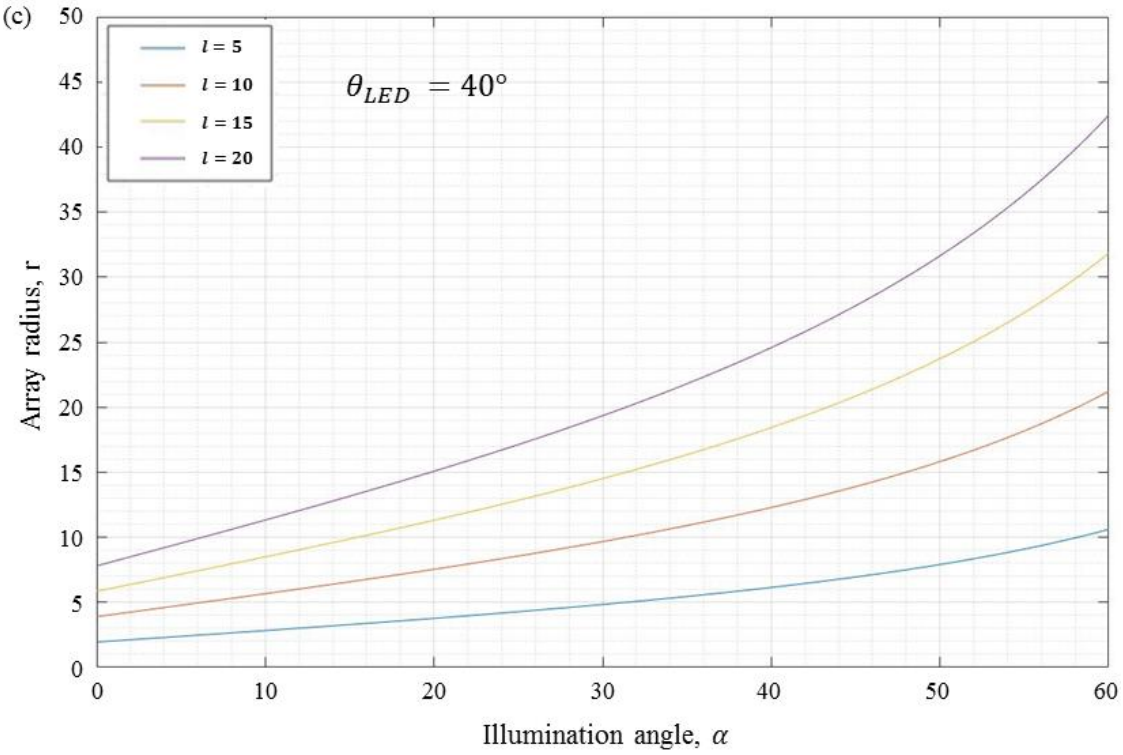

Fig. 3.4 Plot of r as a function of α and l, where θ_{LED} is (a) 20°, (b) 30°, and (c) 40°.

3.4 Selecting a suitable image capturing device

Several factors were put into considerations when selecting a suitable image capturing device. In addition to its ability to provide a direct visualization of the ICA region with good quality images, the selected camera should be compact, and be able to readily integrate into the proposed imaging probe. Since water-based ophthalmic gels or saline solutions may be used as coupling medium to overcome the phenomenon of total internal reflection at the tear-air interface, the camera should be completely waterproof. Also, to be cost effective, the camera system should be durable and suitable for reusable medical applications after high level disinfection.

Micro ScoutCam™ 3.0 charged-coupled device (CCD) camera (Medigus Ltd., Israel) was chosen as the image capturing device to record, capture, and display images of the ICA region and fundus. It is a 3.0 mm × 3.0 mm, advanced, high-end color camera that operates with a video processor. It has system

functions such as automatic gain control, brightness control, color correction, and white balance etc.. Image acquisition is possible in either single frame mode or fast kinetic series. The CCD camera has a pixel size of 2.95 μm (horizontal) × 1.90 μm (vertical), and 291,000 effective numbers of pixels (582 lateral × 500 longitudinal). It has a frame rate of 30 frames per second (fps), and a field of view (FOV) of 140° which is sufficient to capture an entire quadrant of the eye at any one time. The micro ScoutCam™ has variable resolution at different working distances. Table 3.2 shows the best achievable resolution of the micro ScoutCam™ 3.0 measured at various working distances.

Table 3.2 Resolution of micro ScoutCam™ 3.0 at various working distances.

Working distance (mm)	Resolution (lp/mm)	Resolution (μm)
5	10	50
10	8	62.5
15	5.6	89.29
20	4	125
25	3.2	156.25
30	2.8	178.57
40	2	250
50	1.6	312.5
60	1.25	400
70	1.1	454.55

The characterization was performed in free space using a USAF 1951 resolution test target. A graphical representation is shown in Fig. 3.5. The working distances at the ICA region and fundus are ~10 and 20 mm, respectively. Assuming uniform optical density of 1.33 in the anterior and posterior chambers, the CCD camera has resolutions of 10.08 line pairs per mm (~49.61 μm) at the ICA region and 5.04 line pairs per mm (~99.21 μm) at the fundus. These resolutions are sufficient to delineate the iris root (IR), ciliary body band (CBB), trabecular meshwork (TM) and scleral spur (SS) in the anterior chamber, and the arteries, veins, and optic disc in the posterior segment. Photograph of the micro ScoutCam™ 3.0 and processor are shown in Appendix F.

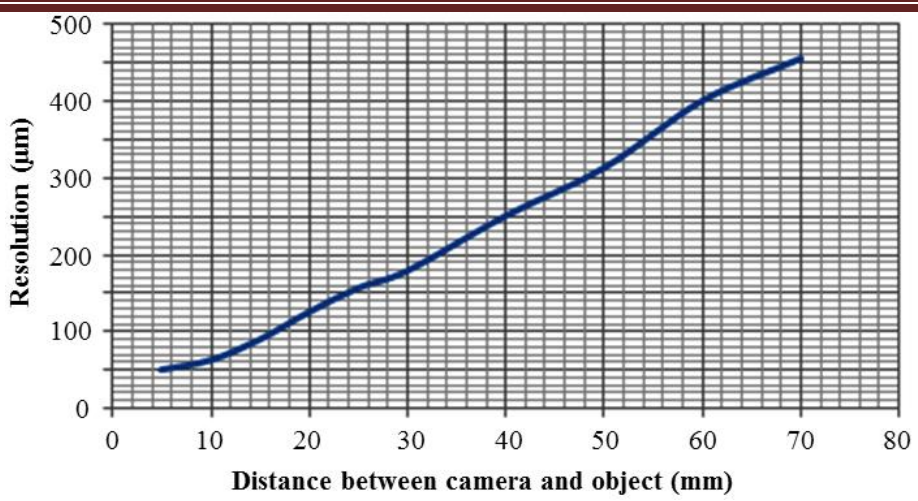

Fig. 3.5 Graphical representation of the characterization test in free space.

3.5 Assembling the imaging system

The distal end of the imaging probe is designed using computer-aided design software, SolidWorks. It is 26 mm in diameter, and has a 3 mm × 3 mm imaging conduit in the center. The imaging conduit houses the micro color CCD video camera which is coupled to a video processing unit. The video processor is in turn linked to a personal computer for display and/or for storage. The imaging conduit is surrounded by four illumination conduits. Each of the illumination conduits is fitted with a 20° viewing angle white light LED with maximum luminous intensity of 7000 mcd. The light sources are arranged in a circular ring array with a radius of 5.5 mm. The illumination conduits have internal diameters of 5 mm, and are drilled at an angle of 71° with respect to the illumination plane array, for sufficient illumination across the entire FOV. The design is based on a Lambertian approach [112] for isotropic luminescence. The design equations and formulas are adopted and derived geometrically from the design equations for a circular ring array of four LEDs at 0° illumination as discussed in the Section 3.3. A

potentiometer is employed to control the brightness of the LEDs. A schematic of the distal end of the imaging probe is shown in Fig. 3.6.

Near infrared (NIR) laser is employed in one of the probe configurations. Here, the camera is surrounded by two white light LEDs, one 20° viewing angle NIR LED with 940 nm peak emission wavelength and maximum radiant intensity of 50 nW/ sr, and a 808 nm NIR diode laser source with optical output power of 140 mW (LuxX 808, Omicron Laserage, Rodgau, Germany). The two configurations are shown in Fig. 3.7. Fig. 3.8 shows a photograph of the assembled system.

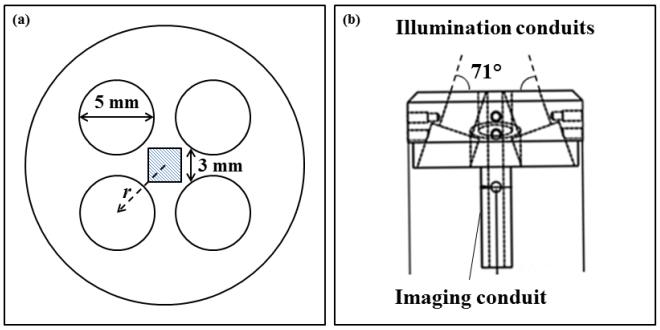

Fig. 3.6 (a) Top view and (b) side view of the imaging probe.

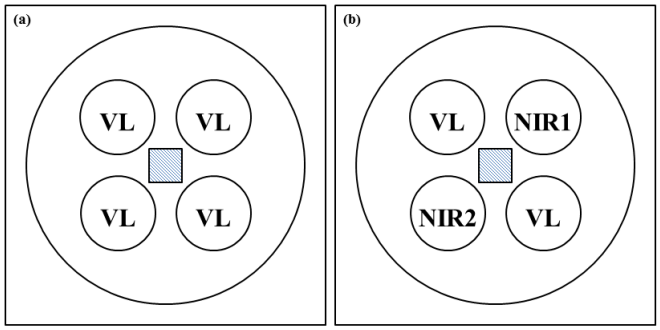

VL: White light LED where $\theta_{LED} = 40°$ and $I_V = 7000$ mcd
NIR1: 940 nm peak wavelength LED where $\theta_{LED} = 40°$ and $I_E = 50$ nW/sr
NIR2: 808 nm diode laser with optical output power of 140 mW

Fig. 3.7 Imaging probes with (a) 4 white LEDs, and (b) 2 white LEDs, 1 NIR LED, and 1 diode laser.

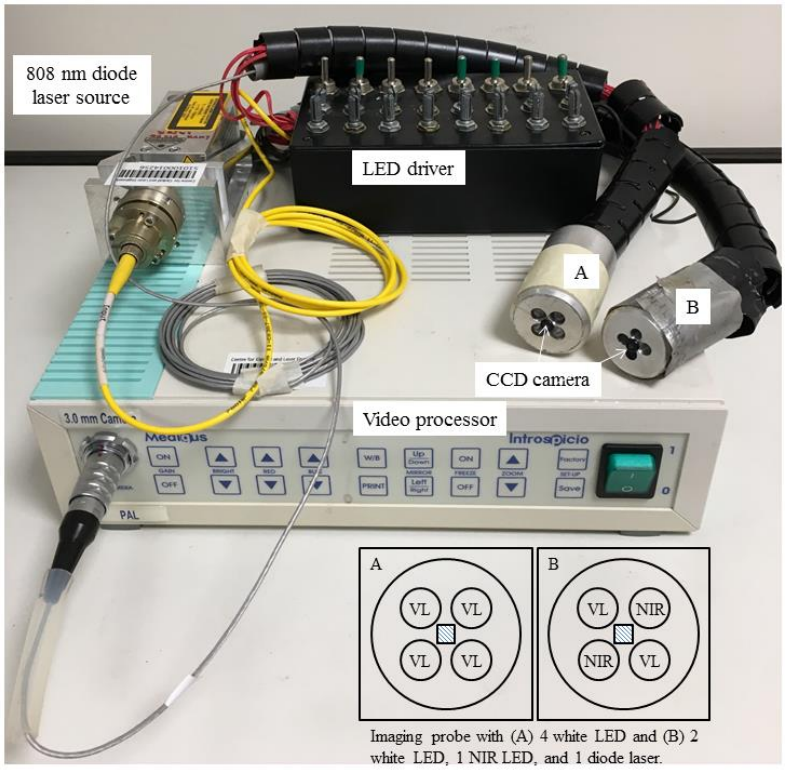

Fig. 3.8 Photograph of the assembled imaging system.

3.6 Equipment safety and maintenance

LEDs are grouped under incoherent optical sources because of their larger spectral bandwidth. Ophthalmic diagnosis with the proposed probe exposes the eye to incoherent optical radiation. Spectral details such as spectral irradiance, spectral radiance, and the angular subtense of the LED sources perceived by patients need to be considered for the correct application of exposure limits if luminance is greater than 10,000 candelas per meter squared ($cd\ m^2$) [113]. Since LM520A has a luminous intensity of 7,000 millicandela (mcd), evaluation of retina hazard is not required.

In one of the probe variations, NIR laser is employed in dark room provocation test to elicit primary angle closure. The laser beam is however not directed at the lens or retina, and exposure

is indirect and off-axis. In addition, light at this wavelength is absorbed by the vitreous humour, and only a small percentage of the incident light reaches the retina. IR-A (780-1,400 nm) is very inefficient in producing retinal injuries [114, 115]. Therefore, considering the wavelength, power, and exposure time needed for image acquisition, the exposure limit falls well within the maximum permissible limits for eye. The design of the imaging probe therefore fulfills the safety directions recommended by the International Commission on Nonionizing Radiation Protection (ICNIRP) [116]. It should however be fairly noted that there will be patient discomfort because the natural defense mechanisms of eyes' such as blinking, eye movements, glare avoidance, and squinting are compromised during image acquisition. Also, target fixation limits the movement of retina relative to the white light LED sources, and increases the concentration of radiant energy at the retina. Pupillary constriction to bright light is not inhibited since cycloplegics and mydriatics drugs are not used.

The use of hydrogel contact lens as an alternative method to overcome the phenomenon of total internal reflection at the tear-air interface, and as a better protective barrier to reduce epithelial trauma, is proposed later in this chapter. The history of contact lenses can be dated back to the da Vinci era [117]. It has evolved from a protruding contact lens, to one that was affixed with wax, to biocompatible hydrogel contact lenses for refractive error correction, therapeutic, and aesthetic purposes. Safety, vision, and comfort are the primary attributes of contact lens performances. The etafilcon A hydrogel contact lenses used in this study have a refractive index of 1.4, 70% minimum light transmittance, hydrophilic surface character, and 58% water content. These contact lenses have been cleared by regulatory bodies in terms of safety and efficacy. Like all contact procedures in ophthalmology, imaging with the flexible

ocular imaging probe creates discomfort to the patient and exposes them to risks of infections and corneal abrasions. A skilled and experienced operator is often needed and the procedure can be time-consuming. Though the use of etafilcon A hydrogel lenses as index matching medium does not eliminate the risk of infections such as microbial keratitis, the rates and severity of infections are low, and hence there is lesser risk of resultant reduction in visual acuity [118, 119]. Moreover, etafilcon A contact lenses have minimal physiological effects and a low rate of adverse events [120, 121]. Examinations similar to indentation gonioscopy can be performed safely since the hydrogel lenses double up as a protective barrier against corneal abrasions and epithelial injuries. It does not introduce any imaging artifacts, and can give good quality digital images. On comfort, these lenses are easy to apply and remove due to its hydrophilicity. All the above factors are critical, when choosing an alternative index matching medium since glaucoma is a chronic condition that requires life-long review, even after successful control of the intraocular pressure (IOP).

The flexible ocular imaging probe can be cleaned thoroughly with 75% isopropyl alcohol to remove the ophthalmic gel or saline solution before immersion in high level disinfectant solution Cidex® OPA (ortho-Phthalaldehyde). It is then rinsed with large volumes of sterile water. The illumination and imaging conduits are flushed, to ensure that the Cidex® OPA solution residues are removed completely. Sterile technique should be used during rinsing and handling. Contact lenses used in this investigation are for single use only.

3.7 Choice of animal models

Porcine eye is a suitable *ex vivo* animal model due to its high morphological similarities to that of the human eye. Furthermore, it is a validated animal model of glaucoma [122], and is

used in neuroretinal studies because of its similar retina structure to the human retina [123]. Randomly selected eyes from ten pigs (Sus scrofa domestica) were enucleated at the local abattoir and imaged within 4 hours. In order to maintain its "freshness", the enucleated eyes were transported on ice and kept till the investigation started. The conjunctivas, lacrimal gland, as well as other extra-ocular tissues were removed before fixing the eyes onto custom eye holder. The investigations with *ex vivo* porcine samples were conducted in accordance to the regulations of Agri-Food & Veterinary Authority of Singapore and Nanyang Technological University's regulations on biosafety.

The New Zealand white rabbit (Oryctolagus cuniculus) is chosen for this study because it is a naturally occurring glaucoma model [124]. The cynomolgus monkey (Macaca fascicularis) is another naturally occurring glaucoma model [125] used in this study due to its high homology and close phylogeny with humans. Their optic nerve and retinal anatomy are almost identical to that of human [126]. The *in vivo* and *ex vivo* animal models have continuous endothelial lining at the aqueous outflow channels, similar to those in human [127]. They are therefore validated models in this study.

Imaging of the New Zealand white rabbit and non-human primate were conducted in SingHealth Experimental Medicine Centre (SEMC), in accordance with the guidelines of the National Advisory Committee for Laboratory Animal Research (NACLAR) in Singapore. The New Zealand white rabbit was intra-muscularly anesthetized with xylazine (10 mg/kg) and ketamine hydrochloride (50 mg/kg) whereas the non-human primate was anesthetized with medetomidine (0.02 mg/kg) and ketamine hydrochloride (10 mg/kg).

3.8 Imaging method

The micro-CCD camera is positioned precisely at the center, so the imaging axis coincides with the central axis. A thin layer of ophthalmic gel (Vidisic Gel, Bausch & Lomb GmbH, Berlin, Germany) is applied onto the cornea. The probe is able to capture the anterior and posterior chambers of the eye when placed at the limbus or central cornea for ICA and fundus imaging, respectively. For ICA imaging, the imaging probe is positioned at the corneal limbus to image the angle in the opposite quadrant. For fundus imaging, the probe is placed at the central cornea such that the imaging axis coincides with the optical axis of the eye. The imaging schemes for ICA and fundus imaging are illustrated in Fig. 3.9(a) and 3.9(b) respectively.

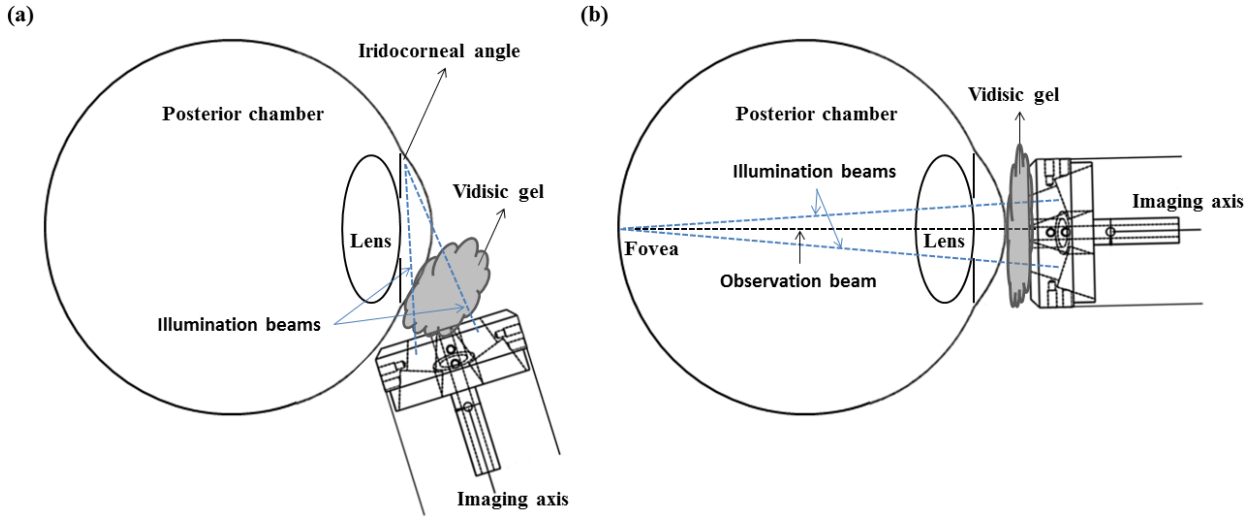

Fig. 3.9 Imaging schemes for (a) ICA and (b) fundus imaging.

3.9 Preclinical imaging of the ICA and fundus

To determine whether a patient is affected with glaucoma or to monitor the disease progression, it is necessary to undergo a series of tests. The major objectives of these tests are (i) the measurement of IOP of the eye, (ii) assessment of possible damage of the optic nerve at the

back of the eye, (iii) mapping of the complete field of vision, (iv) determination of corneal thickness, and (v) assessment of the drainage system to check for fluid in the anterior chamber of the eye [128, 129]. Unfortunately, the signs and symptoms associated with glaucoma are inconsistent among the various clinical subtypes, and may not even be presented until permanent damage has occurred. The most indicative clinical hallmarks of glaucoma are abnormalities in the AOS and optic nerve. While a wide angle allows sufficient drainage of aqueous humour through the TM, a narrow angle obstructs the flow of the aqueous humour and can eventually lead to angle-closure glaucoma. Stereo images of the optic nerve on the other hand, provide important information with regards to the cup to disc ratio, shape, and color of the optic nerve [130]. The documentations of ICA region and optic nerve are therefore critical and necessary, in the evaluation and assessment of glaucoma.

Since the direct view of the ICA is obstructed by the scleral overlap, the imaging probe is positioned at the limbal region to image the opposite ICA as illustrated in Fig. 3.9. Total internal reflection is avoided by altering the refractive index of the medium outside the cornea. Vidisic gel has a refractive index of about 1.33, very close to that of the cornea and aqueous humour. Optical distortion as a result of the corneal curvature is therefore reduced. Image acquisition is possible in single frame mode or fast kinetics mode. Since the camera has a FOV of 140°, only one image has to be taken from each quadrant, for a complete view of the ICA region. The imaging probe can visualize the anterior chamber structures in a manner similar to direct gonioscopy, making interpretation easy. The imaging capability of the ocular imaging probe is first demonstrated using an eye model (OEMI-7, Ocular Instruments Inc., Bellevue, WA, USA) shown in Fig. 3.10(a). Fig. 3.10(b) to (e) are representative images of the ICA region captured at

different quadrants of the eye model. The TM regions are indicated by the red arrows. Fundus structures can also be observed in Fig. 3.10(f). It should however be fairly noted that the circular ring array of LEDs are optimized for ICA imaging, with a 10 mm working distance. Fig. 3.11 shows the ICA and fundus images of the *ex vivo* porcine samples. Similarly, the TM regions are indicated by red arrows.

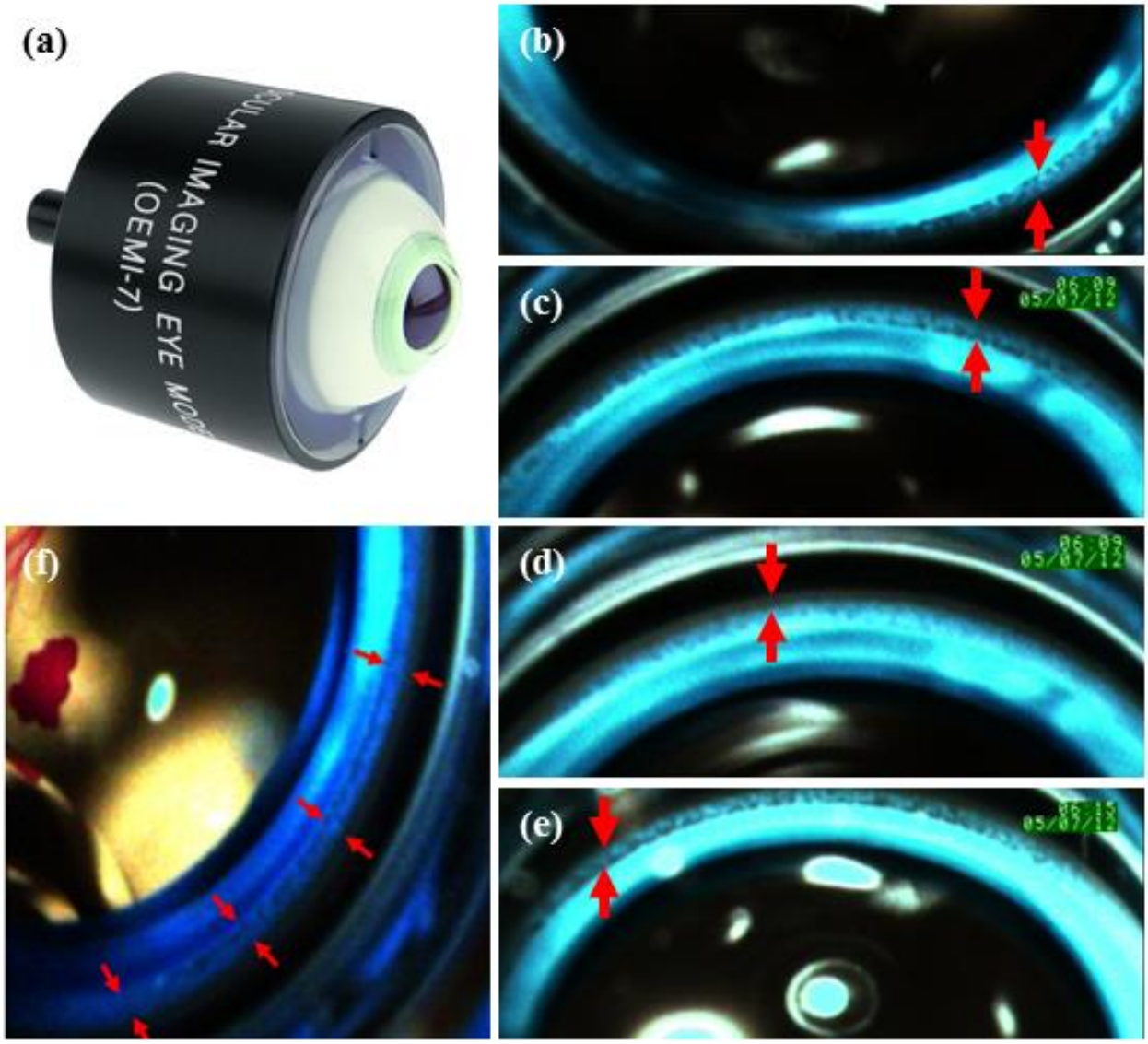

Fig. 3.10 (a) Photograph of OEMI-7. (b) – (f) Images of the ICA and fundus. TM regions are indicated by red arrows.

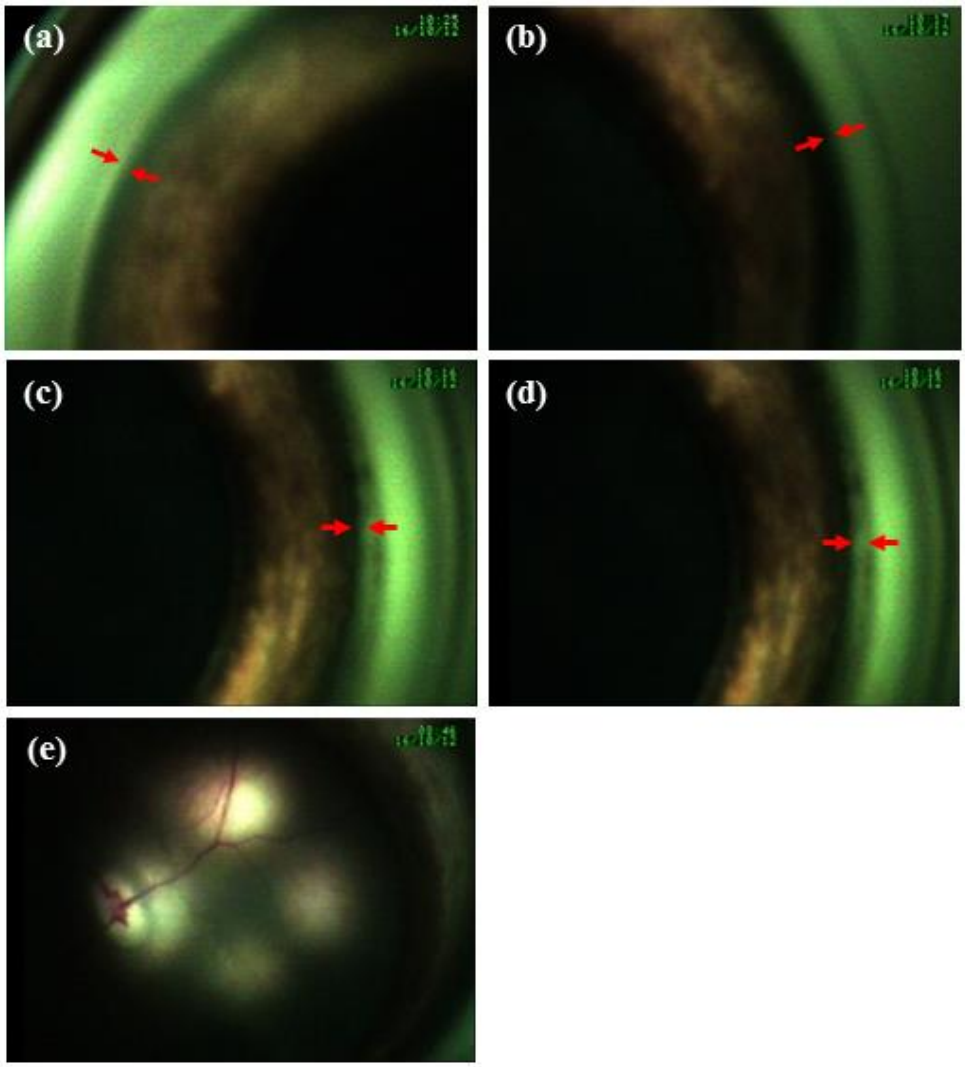

Fig. 3.11 (a) – (d) ICA images and (b) fundus image of the porcine sample. TM regions are indicated by red arrows.

The use of white light illumination causes constriction of pupils in live samples, thereby inducing an "open angle". This was however not a cause for concern with the eye model and *ex vivo* porcine samples since they will not have any change regardless of the lighting conditions. In order to increase the diagnostic precision in predicting primary angle closure in a clinical setting, it is necessary to conduct dark-room provocation test using NIR sources to elicit primary angle closure. The imaging efficiency of this dual functionality imaging system is validated by

capturing digital images of OEMI-7, *ex vivo* porcine samples, and follow-up preliminary trials on animal models, indicating promising results. The results are shown in Fig. 3.12 to Fig. 3.15.

All the *ex vivo* and *in vivo* eyes in Fig. 3.13 had anatomically open angles. Fig. 3.13 shows representative images of the ICA in a porcine sample, a New Zealand white rabbit, and a non-human primate. In contrast to the porcine sample and non-human primate eye, which are heavily pigmented, the New Zealand white rabbit has a genetic deviation knows as albinism. Nonetheless, normal iris processes can be seen reaching the SS in all the three images, indicating open angles. Fig. 3.14 (a) and (b) show the superior quadrant of the New Zealand white rabbit using white light LEDs and NIR sources, respectively. The ICA of the New Zealand white rabbit was not occluded in both cases.

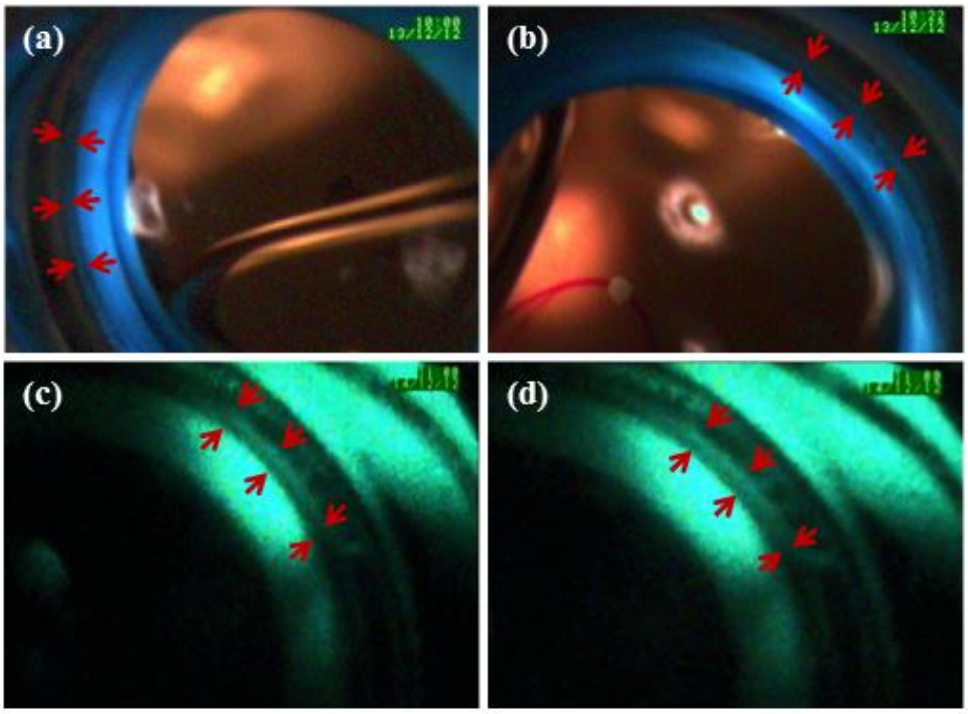

Fig. 3.12 ICA images of OEMI-7 using (a, b) LM520A and (c, d) NIR sources. TM regions are indicated by red arrows.

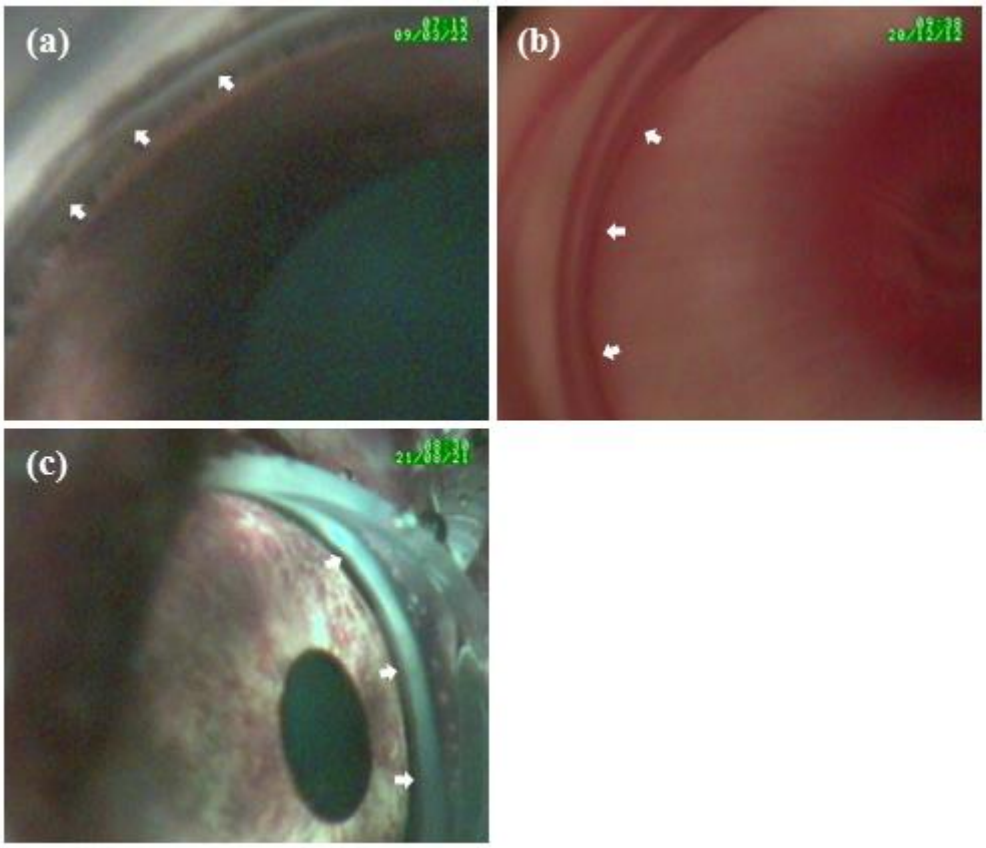

Fig. 3.13 ICA images of (a) porcine sample, (b) New Zealand white rabbit, and (c) non-human primate. TM regions are indicated by white arrows.

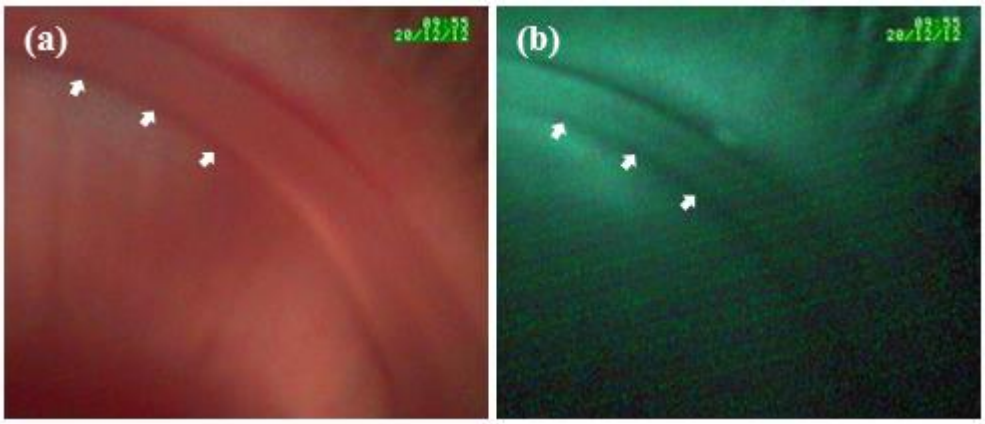

Fig. 3.14 Superior quadrant of New Zealand white rabbit using (a) LM520A and (b) NIR sources. TM regions are indicated by white arrows.

Fundus imaging with the handheld probe is similar to direct ophthalmoscopy. It is based on the principle of reversibility of light. The pupil functions as an entrance for the illuminating

LEDs and an exit for the imaging light rays. The retina and optics disc can be imaged directly enabling clinicians and vision researchers to examine the shape and color of the optic nerve. Fig. 3.15 shows fundus images of the porcine sample and New Zealand white rabbit. The arteries are relatively pale and thin, while the veins are relatively dark red and large. Interfering reflections and corneal reflection along the optical axis are significantly reduced since the trajectory of the illumination beams and observation beams are separated as shown in Fig. 3.9. The quality of the image may be degraded by media opacities. This problem can be overcome by increasing the illumination. It should be noted that there will be increased discomfort because the natural mechanisms of eyes, such as blinking, eye movements, glare avoidance, and squinting, are compromised during image acquisition.

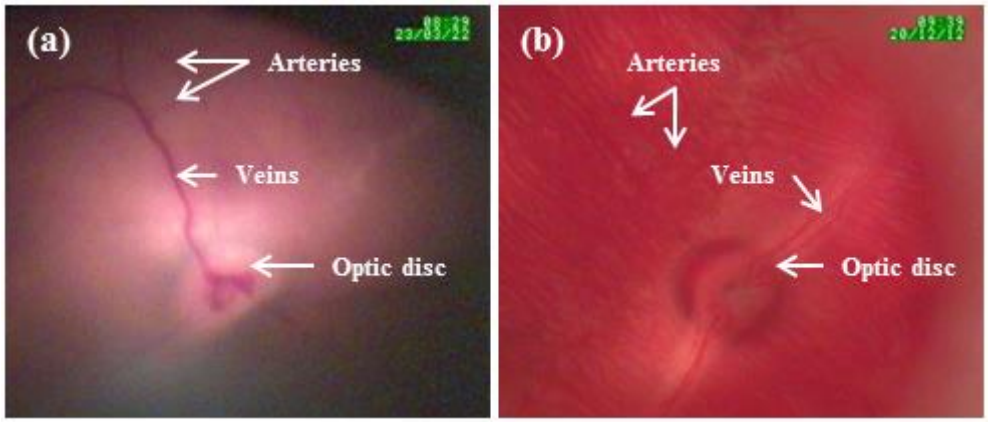

Fig. 3.15 Fundus images of the (a) porcine sample and (b) New Zealand white rabbit.

ICA region and fundus imaging with the dual functionality imaging probe take less than 2 min per eye. Unlike the EyeCam/ RetCam assessment, examination of the ICA region and fundus with the imaging probe does not require any change in the distal end optics. The upright positioning of the patients allow the images to be captured in the most natural and dynamic state. Operation of the imaging system requires minimum expertise, and the images obtained are also

similar to what is seen in gonioscopy. Critical anatomical structures of the AOS, such as the IR, CBB, TM, and SS, can be identified in a normal eye. The dual functionality imaging probe has variable resolution at different working distances. The working distances at the ICA region and fundus are ~10 and 20 mm, respectively. Assuming uniform optical density in the anterior and posterior chambers, the imaging probe has resolutions of 10.08 lp/mm (~49.61 μm) at the ICA region and 5.04 lp/mm (~99.21 μm) at the fundus. Compression artifacts are circumvented by fluid-based optical coupling.

Indentation examination is demonstrated with *ex vivo* porcine samples using contact lens assisted imaging. Here, a 8.8 mm back curvature, 14.0 mm diameter etafilcon A contact lens (Acuvue, Johnson & Johnson Vision Care Inc., Florida, USA) is positioned precisely onto the cornea of the *ex vivo* porcine samples. Similarly, the imaging probe is placed at the limbal region to image the ICA region at the opposite quadrant. The imaging scheme for contact lens assisted imaging is illustrated in Fig. 3.16. Fig. 3.17 shows images of the ICA captured with the ocular imaging probe, using the hydrogel contact lens as an index matching medium.

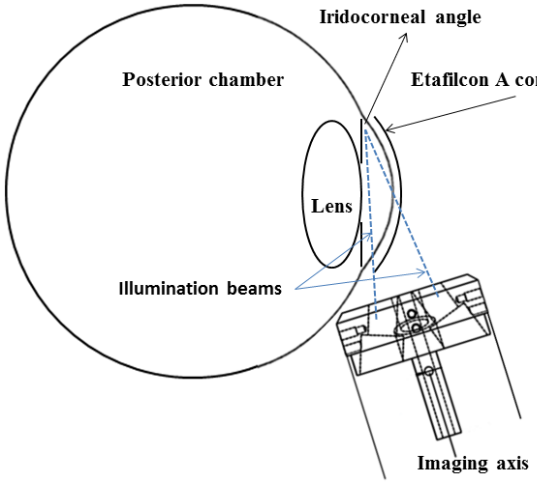

Etafilcon A contact lens properties	
Back curvature	8.8 mm
Diameter	14.0 mm
Power	− 2.50 diopters
Refractive index	1.4
Light transmittance	> 70%
Surface character	Hydrophilic
Water content	58%

Fig. 3.16 Contact lens assisted imaging for ICA imaging.

It can be seen from Fig. 3.17(a) that the normal iris processes are reaching towards the SS. This indicates an open angle. In Fig. 3.16(c), a state of high IOP was induced in the *ex vivo* porcine samples by deliberately injecting fluids into the vitreous chamber. The injection was done via a 29-gauge needle syringe. The increase in pressure caused the iris to close up towards the cornea, narrowing and occluding the ICA. Fig. 3.17(b) and (d) are indentation examinations of the eye before and after the injection. Under normal physiological conditions in Fig. 3.17(b), the iris moved readily when the cornea is indented. In Fig. 3.17(d) where angle closure glaucoma was induced, the iris is seen adhered to the cornea.

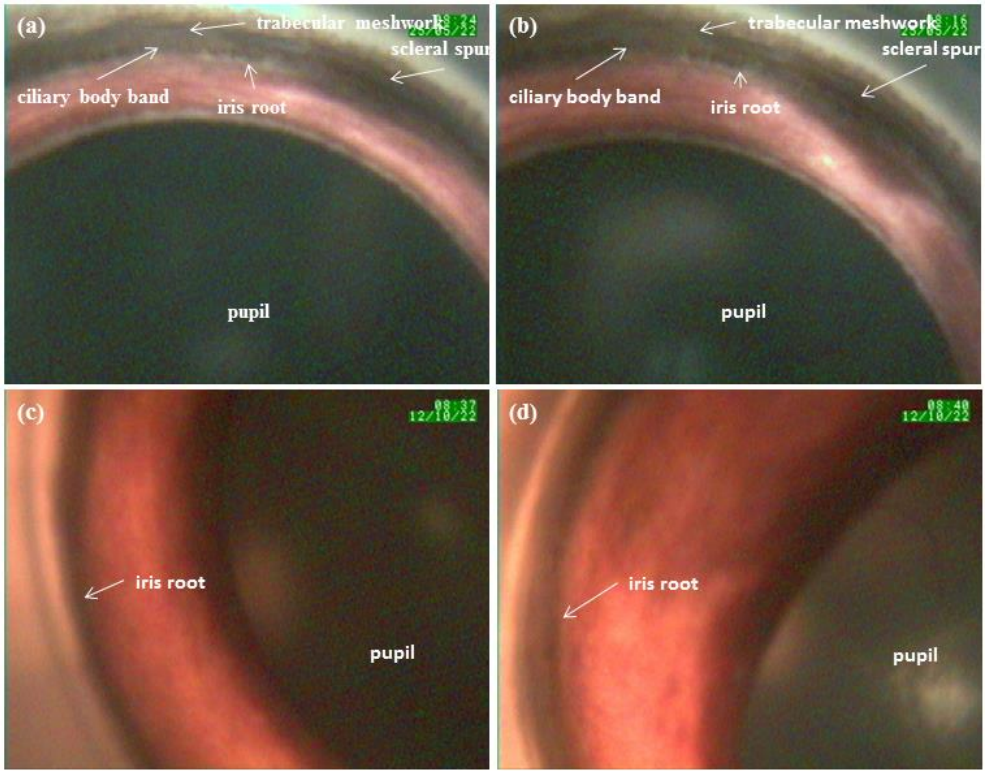

Fig. 3.17 Contact lens assisted imaging of porcine sample showing (a) an open angle and (b) indentation examination under normal physiological condition, (c) a closed angle, and (d) indentation examination after inducing high IOP.

The proposed imaging probe is able to differentiate an open angle from a closed angle. The use of NIR sources for dark room provocation test enables a predictive and objective evaluation

for detecting ICA closure. It is also able to detect pathological conditions, such as peripheral anterior synchiae, hence allowing proper classification and appropriate management. The imaging capability of the developed probe is demonstrated using an eye model and *ex vivo* porcine samples, and subsequently on naturally occurring glaucoma models, such as the New Zealand white rabbit and cynomolgus monkey. The imaging system is able to give good quality digital images of the ICA region and fundus with high repeatability and reproducibility. It reduces image acquisition time and patient discomfort compared to conventional photographic methods such as gonioscopy and RetCam. The imaging system is portable and can be attached to any workstation or even a slit-lamp, installed with the interfacing software.

3.10 Comparison of imaging systems in clinical ophthalmology

With no all-round, foolproof concept and methodology for imaging angles, clinicians tend to use individualized approach for the assessment of glaucoma. For example, some clinicians use the anterior segment optical coherence tomography (AS-OCT) as a first-pass method to detect eyes with narrow angle, as well as obtaining quantitative information about the depth of the angle before proceeding to gonioscopy. Photographic documentation allows observation of pathological changes in the ICA region and fundus over time and can be used as patient education tools to help patients better understand their conditions in clinical settings. Those with the technical capabilities choose to perform gonioscopy on all glaucoma patients since it is the fundamental part of eye examination. Despite being the current gold standard in the diagnosis and management of glaucoma, gonioscopy is a subjective method. The documentation of ICA region by gonioscopy is through various grading procedures. Its main drawbacks include physician compliance and patient discomfort [131]. Interpretations of gonioscopic images

require expertise, and are subjected to considerable disagreement between clinicians and vision researchers [132]. In addition, this procedure is time consuming and cumbersome. An earlier study revealed that gonioscopy was not performed on 50% of glaucoma patients in clinical examinations [53]. On the other hand, RetCam is a fundus camera system originally designed to capture retina images for the diagnosis and monitoring of posterior segment diseases [133]. With proper modifications, it can be used to document the anterior chamber angle [54, 134]. However, imaging of the ICA region and fundus with RetCam requires a longer time. The imaging of the ICA region and fundus takes about 5 to 10 min and 1 min per eye, respectively, and requires change of distal end optics. Moreover, the supine positioning of the patients in RetCam might cause an artifactual widening of the anterior chamber angle, resulting in underestimated measurements [135]. Skilled and experienced operators are required for gonioscopy, RetCam, and EyeCam assessments. Table 3.3 shows a comparison of imaging systems in clinical ophthalmology and the dual functionality imaging probe.

Table 3.3 Comparison with imaging systems in clinical ophthalmology.

Instrument	Fundus imaging	Iridocorneal angle imaging	Anatomical structures (anterior chamber)	Operator requirement	Patient position	Cost
Gonioscopy	No	Yes	Easy identification	Skilled, contact	Upright	Low
AS-OCT	No	Yes	Difficult	Simple, non-contact	Upright	High
RetCam/ EyeCam	Yes	Yes	Easy identification	Skilled, contact	Supine	High
Flexible ocular imaging probe	Yes	Yes	Easy identification	Simple, contact	Upright	Low

3.11 Summary

Ophthalmic instruments based on medical photographic methods enable clinicians and vision researchers to evaluate the internal drainage system of the eye, and are essential for the accurate diagnosis, prognosis, and management of glaucoma. These methods capture images of the ICA region and fundus, and store them in the patients' database. They allow the clinical documentation of anatomical changes and treatment responses with disease progression, and are also the preferred patient education tools. In this chapter, an ocular photographic imaging probe to record, capture, and display images of the ICA region and fundus is developed and illustrated. The strategy to design and optimize the ocular photographic imaging probe consisting of four LED light sources at the desired angle and an image capturing device is presented. The procedure is summarized in a flowchart shown in Fig. 3.18.

The parameters for modelling a circular ring array of LEDs at the desired angle include the LED illumination angle, ring array radius, LED viewing angle, and working distance. The design equation illustrates the relationship between these parameters, and is derived geometrically from the design equation for LED ring array at 0° illumination. For simplicity, LEDs with 20° viewing angles are used, and the working distance is set at 10 mm. Although images of reasonable quality are obtained for fundus imaging, it should be noted that the circular ring array of LEDs is not optimized for fundus imaging. One solution is to employ a pair of two linear LED arrays at 0° illumination for future prototype. This will be discussed further in Chapter 6.

The image capturing device is chosen based on its compactness, durability, and imaging capability. One limitation of the current imaging system is that the micro color CCD camera has reduced sensitivity in the NIR range. Lastly, it is important to ensure that the imaging probe

fulfils the safety directions adopted in routine clinical use as per international standards. It is envisaged that this imaging system can enable accurate diagnostic procedures of glaucoma. One of the future work directions is to extend its application to the surgical management and follow-up procedures of micro-invasive glaucoma surgeries and goniosynechiolysis.

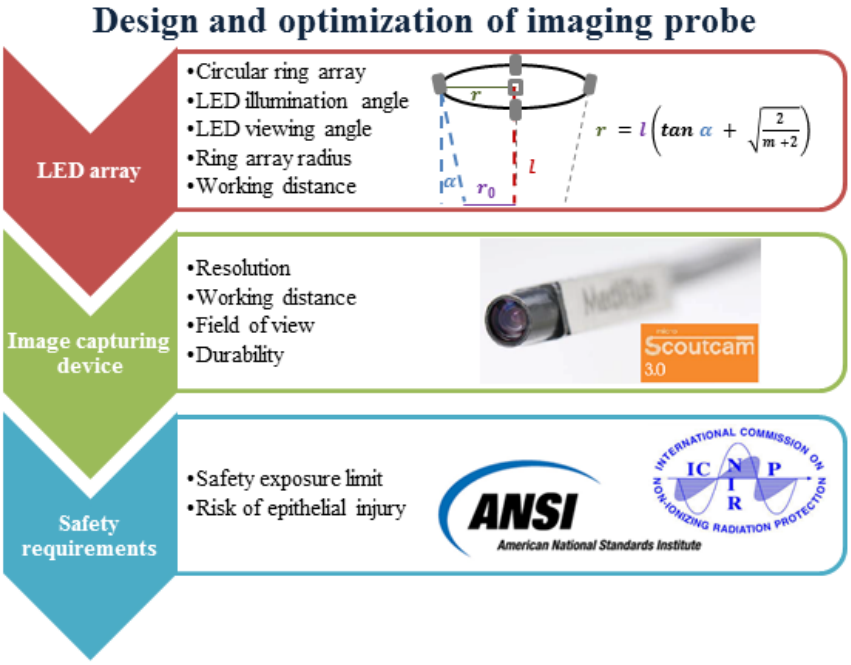

Fig. 3.18 Procedure to design and optimize the ocular photographic imaging probe.

This chapter introduces a flexible ocular imaging probe with specifications to document the ICA and fundus through digital imaging technique. While it has the potential to be used for the diagnostic monitoring of open and close angle in glaucoma patients, it does not have sufficient spatial resolution to resolve the TM structures. The following chapter explores into high resolution imaging methods such as selective plane illumination microscopy (SPIM) and a novel imaging technique that integrates gonioscopy. These imaging modalities allow the direct imaging of the TM with structural clarity.

Chapter 4: Imaging of trabecular meshwork using Gaussian and Bessel-Gauss beams

This chapter presents two imaging systems for the high resolution ex vivo studies of the aqueous outflow system (AOS) inside porcine eye, based on a Gaussian illuminated and a digitally scanned Bessel-Gauss beam light sheet fluorescence configurations. Bessel-Gauss beam is generated with the on axis illumination of an axicon lens. The digitally scanned Bessel-Gauss beam is able to overcome the trade-off between the length and thickness of the Gaussian light sheet to give better imaging performance. It has adequate spatial resolution to resolve critical anatomical structures such as the trabecular meshwork (TM), thereby enabling objective information about the AOS. This non-contact and non-invasive imaging methodology with excellent safety profile is expected to be well received by vision researchers and clinicians in the evaluation and management of glaucoma. This chapter also introduces an indirect axicon lens assisted gonioscopy imaging system using white light illumination. The proposed concepts and methodologies are validated through theoretical modelling, simulation studies, and experiments with ex vivo porcine samples.

4.1 Imaging with light sheet fluorescence microscopy

Fluorescence imaging modality is a powerful imaging technique for biological samples because of its ability to specifically image sub-cellular features of interest by attaching fluorescent labels to the region of interest (ROI) [136, 137]. Though wide field imaging techniques can also make use of fluorescence contrast, these techniques have limitation in the in-focus as well as out-of-focus light, hence creating blurred images. In order to avoid the issue with out-of-focus light, methodologies such as confocal laser scanning microscopic techniques have been established [106, 107]. These techniques create images only from the light in focus

and thus have intrinsic optical sectioning capabilities. It is also possible to image at cellular and sub-cellular level. Conventional laser point scanning microscopy employs an epi-illumination configuration, whereby the excitation and detection occur along the same axis, through the same objective lens. The constant irradiation results in cumulative photodamage within the sample when taking an image stack. For example, the excitation beam penetrates the entire sample axially when it is in focus at the focal plane, and high fluorescence background results as a consequence of the out-of-focus excitation, leading to the onset of unnecessary photobleaching and photodamage. Such is an example of the inherent problems of the epi-illumination configuration. Light sheet fluorescence microscopy (LSFM), having an orthogonal illumination and detection axes, is a promising solution to these problems. This technique has rapidly evolved in recent years because of its ability to give high resolution optical sections with minimal phototoxicity and photobleaching.

In conventional LSFM, cylindrical optics is employed to project a static sheet of excitation light onto the sample plane, and the fluorescence light emitted from the sample is collected through a microscope objective orthogonal to the illumination axis. The most obvious advantage of LSFM is the ability to generate two dimensional (2D) optical sections in large field of view (FOV), and at the same time reducing photodamage to the minimal. This is possible because the irradiation is restricted to the plane under observation [138]. The light sheet for illumination is positioned such that it is within the depth of field (DOF) of the objective lens in the detection arm. The efficiency of the illumination source is maximized because light is concentrated only at the ROI. In addition, image sharpness is improved while background noise is minimized since the specimen that is not within the objective's DOF does not contribute to the out-of-focus blur.

The high acquisition speed and low photodamage of this methodology make this technique a perfect tool for *in vivo* imaging of eye. In LSFM, the resolutions along the axial and lateral directions are decoupled and are governed by the light sheet thickness and numerical aperture (NA) of the detection objective respectively. Its imaging capability is limited by the following factors. Firstly, the broadening of the light sheet deep inside the sample as a result of the sample-induced aberration or scattering [139] increases the width of the excitation sheet and hence, decreases axial resolution. Secondly, lenses with low NA and large DOF are often used for obtaining large FOV. Conversely, this also reduces the resolution in the lateral direction and the optical sectioning capability of LSFM as the thickness of the light sheet is increased. A light sheet can also be realized by digitally scanning a Bessel-Gauss beam with a thin and long focus in one dimension [140]. In addition to its ability to generate a thinner light sheet as compared to Gaussian illumination, several research groups have also demonstrated the ability of the Bessel-Gauss beam to generate images with high signal-to-noise ratio and invariant resolution across an extended depth of focus [141, 142].

In this perspective, the following sections describe the imaging of the aqueous outflow system (AOS) inside the eye using conventional LSFM and digitally scanned Bessel-Gauss beam light sheet microscopic techniques. While the unique property of the Bessel-Gauss beam to self-reconstruct enhances the contrast of the trabecular meshwork (TM) and minimizes scattering and shadowing artifacts, the use of fluorescein sodium as a contrast agent further increases the anatomical discrimination and image contrast in the optical sections. The optical power of the imaging systems are kept within the maximum permissible exposure (MPE) limit recommended by the American National Standards Institute (ANSI) and other safety standards [113, 116, 143].

4.2 Materials

Light sheet fluorescence imaging system consists typically of the following components: a laser source for illumination and fluorescence excitation, a cylindrical lens for generating a static light sheet, a fluorescent stained specimen, orthogonal illumination and detection axes, and specimen movement to render *z*-stack volume. LSFM, being an optical fluorescent method, requires either fluorescent molecules or some fluorophores to be applied to the specimen.

An Andor Neo 5.5 scientific complementary metal-oxide semiconductor (sCMOS) (Belfast, United Kingdom) was used to image the iridocorneal angle (ICA) region, with an Omicron LuxX 488 nm diode laser (Rodgau, Germany) as an illumination source. The infinity-corrected long working distance objective lenses were purchased from Mitutoyo Corp., (Tokyo, Japan). The notch filter, NF-488-15, infinity-corrected tube lens, ITL200, visible scan lens, CLS-SL, fiber collimator, F810FC-543 were acquired from ThorLabs Inc., (Newton, New Jersey, USA). Two-axis galvanometer mirror, ProSeries PS1 Scan Heads and 176° plano-convex axicon lens were obtained from Cambridge Technology Inc., (Bedford, Massachusetts, USA) and Altechna Co. Ltd., (Vilnius, Lithuania).

All reagents used were of analytical grade. The fluorescein powder was obtained from Fluka Analytical/ Sigma-Aldrich, (St-Louis, Missouri, USA), whereas the sodium hydroxide (NaOH) pellets were from Merck, (Rahway, New Jersey, USA). All solutions were prepared using ultrapure water from the Milli-Q Synthesis A10 system.

4.3 Preparation and administration of fluorescein sodium

The *ex vivo* sample preparation is as detailed in section 3.7. A 0.2 % w/v of fluorescein solution was achieved by dissolving 0.02 g of fluorescein powder in 10 ml of 1M NaOH. The solvent was first prepared by dissolving 4 g of NaOH pellets in 100 ml of ultrapure Milli-Q water. The solution was shielded from light to prevent photobleaching. The fluorescein dye was then loaded into a sterile 29-gauge needle syringe before injecting into the anterior chamber.

4.4 Optical setup for static light sheet fluorescence

A schematic of the optical setup is presented in Fig. 4.1. The 488 nm diode laser is used as an illumination and excitation source. The laser beam is coupled into an optical fiber, and the output is collimated using a fiber collimator (NA = 0.26, f = 34.74 mm) before reaching a cylindrical lens. Here, a thin light sheet with a Gaussian beam profile is projected into the FOV of the objective lens (Plan Apo, magnification = 20X, NA = 0.42, f = 10 mm, working distance = 20 mm) at the detection axis and the reflected fluorescence signal is detected by the Andor sCMOS camera arranged in an orthogonal fashion. The NF-488-15 notch filter is used to transmit the fluorescence wavelength with little intensity loss, while attenuating the excitation source. The emitted fluorescence is imaged onto the low light sensitive sCMOS, through the infinity-corrected tube lens (f = 200 mm, working distance = 148 mm). A three axis motorized rotating stage is used to move the specimen across the light sheet. Movement along the *x*, *y*, and *z*-axes produces a focused specimen across the full width, positions the specimen within the objective's focal plane, and produces serial optical sections across the specimen respectively.

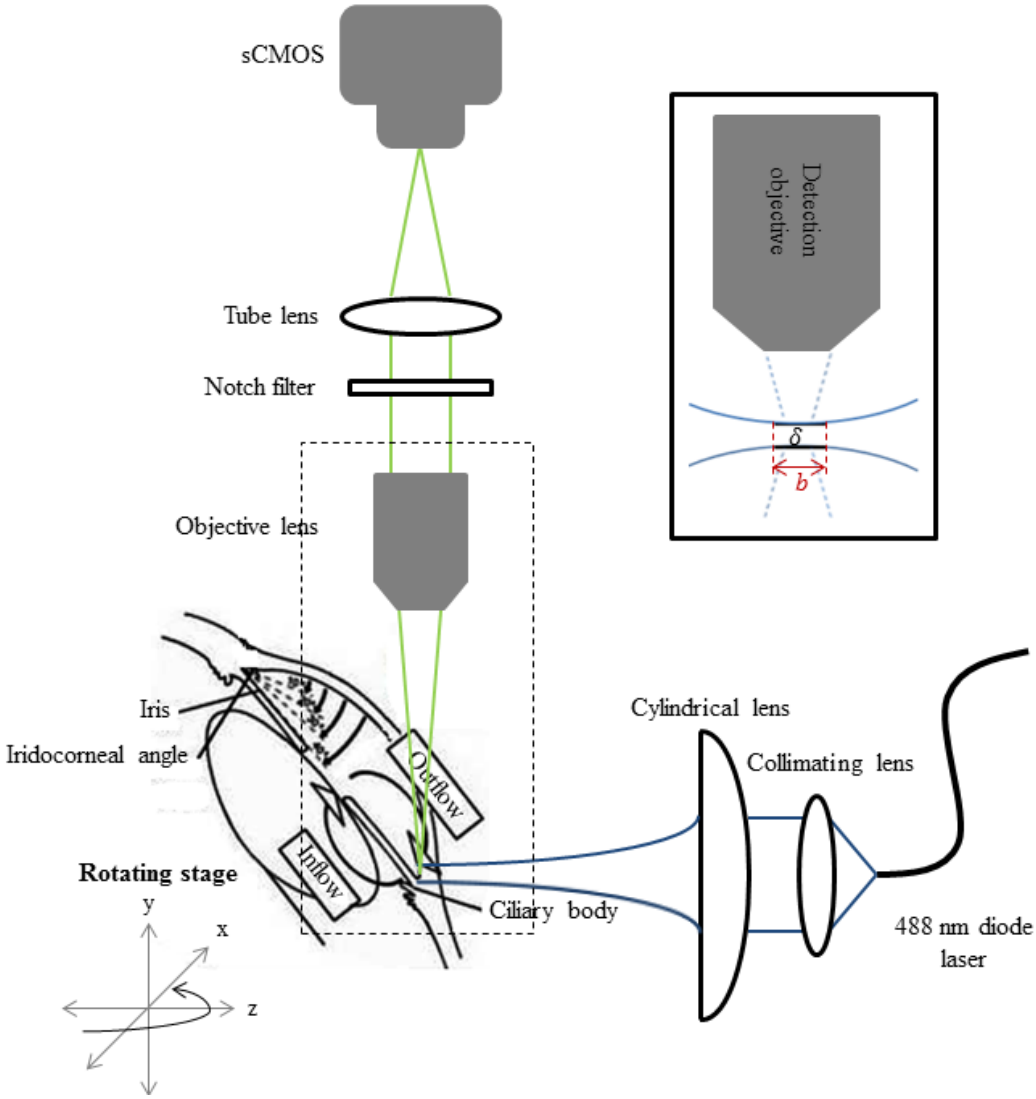

Fig. 4.1 Schematic of static Gaussian light sheet fluorescence microscopy.

4.5 Static light sheet fluorescence imaging

A lab prototype was built to demonstrate the capability of conventional LSFM and a pilot study was performed on enucleated porcine's eyes in an attempt to resolve the TM structure of the AOS. Here, a thin light sheet with a Gaussian beam profile is projected into the FOV of the objective lens at the detection axis. The minimum thickness of the light sheet is at the focal point and the confocal parameter *b*, is the distance where the beam waist remains relatively constant

[99]. An approximation for the theoretical thickness of the illumination light sheet, δ, is given as $\frac{\lambda_0}{2\,NA_{CL}}$, based on Eq. (2.3), where λ_0 is the wavelength of the illumination source in vacuum, and NA_{CL} is the numerical aperture of the cylindrical lens. The axial resolution of conventional LSFM, R_{LSFM}^{axial}, is dependent on δ and the axial resolution of the detection objective, R_{det}^{axial}. It can be calculated using Eq. (2.4) and Eq (2.5) as detailed in Chapter 2, where $R_{LSFM}^{axial} = (\frac{1}{\delta} + \frac{n\,(1-cos\,\theta_{det})}{\lambda_{fl}})^{-1}$, and $R_{det}^{axial} = \frac{\lambda_{fl}}{n\,(1-cos\,\theta_{det})}$. Here, λ_{fl} is the fluorescence emission wavelength, n is the refractive index of the medium (in this case it is the refractive index of the aqueous humour), and θ_{det} is the half angle of the light collection in the detection plane. A high NA translates to the generation of a thinner light sheet and hence, a higher axial resolution.

Out-of-focus background in LSFM is automatically rejected since no fluorescence is generated beyond the plane of illumination, giving rise to an intrinsic optical sectioning capability. The thickness of the light sheet should be constant throughout the imaging field for uniform axial resolution and optical sections. This sets a limitation when Gaussian illumination is employed, due to the phenomenon of diffraction. Since a Gaussian light sheet of $\boldsymbol{\delta}$ varies in thickness by a factor of $\boldsymbol{\sqrt{2}}$ over the Rayleigh length given by $\boldsymbol{\frac{\pi(\frac{\delta}{2})^2}{\lambda_{ill}}}$, there exists a compromise between the thickness and length of the Gaussian light sheet. The axial resolution of a conventional Gaussian illuminated LSFM is therefore dominated by $\boldsymbol{R_{det}^{axial}}$, or the DOF of the detection objective. This means that subcellular details of the TM will not be resolved in the axial direction. While zoom optics and irises can change the properties of the static light sheet, a digitally scanned light sheet offers more efficient and convenient method to adjust the height and

intensity of the light sheet. Instrumental modifications are needed to enhance the system's resolution and to maximize the optical sectioning capability.

The lateral resolution of the proposed optical setup is governed by the diffraction limit of wide field microscopy $\frac{\lambda_{fl}}{2\,NA_{det}}$, where NA_{det} is the numerical aperture of the detection objective. Experimentally, the lateral resolution is determined by the imaging of the U.S. Air Force bar target (USAF1951 chart). The proposed configuration is able to image up to group 7, element 6, of the USAF1951 chart using the 20X objective, as shown in Fig. 4.2. This corresponds to a lateral resolution of about 2.19 µm.

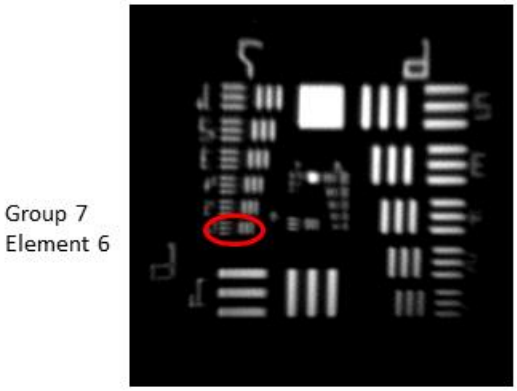

Fig. 4.2 Measurement of lateral resolution using USAF1951 chart.

Fig. 4.3(a) shows a picture of the excitation and detection through the cylindrical lens and objective lens respectively. The imaging of the ICA region is performed on fluorescein injected porcine sample and the representative result is shown in Fig. 4.3(b). The regions corresponding to the sclera, ICA and iris are denoted by S, A and I respectively.

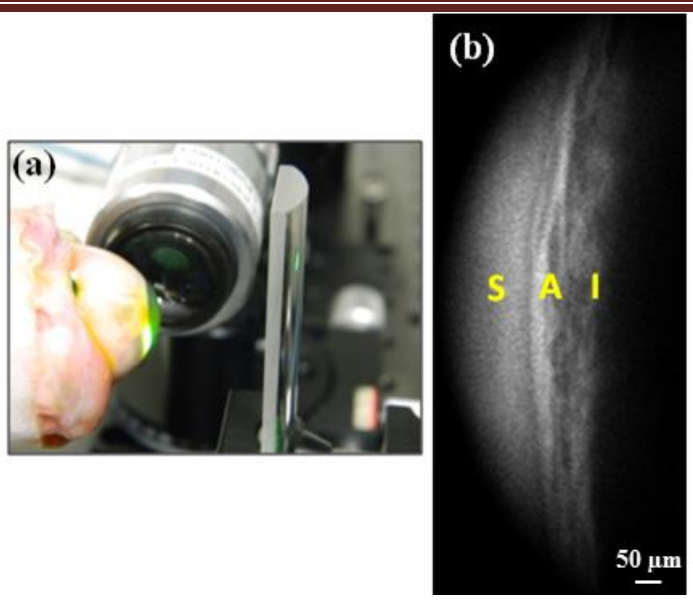

Fig. 4.3 (a) Imaging end of static LSFM, and (b) 2D image of porcine ICA.

4.6 Optical setup for Bessel-Gauss beam light sheet fluorescence

A schematic of the proposed digitally scanned Bessel-Gauss beam light sheet fluorescence imaging system is shown in Fig. 4.4. Similar to the optical setup for the static light sheet fluorescence imaging, the diode laser with emission wavelength at 488 nm is used as an illumination and excitation source to interrogate the AOS of the porcine sample, with the reflected fluorescence signal detected by the Andor sCMOS camera arranged in an orthogonal fashion. The laser beam is coupled into an optical fiber, and the output is collimated using a fiber collimator (NA = 0.26, f = 34.74 mm) before reaching the 176^0 apex angle plano-convex axicon lens. The resulting laser ring is then focused by a collimation lens onto the two-axis galvanometer mirror before passing through the visible scan lens (f = 70 mm, working distance = 54 mm), infinity-corrected tube lens (f = 200 mm, working distance = 148 mm) and infinity-corrected objective lens (Plan Apo, magnification = 20X, NA = 0.42, f = 10 mm, working distance = 20 mm) configuration. The reflected fluorescence signal from the sample is collected

by another infinity-corrected objective and tube lens configuration, with optical axes orthogonal to the illumination/ excitation arm. Objectives of the same NA are used. The second infinity-corrected tube lens is employed to focus the fluorescence signal onto the low light sensitive sCMOS. A small digital microscope (Dino-Lite Pro, AnMo Electronics Corporation, Hsinchu, Taiwan) is used to assess and document the alignment of the eye with the laser beam. The digital images of the ICA region are visualized directly on the computer screen.

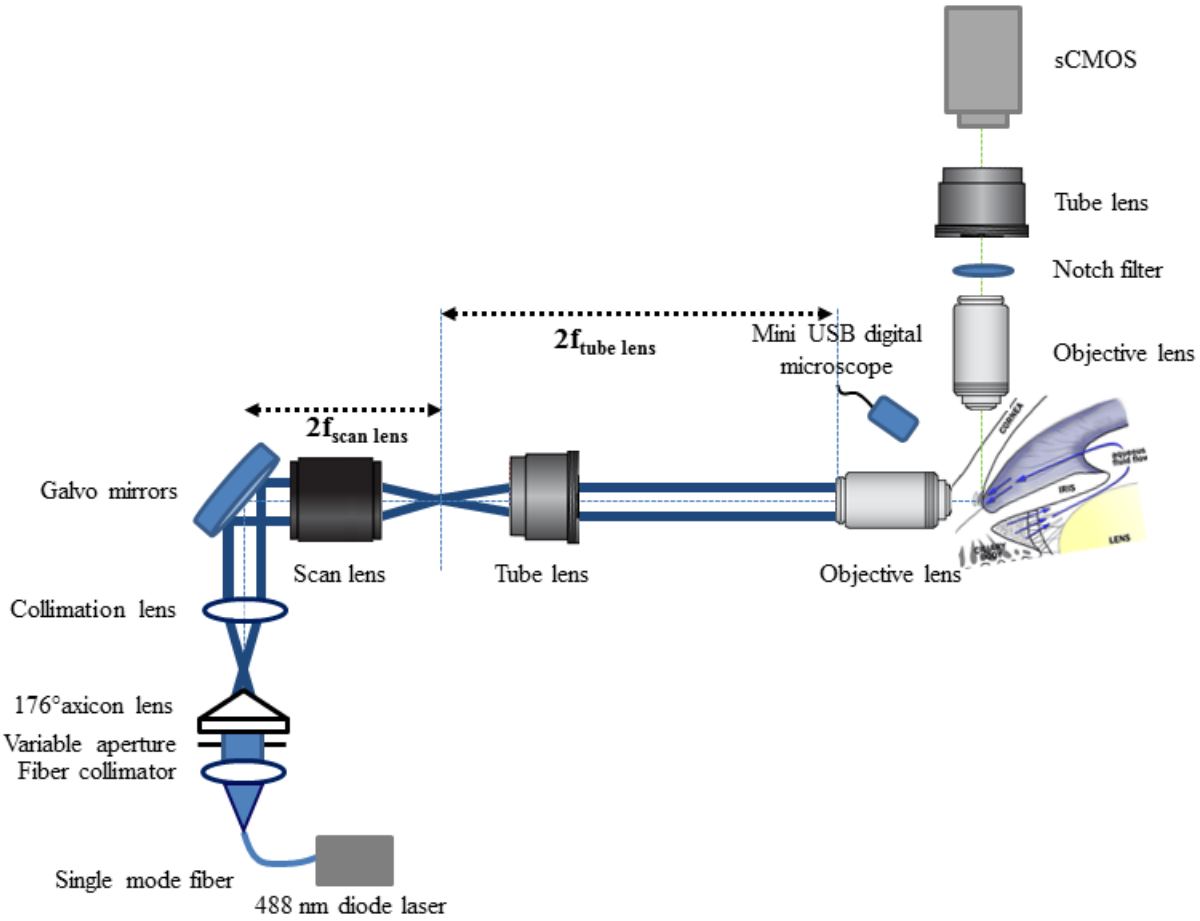

Fig. 4.4 Schematic of digitally-scanned Bessel-Gauss light sheet fluorescence system.

4.7 Generation of Bessel-Gauss beam

Unlike a spherical lens where light is focused to a point, axicon lens focuses light over a distance along the propagation axis, thereby increasing the depth of focus. Since the light energy is distributed along a range of points along the optical axis, it should be fairly noted that the optical power and contrast is reduced. The intensity distribution of the Bessel-Gauss beam upon an on axis illumination is approximately given as [144]:

$$I(r,z) = \frac{4\pi^2 E^2(R_{ill})}{\lambda}\frac{R_{ill}\sin\beta}{\cos^2\beta}J_0^2\left(\frac{2\pi r\sin\beta}{\lambda}\right), \tag{4.1}$$

where $E^2(R_{ill})$ is the energy of the incident beam, R_{ill} is the radius of the illumination beam, β is the NA of the axicon lens, and J_0 is the Bessel-Gauss beam. The axicon angle γ, β, and depth of focus Z_D, are constrained by the following equations:

$$n\sin\gamma = \sin(\gamma + \beta), \tag{4.2}$$

and

$$Z_D = R_{ill}(\cot\beta - \tan\gamma), \tag{4.3}$$

where n is the refractive index of the axicon lens. For small values of γ, Z_D can be simplified to:

$$Z_D = \frac{R_{ill}}{(n-1)\gamma}. \tag{4.4}$$

Fig. 4.5(a) illustrates the geometry of a Gaussian beam focusing to a point using a spherical lens. Fig. 4.5(b) shows a J_0 beam production using a spherical lens with an annular pupil at the back focal plane. Here, the annular pupil in the system also functions as a beam stop and limits the amount of light reaching the lens. Fig. 4.5(c) illustrates a J_0 beam production with an axicon lens, where light focuses over a distance along the propagation axis, thereby increasing the depth

of field. Fig. 4.6 shows a Zemax simulation which illustrates the linear relationship between Z_D and R_{ill}. The relationship between Z_D and R_{ill} will be discussed in the following section.

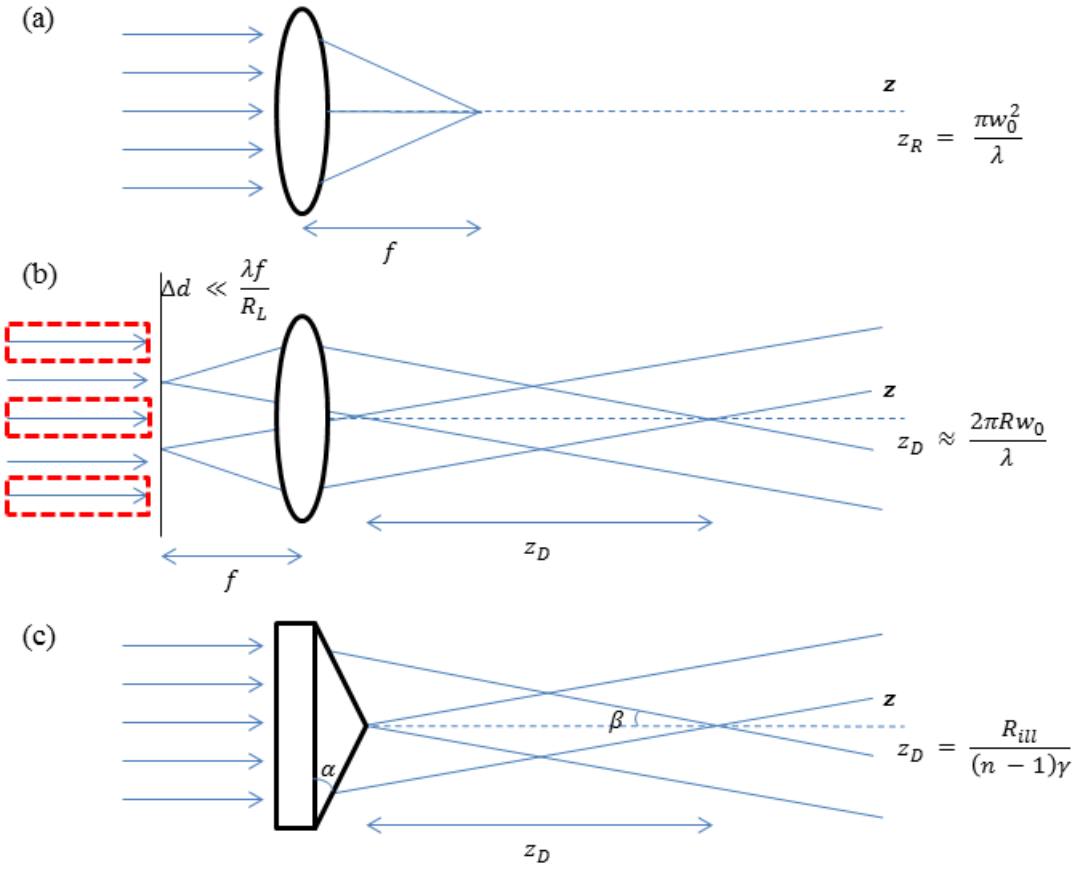

Fig. 4.5 Focusing with (a) spherical lens, (b) lens and annular pupil, and (c) axicon lens.

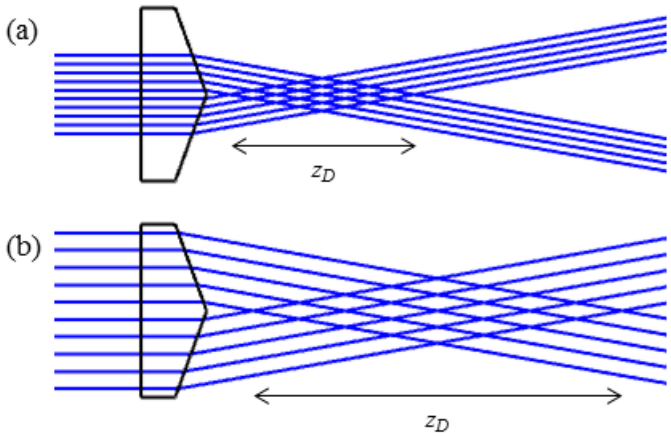

Fig. 4.6 Zemax simulation illustrating the linear relationship between Z_D and R_{ill}.

4.8 Bessel-Gauss beam light sheet fluorescence imaging

In contrast to the static light sheet optical configuration that requires lower peak intensities to reduce photodamage, a virtual or digitally scanned light sheet allows more control with respect to the intensity profile and size of the illumination sheet. Quantitative analysis of large samples in their natural and dynamic state is possible because the sample is illuminated with the same intensity at each line. It should be noted that the higher laser power in the digitally scanned light sheet fluorescence imaging does not increase the rate of photobleaching because the imaging system operates in a linear photobleaching regime. Furthermore, the integrated amount of illumination light energy used to obtain the images of the same brightness is the same [94]. Fig. 4.7 shows an illustration of the static and virtual light sheet.

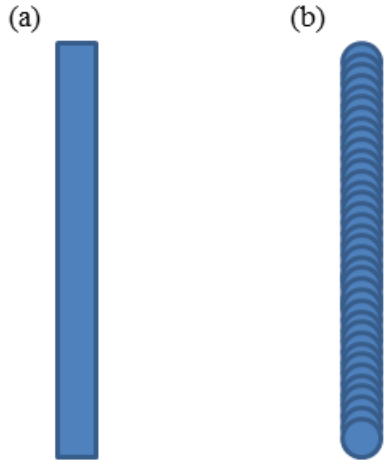

Fig. 4.7 Illustration of (a) static and (b) digitally-scanned light sheet.

The optical components in the detection axis are similar to that in static light sheet microscopy arrangement. In the illumination axis however, several additional components are required: a plano-convex axicon lens and a collimation lens for the generation and focusing of the Bessel-Gauss beam respectively; a two-axis galvanometer for the scanning mechanism to

sweep the focused Bessel-Gauss beam; a visible scan lens and infinity-corrected tube lens combination arranged in a 4F configuration to relay the scan plane of a laser scanning imaging system to the back aperture of the illumination objective; and a long working distance objective lens in place of the cylindrical lens.

To overcome the limitation of the Gaussian illuminated light sheet, a Bessel-Gauss beam is generated with the on axis illumination of an axicon lens. This method of generating a Bessel-Gauss beam is more efficient in generating an annular pattern compared to the illumination of an annular pupil of finite width due to the absence of a beam stop [145]. This in turn translates to higher illumination efficiency and hence, a lower exposure time which minimizes photobleaching and photodamage. It should be noted that beyond the depth of focus, Z_D, of the Bessel-Gauss beam, also known as the beam length, the rays of light become an expanded ring. The scan lens and tube lens are arranged in a 4F configuration such that the rays will alternate between the beam phase and the ring phase as shown in Fig. 4.8. Z_D in the proposed optical setup is regulated by a variable aperture before the axicon surface and can be approximated by Eq. (4.4). For a given NA_{ill}, the larger the R_{ill}, the greater the Z_D, and the more energy exists in the side lobes and vice versa. In other words, the Bessel-like characteristics and hence the length of the output beam is linear with the aperture radius. The thickness of the virtual light sheet is proportional to $\frac{\lambda_0}{2\,NA_{ill}}$, where NA_{ill} is the NA of the illumination objective. One important factor for consideration in this imaging scheme is therefore to project a beam that can sufficiently and precisely cover the region of interest. Otherwise, the increased side lobes energy will also result in an increased in excitation tails on either side of the central core, thereby decreasing the overall axial resolution and image quality.

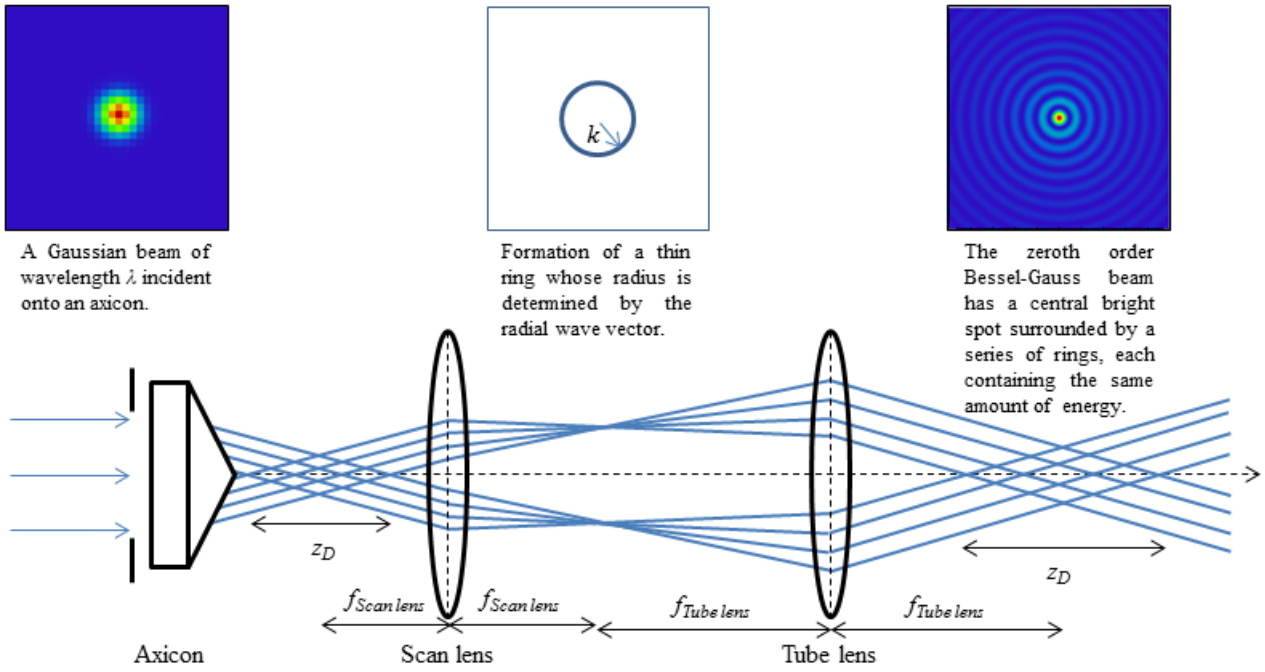

Fig. 4.8 Generation and propagation of Bessel-Gauss beam with Zemax.

The galvanometer mirror sweeps the focused Bessel-Gauss beam in the *y*-direction to generate a digitally scanned or virtual light sheet for fluorescein excitation. The Bessel-Gauss light sheet is positioned within the DOF of the detection objective lens as shown in Fig. 4.9. Fig. 4.9 also shows a comparison of relative intensity (amplitude squared) cross section and relative radial intensity between a digitally scanned Gaussian beam and a Bessel-Gauss beam. The Zemax simulation shows that Bessel-Gauss beam has a longer depth of focus and a central peak that is narrower than Gaussian beam. It can overcome the trade-off between the thickness and length of the Gaussian light sheet. The fluorescence threshold responses should be higher than the peak strengths of the side lobes, in order to enhance the anatomical discrimination and image contrast of the optical slices. 2D optical sections with large FOV are possible as the irradiation is restricted to the plane under observation and fluorescence is imaged across the entire excitation plane simultaneously. The parallelization of image collection on the Andor Neo sCMOS camera

allows high image acquisition speed and hence reduces photodamage. The imaging schematic for Bessel-Gauss light sheet fluorescence imaging is shown in Fig. 4.10.

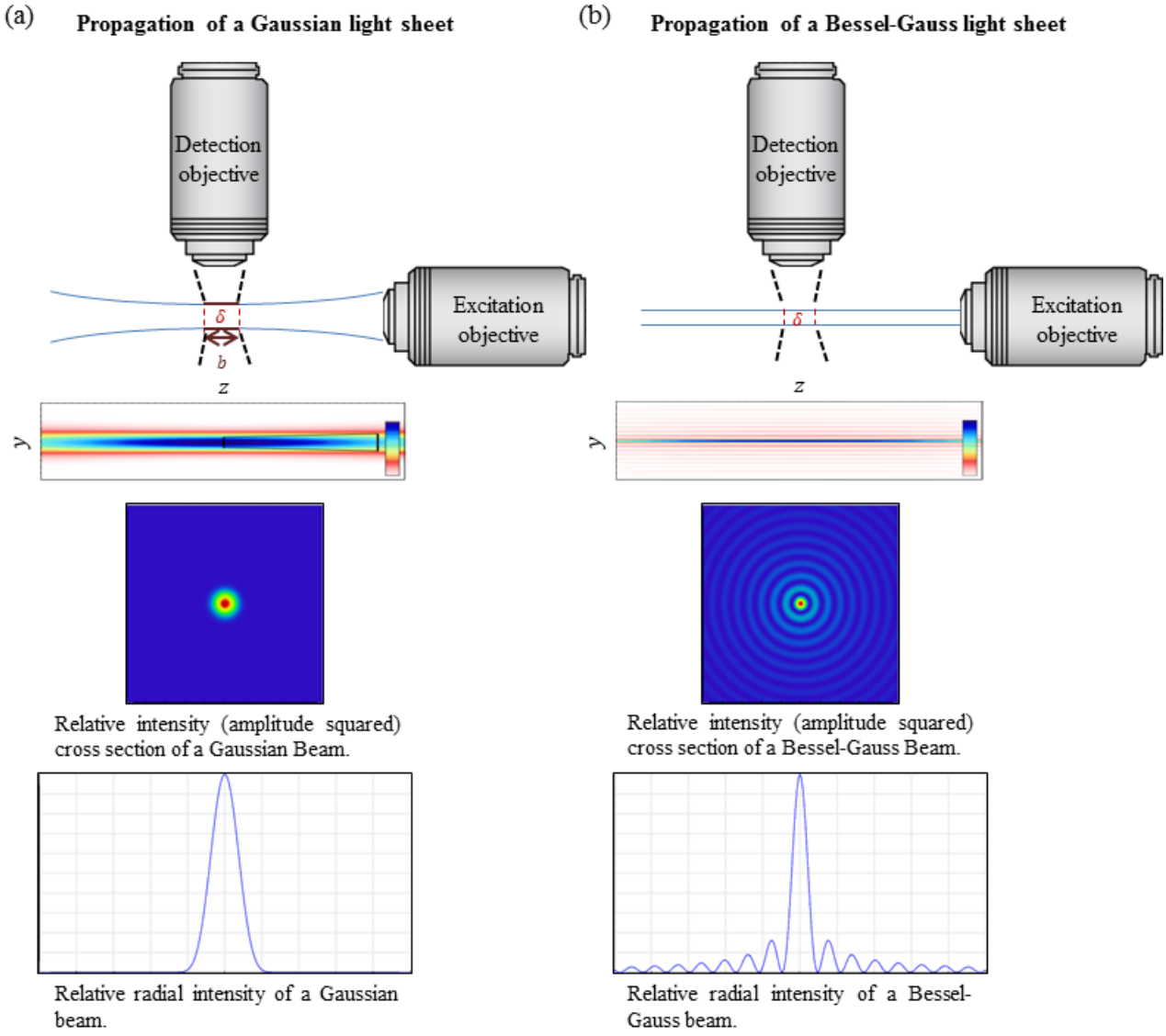

Fig. 4.9 Propagation of digitally scanned (a) Gaussian and (b) Bessel-Gauss light sheet.

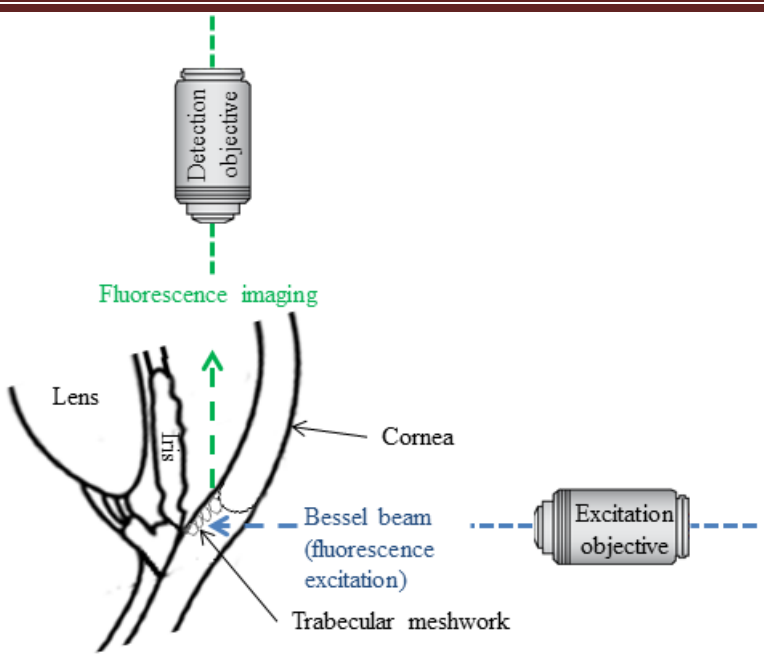

Fig. 4.10 Imaging schematic for Bessel-Gauss light sheet fluorescence imaging.

Both the proposed configurations use the Andor Neo sCMOS camera which operates at wide dynamic range, high sensitivity, and rapid full frame rates. The high dynamic range of the sCMOS camera allows image deconvolution to enhance resolution [146] and time-lapse imaging. High sensitivity is correlated with high signal-to-noise ratio, while rapid frame rates allow dynamic information to be captured with high temporal resolution. Since the 5.5 megapixel sensor is more than sufficient to capture the desired ROI, the FOV is traded off for an enhanced temporal resolution. An array size of 512 × 512 was pre-selected, with a rolling shutter mode and global (snapshot) shutter mode of 412 frames s^{-1} and 200 frames s^{-1}.

The imaging result obtained from the ICA region using this optical imaging configuration is shown in Fig. 4.11(a). A better representation of the ROI is shown in Fig. 4.11(b), where the image is digitally processed by finding edges and adjusting the brightness and contrast. Compared to the image from the Gaussian illuminated light sheet in Fig. 4.3(b), this optical setup is more efficient in the examination of

the AOS, as it can resolve the TM structures with higher resolution in the axial direction. The higher axial resolution of this prototype is due to the thinner light sheet, and the ability of the Bessel-Gauss beam to reconstruct through scattering media. Images acquired are in sharp focus since the light sheet is thinner than the DOF of the detection objective. The unique ability of the Bessel-Gauss beam to reconstruct itself increases the image contrast at the TM, and minimizes the scattering and shadowing artifacts [147, 148]. The lateral resolution on the other hand, is governed by the diffraction limit of wide field microscopy, and is the same as that in the static light sheet fluorescence imaging configuration. The results obtained clearly present a network of collagen fibers in a meshwork fashion, and the dimensional information is in good agreement with histological measurements performed by previous study group [57]. More translational studies with other established methodologies are required, to determine whether the proposed system will complement existing imaging modalities in a clinical setting, so as to improve the effectiveness of subsequent treatment and to decrease morbidity.

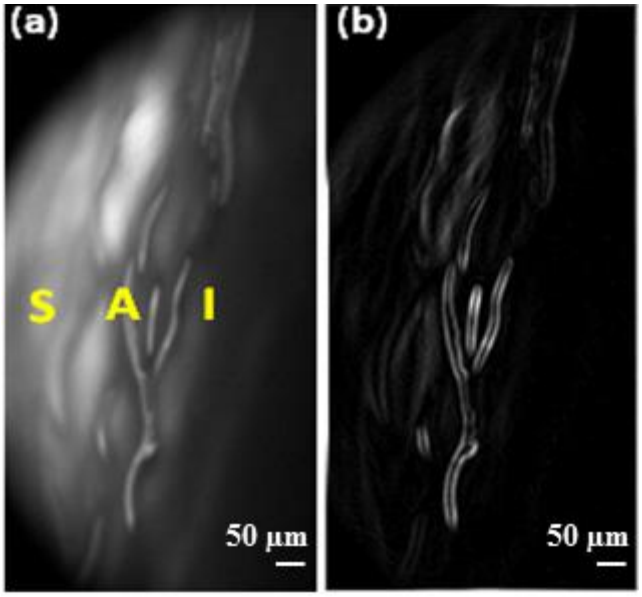

Fig 4.11 (a) 2D image of *ex vivo* porcine ICA and (b) the processed image.

To date, light sheet microscopy and its various configurations have been established widely in developmental biology [137, 146, 149]. This is the first application of light sheet microscopic technique in the field of ophthalmology. In human, fluorescein administration can be performed intravenously via injection into the peripheral vein. The normal adult dosage should not exceed 500 mg, whereas dosage for pediatric patients must be adjusted according to their body weight [150]. Fluorescence intensity in the circulation is greatly reduced due to the binding of fluorescein molecules to plasma proteins [151]. The free fluorescein molecules which contribute to the emission are excited with 488 nm diode laser. Alternatively, 2 % Minims Fluorescein Sodium solution, (Chauvin Pharmaceuticals Ltd, Romford, United Kingdom) can be applied as eye drops. The fluorescein molecule will diffuse through the cornea, into the anterior chamber. The dye can be metabolized by the kidneys, and will be excreted through urine 24 to 36 hours after administration.

4.9 Comparison of imaging systems in clinical ophthalmology

The long working distance objectives allow the non-contact and non-invasive approach in imaging the TM and this gives an added advantage to the proposed system as compared to gonioscopy and other contact based methodology for anterior chamber angle interrogation. Table 4.1 shows a comparison of imaging systems in clinical ophthalmology and the proposed configurations. The upright positioning of the eye and the non-contact nature of the procedure suggest that there are little distortions to the eye anatomy, and the ICA region can be viewed in its natural and dynamic states. The use of laser illumination in the visible wavelength range however, will cause the constriction of pupil in a live sample, thereby inducing an “open angle”. This was however not a cause for concern with the *ex vivo* porcine samples since they will not have any change regardless of the lighting conditions. The proposed prototype does not require

much expertise to operate, since there is no requirement for any coupling medium or complicated sample preparation that will expose the animal/ patient to risk of corneal abrasion and infections. In contrast to ultrasound biomicroscopy (UBM), RetCam™ and gonioscopy, this procedure is therefore suitable for both pre- and post-operative eyes, and for patients with prior ocular injuries.

Table 4.1 Comparison with imaging systems in clinical ophthalmology.

Instrument	**Scan source**	**Measuring principle**	**Axial Resolution**	**Lateral Resolution**	**Coupling medium**	**Patient position**	**Operator requirement**
OCTs	SLD 840nm – 1310 nm	Interferometry	5-25 µm	15-100 µm	No	Upright	Simple, non-contact
UBM	Ultrasound (50 Mhz)	Ultrasound	25 µm	50 µm	Yes	Supine	Skilled, contact
RetCam™	White light	Direct ophthalmoscopy	N.A.	N.A.	Yes	Supine	Skilled, contact
Gonioscopy	White light	Total internal reflection	N.A.	N.A.	Yes	Upright	Skilled, contact
Gaussian beam LSFM	488 nm diode laser	LSFM	> 6 µm	2.19 µm	No	Upright	Simple, non-contact
Bessel-Gauss beam LSFM	488 nm diode laser	LSFM	> 0.5 µm	2.19 µm	No	Upright	Simple, non-contact

4.10 Axicon lens assisted gonioscopy

An axicon lens assisted gonioscopy imaging system is also conceptualized and developed in this chapter. This imaging system integrates the concept of Bessel beam microscopy with conventional gonioscopy imaging. The combination of an axicon lens and a refocusing lens placed at a focal length away from the imaging plane transforms the point spread function of the imaging system into a pseudo Bessel beam with super-resolution imaging capability. The Bessel beam microscopy configuration is validated experimentally by performing spatial resolution characterization tests. Its imaging capability is compared against classical Gaussian systems. More information can be found in Appendix G.

4.10.1 Optical modelling of axicon lens assisted gonioscopy

The three dimensional (3D) representation and schematic illustration of the optical setup for the axicon lens assisted gonioscopy imaging system is shown in Fig. 4.12.

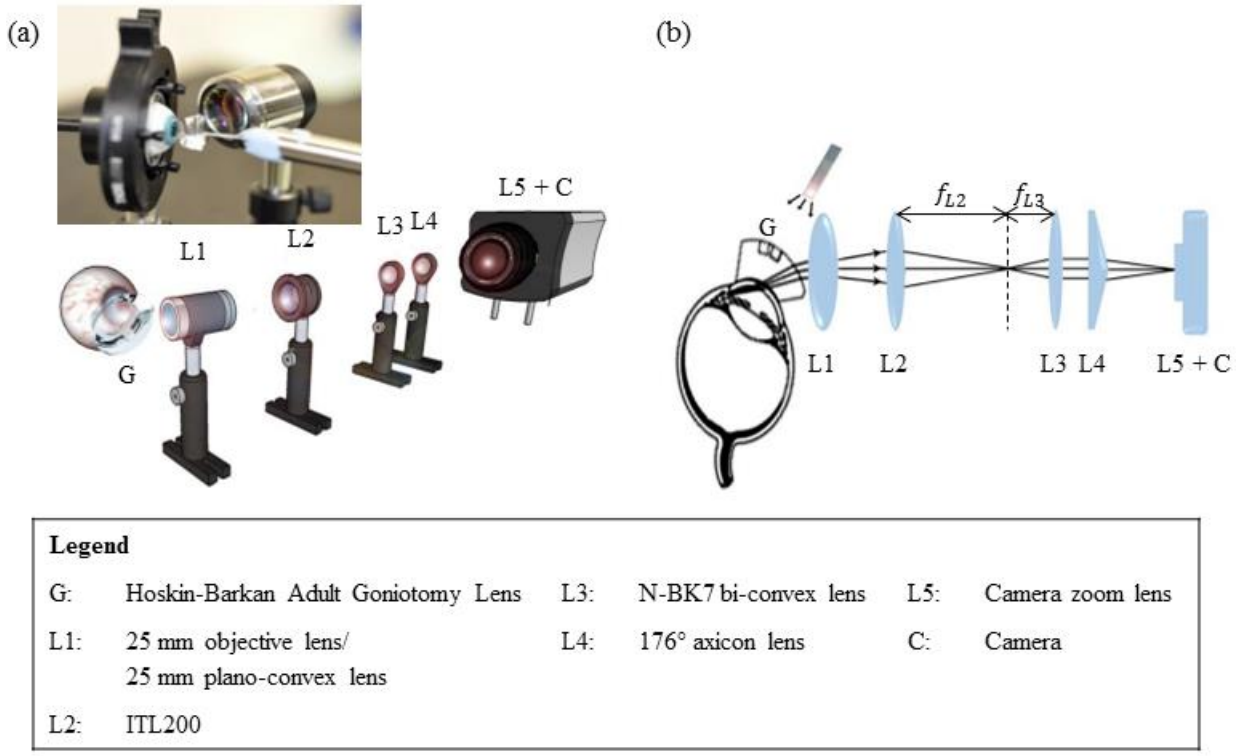

Legend					
G:	Hoskin-Barkan Adult Goniotomy Lens	L3:	N-BK7 bi-convex lens	L5:	Camera zoom lens
L1:	25 mm objective lens/ 25 mm plano-convex lens	L4:	176° axicon lens	C:	Camera
L2:	ITL200				

Fig 4.12 (a) 3D representation and (b) schematic of axicon lens assisted gonioscopy.

For the theoretical modelling, a 25 mm focal length plano-convex lens is used in place of the objective lens (LSM03-VIS, ThorLabs Inc., NJ, USA). ITL200 and N-BK7 bi-convex lens (LB1844-A ThorLabs Inc., NJ, USA) are separated by a distance equal to 197.1 mm, which is the sum of the working distance of ITL200 (148 mm) and the back focal length of N-BK7 bi-convex lens (49.1 mm). The 176° apex angle plano-convex axicon lens is placed in close proximity to N-BK7 bi-convex lens to minimize loss of light. After the axicon lens, the interference pattern generates a pseudo-Bessel beam with an extended depth of focus. The charged-coupled device (CCD) camera (EXi Aqua Bio-Imaging Microscopy Camera, Q

Imaging, Surrey, BC, Canada) can be positioned anywhere within Z_D. For accurate optical modelling of the axicon lens assisted gonioscopy, it is necessary to consider the contribution and behavior of the eye as part of the optical system. Information on the simulated goniotomy lens and eye model can be found in Appendix H. A point source is placed at the anterior chamber of the eye to simulate light transmission from the anterior chamber of the eye. For imaging, a white light source (Correct Shimadzu FA-150EN Fiber Illuminator, Japan) is used for illumination. A thin layer of ophthalmic coupling gel is applied onto the cornea to reduce refractive index mismatch at the tear-air interface.

Fig. 4.13 shows the Zemax optical simulation model of the axicon lens assisted gonioscopy. The Huygens point spread functions (PSFs) are analyzed and the surface PSF and false color PSF are shown. In another simulation, the N-BK7 bi-convex lens and axicon lens are removed. In this case, the image plane is 148 mm away from the 25 mm focal length plano-convex lens. The optical simulation model, Huygens surface PSF, and false color PSF are shown in Fig. 4.14. PSF grids are also shown for both configurations. The aim is to study the differences between axicon lens assisted gonioscopy and conventional gonioscopy. The simulations are performed with two point sources that are 3 μm apart along the *y*-axis. From the results, it is evident that the axicon lens assisted gonioscopy imaging system has a higher spatial resolution compared to the conventional gonioscopy imaging system. It can clearly distinguish the closely spaced points as two entities, rather than one. The conventional gonioscopy model is unable to differentiate between the two closely spaced points.

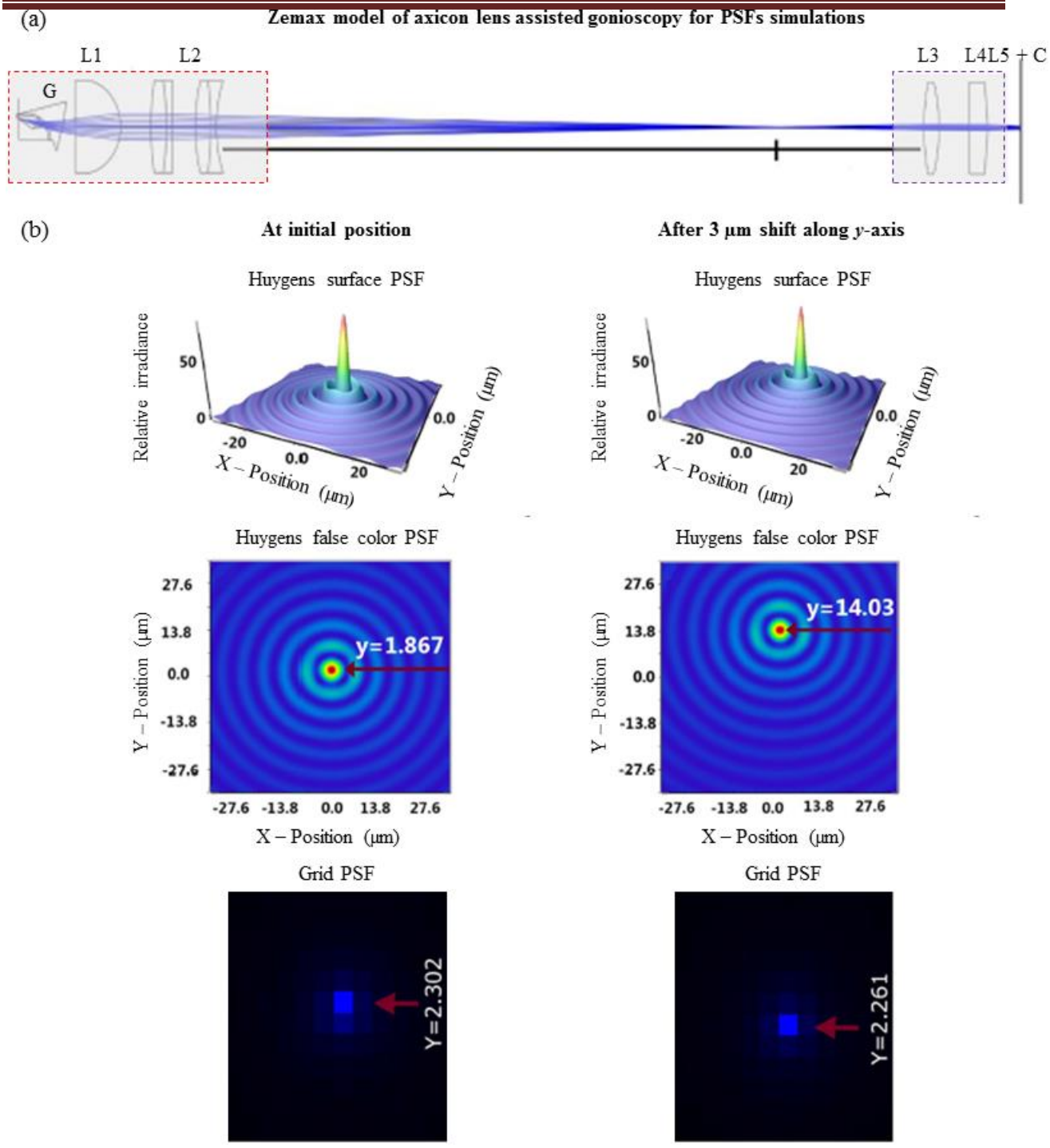

Fig. 4.13 (a) Zemax model of axicon lens assisted gonioscopy and its (b) Huygens surface PSFs, false color PSFs, and PSF grids before and after 3 µm shift along *y*-axis.

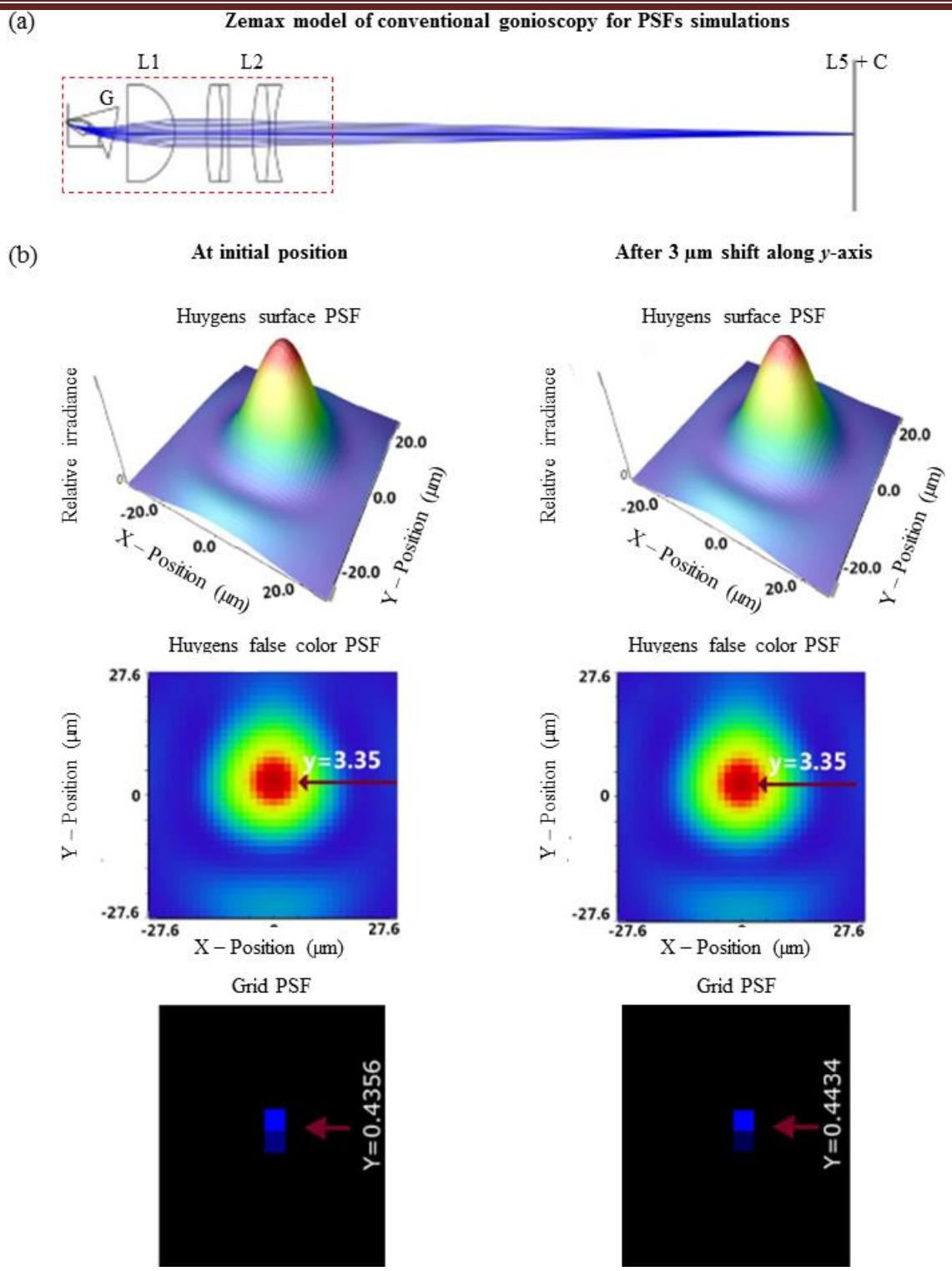

Fig. 4.14 (a) Zemax model of conventional gonioscopy and its (b) Huygens surface PSFs, false color PSFs, and PSF grids before and after 3 µm shift along *y*-axis.

4.10.2 Spatial resolution characterization test

Spatial resolution characterization tests are conducted for the axicon lens assisted gonioscopy and conventional gonioscopy imaging systems. The experimental setup is as shown in Fig. 4.12, except that USAF1951 chart is used in place of the eye model. The axicon lens assisted gonioscopy imaging system is able to image up to group 7, element 4 of the USAF1951 chart resolution test target, which corresponds to a line thickness of 2.76 μm. In comparison, the conventional gonioscopy imaging system is only able to image up to group 6, element 2 of the USAF1951 resolution test target. This corresponds to a line thickness of 6.96 μm. The results are shown in Fig. 4.15. It is noted that the axicon lens assisted gonioscopy imaging system has reduced resolving capability compared to the Bessel-beam microscopy configuration in Appendix G. This can be attributed to significant scattering and Fresnel reflection as a result of the steep angle of incidence on the surface of the gonioscopic lens [105].

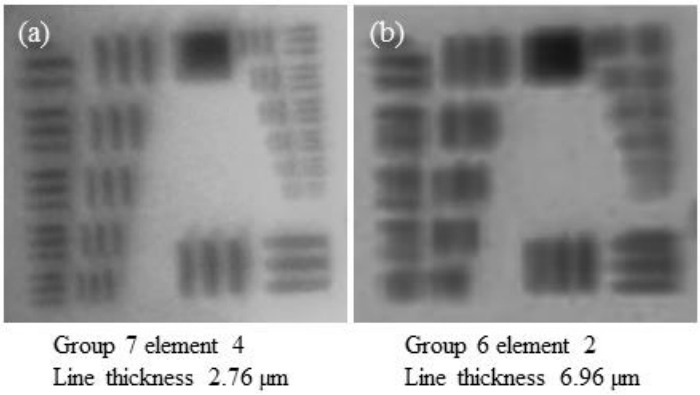

Fig. 4.15 Lateral resolutions with (a) axicon lens assisted and (b) conventional systems.

4.10.3 Comparison with ICA photographic imaging methods

The imaging capability of the axicon lens assisted gonioscopy is compared against other ICA photographic imaging methods. These methods include conventional indirect gonioscopy with

Latina 5 Bar SLT (Ocular Instruments, Bellevue, WA, USA), EyeCam™ (Clarity Medical Systems, Pleasanton, CA, USA), and the flexible ocular imaging probe discussed in Chapter 3. The image quality of these trans-corneal imaging methods is highly dependent on the optical quality of the cornea. The comparison is thus performed on clear and mildly cloudy *ex vivo* porcine samples across all imaging systems. Five clear and five mildly cloudy *ex vivo* porcine samples with anatomically open angles are used for this investigation. The representative results are shown in Table 4.2.

The following conclusions can be drawn from Table 4.2. The ICA structures are more distinct in samples with higher optical quality cornea regardless of the imaging systems. It is also noted that the axicon lens assisted gonioscopy imaging system is able to show better image clarity when imaging mildly cloudy eyes. Wide field imaging with EyeCam™ and the flexible ocular imaging probe enable a larger field of view. Direct and indirect gonioscopy typically image up to one quadrant of the eye. On the quality of images, it is evident that the axicon lens assisted gonioscopy imaging system has the highest resolution. It is able to image the ICA with high resolution. The TM, scleral spur (SS), pigmentation, ciliary body band (CBB), and iris are clearly visible. This is followed by the flexible ocular imaging probe, EyeCam™, and indirect gonioscopy with Latina 5 Bar SLT respectively.

Table 4.2 Comparison with ICA photographic imaging methods.

Imaging techniques	Clear cornea	Mildly cloudy cornea
(a) Clear and (b) mildly cloudy cornea.	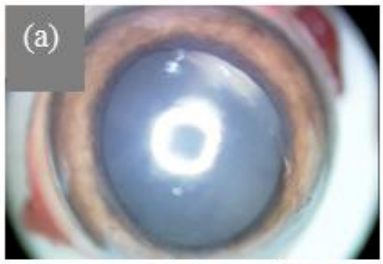	
Latina 5 Bar SLT gonioscopic images of (c) clear and (d) mildly cloudy cornea.	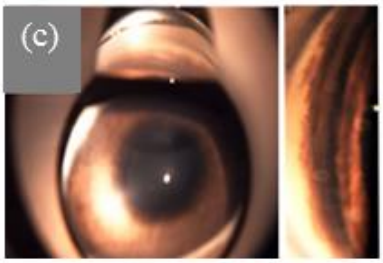	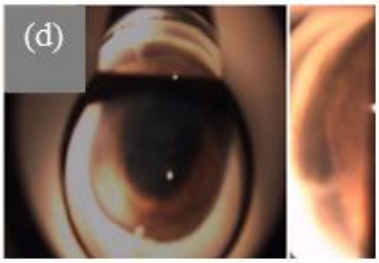
EyeCam™ images of (e) clear and (f) cloudy cornea.		
Flexible ocular imaging probe images of (g) clear and (h) mildly cloudy cornea.	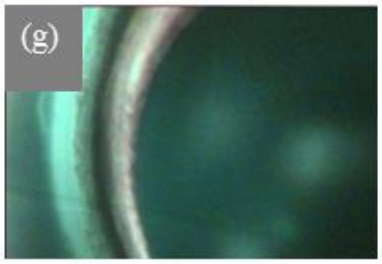	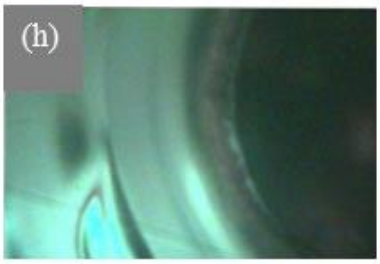
Axicon assisted gonioscopic images of (i) clear and (j) mildly cloudy cornea. The TM, pigmentation (Pi), ciliary body (CB), and iris are clearly visible.	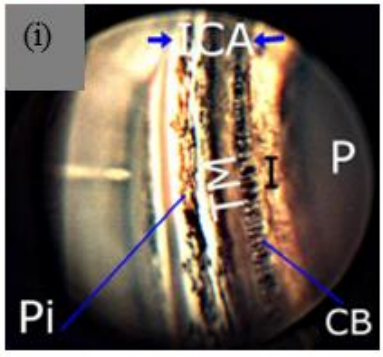	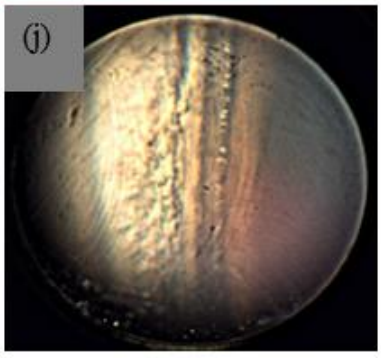

4.11 Summary

Ocular imaging technology that holds promise for both fundamental investigation and clinical detection of glaucoma is still a challenging research area. A direct view of the TM with high resolution is not generally possible because the ICA region is obstructed by the sclera overlap. The best approach to observe the AOS is therefore to view from the opposite angle.

A Gaussian illuminated static light sheet configuration and a digitally scanned Bessel-Gauss beam plane illumination configuration have been demonstrated for trans-corneal ICA imaging of the porcine eye. In addition to the advantages of static light sheet configuration, the digitally scanned Bessel-Gauss beam light sheet configuration is able to overcome the trade-off between the thickness and length of the Gaussian light sheet to give higher axial resolution, a greater depth of focus, and better signal-to-noise ratio. The digitally scanned Bessel-Gauss beam based light sheet imaging system has adequate spatial resolution to resolve the TM structures, thereby providing objective information about the AOS and critical anatomical structures inside the eye. In this research, the imaging is limited to two spatial dimensions. It is therefore necessary to digitally unite a stack of these images, in order to obtain an accurate and complete understanding in three dimensions (3D). For a 3D volumetric stack, the focused Bessel-Gauss beam has to be swept in the *x*-direction to project a light sheet at each *z*-plane. Since the virtual light sheet can be scanned through the sample for 3D imaging, the test sample can be kept at the same position throughout data acquisition. Most importantly, this also minimizes motion artifacts. It is also possible to measure the aqueous humour flow rate overtime with this instrument. Future research work will be focused in these directions. This non-contact and non-invasive imaging methodology demonstrates high repeatability and has excellent safety profile. It is envisaged that

this proposed methodology can be popular among clinicians and vision researchers in the evaluation and management of glaucoma.

With innovative optical engineering of the digitally-scanned Bessel-Gauss beam light sheet imaging system, the illumination arm can be configured for the high resolution imaging and characterization of cornea. The apparatus for the non-contact imaging of AOS and cornea is shown in Fig. 4.16. For corneal imaging, the 488 nm diode laser and F810FC-543 are replaced with a near infrared (NIR) diode laser and a compatible fiber collimator, respectively. Also, the plano-convex axicon lens and collimation lens are not used while performing this imaging modality. The pellicle beam splitter, tube lens, neutral density filter, and CCD camera form the essential components. The laser marking software can be used to create a virtual light sheet or raster scan for ICA or corneal imaging respectively. Details of the optical setup will be covered in Chapter 5. In addition, the system packaging is designed and fabricated using computer-aided design software, SolidWorks as shown in (Appendix I).

This chapter also demonstrated for the first time, an axicon lens assisted indirect gonioscopy imaging system that can image with a spatial resolution of 3 µm. The proposed concept and methodology is successfully validated through Zemax optical simulations, spatial resolution characterization tests with USAF1951 chart resolution test target, and experiments with *ex vivo* porcine samples. Its imaging capability is compared against other ICA photographic imaging methods. The results show significant improvement in the visualization capability at the ICA region, as compared to current clinical photographic imaging instruments.

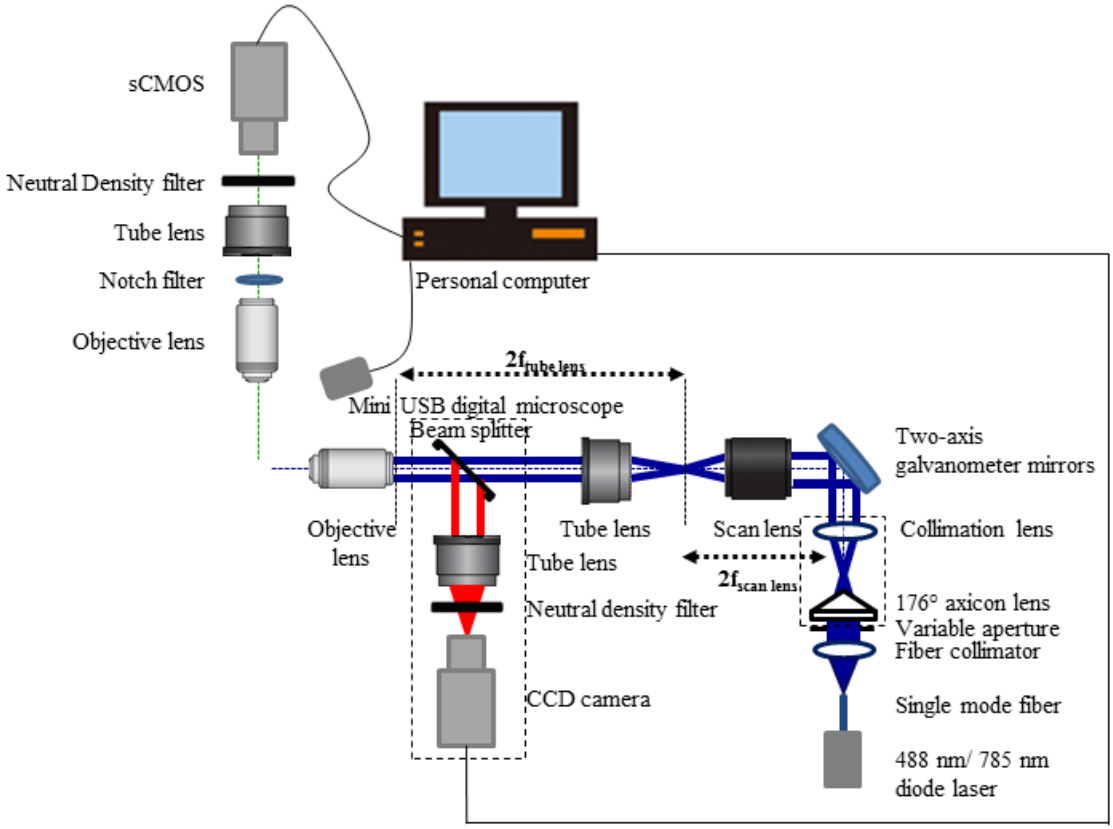

Fig. 4.16 Apparatus for the non-contact imaging of AOS and cornea.

Chapter 5: Non-contact optical imaging probes for evaluation of corneal diseases

This chapter demonstrates an optical method to examine and characterize the cornea. Two initial lab prototypes are developed based on near infrared (NIR) epi-illumination configuration. The proposed concepts and methodologies are validated through spatial resolution characterization tests with 1951 USAF resolution test target and experiments with ex vivo porcine samples. The probes possess high spatial resolutions and are non-dependent on coupling medium, which are significant for a clinician and patient friendly investigation. The clinical significance of the proposed study is validated by performing imaging of the New Zealand white rabbit's cornea infected with Pseudomonas.

5.1 Optical setup of imaging probe and imaging method

A schematic of the proposed configuration is shown in Fig. 5.1, while the photograph of the experimental setup is given in Fig. 5.1(b). The 785 nm diode laser (LBX-785, Oxxius, Wessling, Germany) is used as an illuminating source. The laser beam is coupled into an optical fiber, and the output is collimated using a fiber collimator (NA = 0.25, f = 36.01 mm) before reaching a 45:55 (R:T) pellicle beam splitter. The reflected beam from the beam splitter is used to illuminate the sample surface using a Mitutoyo infinity-corrected long working distance objective lens (Plan Apo, magnification = 20X, NA = 0.42, f = 10 mm, working distance = 20 mm). The images from the laser illuminated eye samples are collected through the same objective lens. An infinity-corrected tube lens (f = 200 mm, working distance = 148 mm) is used to refocus the image from the infinity-corrected objective lens onto the PixeLINK charged-coupled device (CCD) camera (Ottawa, Canada). A neutral density filter is placed between the

tube lens and the CCD camera in order to control the light intensity. The acquired images are digitally displayed on the computer screen. Depth-sensitive measurements are carried out by moving the objective lens gradually towards the eye at a constant lens speed of 60 μm/s, using a translation stage. The first image is captured when the first superficial cells are seen.

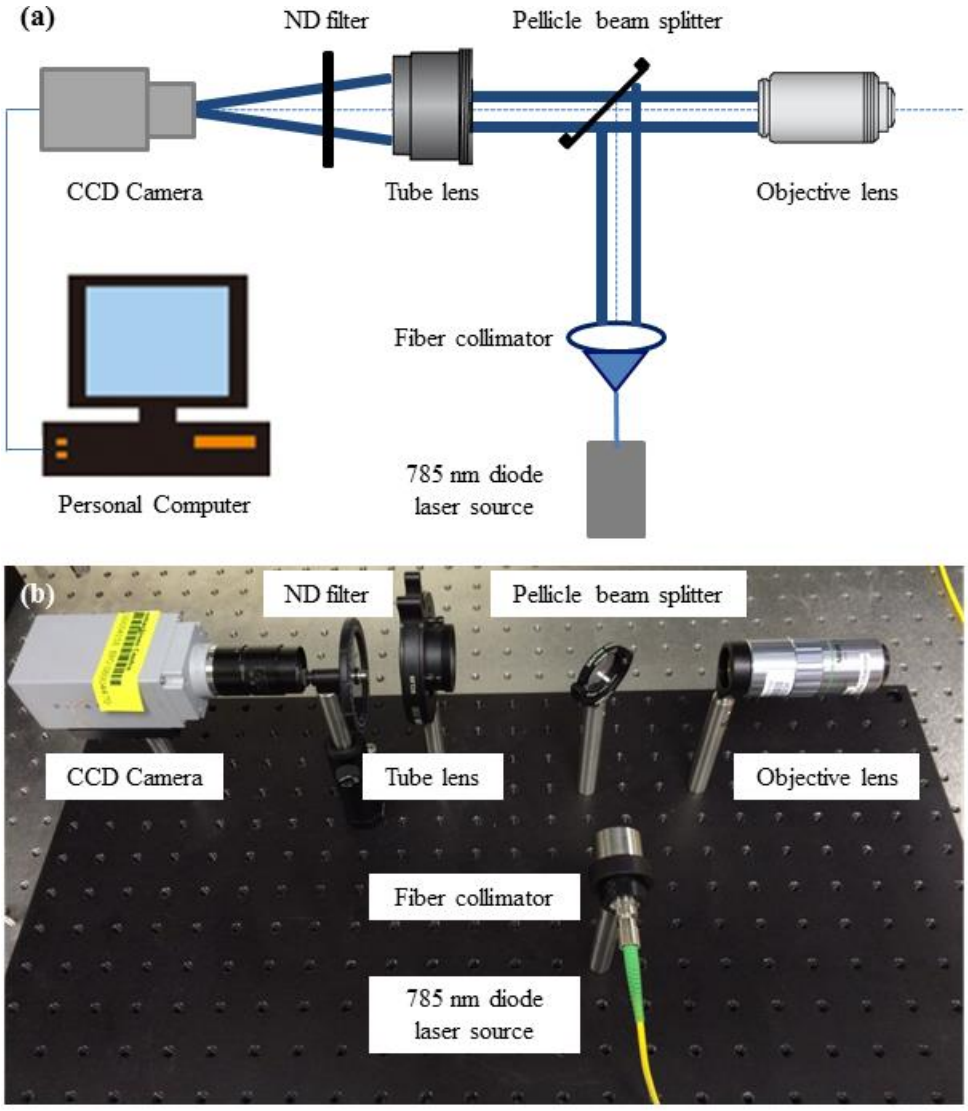

Fig. 5.1 (a) Schematic diagram and (b) photograph of proposed optical imaging probe.

It should be noted that the physical distance moved by the objective lens does not equate to the change in the focal plane through the cornea. This is because of the fact that cornea having

higher refractive index and introduces different (larger) optical path length (OPL) as per the formula, $OPL = nd$, where n is the refractive index of the cornea and d is the physical distance. This implies that for every 60 µm shift in the objective lens, the focal plane is shifted by a distance of 82.56 µm along the optical axis. At a constant lens speed of 60 µm/s, it takes approximately 12 s and 5 s, respectively, to cover the entire thickness of the porcine and rabbit corneas. The average thickness of the human cornea is approximately 500 µm [152], and it takes an estimated time of 6 s to scan from the epithelium to the endothelium layer. The imaging schematic is shown in Fig. 5.2.

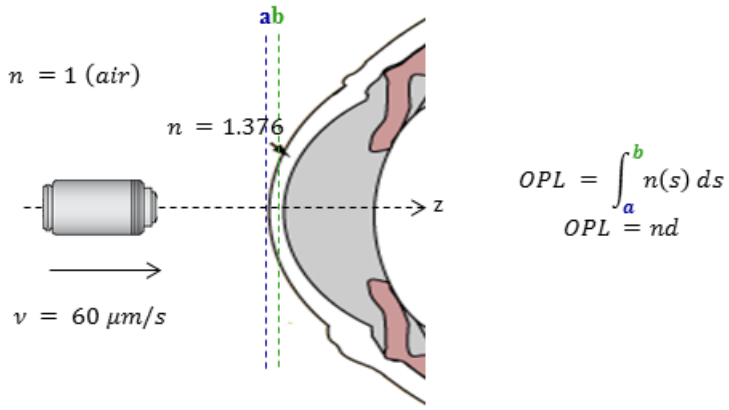

Fig. 5.2 Imaging schematic of the proposed probe.

5.2 Imaging with infinity optics assuming paraxial approximation

Infinity optics is employed in this proposed optical probe configuration to produce a parallel flux of light rays after passing through the objective. Unlike conventional microscope with fixed tube length, optical components placed in this "infinity space" neither introduce spherical aberration nor modify the objective's working distance. The parfocality of the system is also maintained with infinity optics. The distance between the infinity-corrected objective lens and tube lens is kept at 150 mm throughout the experiment, which is within the optimal distance of

70 mm to 170 mm. The image may suffer from aberrations or vignetting if the distance of separation is lesser than 70 mm or greater than 170 mm, respectively. Fig. 5.3 shows a Zemax simulation of two paraxial lenses in a 4F configuration, where the distance of separation is equal to the sum of the focal lengths.

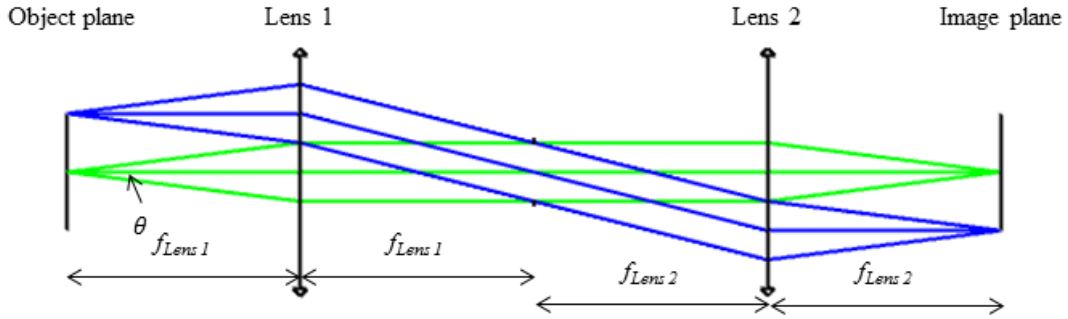

Fig. 5.3 Zemax simulation of two paraxial lenses in a 4F configuration.

Assuming paraxial approximation, the well-known expression for the diffraction limited spot size of a single lens system is given as [153]

$$d_{spot\ size} = 2.44(M + 1)\lambda \frac{f}{D_a}, \tag{5.1}$$

where $d_{spot\ size}$ is the diffraction limited spot size, M is the system magnification given by $\frac{s_i}{s_i}$ (s_i is the image distance and s_o is the object distance), λ is the wavelength, f is the focal length of the lens, and D_a is the aperture diameter. The function $\frac{f}{D_a}$ is also the *f*-number, $f^{\#}$. In an infinity-corrected system, s_o is also the focal length of the objective lens f_{OL}, and s_i is also the focal length of the tube lens f_{TL}. The magnification can therefore be written as a function of the focal lengths

$$M = \frac{s_i}{s_o} = \frac{f_{TL}}{f_{OL}}. \tag{5.2}$$

The diffraction limited spot size in an infinity-corrected system $d_{spot\ size}^{\infty}$ can be obtained by combining Eq. (5.2) with the well-known equation for the diameter of point spread function $d_{PSF} = \frac{2.44 s_i \lambda}{D_a}$. Therefore,

$$d_{spot\ size}^{\infty} = 2.44 M \lambda \frac{f_{OL}}{D_a} = 2.44 M \lambda f_{OL}^{\#}. \tag{5.3}$$

It is noted from Eq. (5.1) and Eq. (5.3) that the diffraction limited spot size of a single lens system and an infinity-corrected system are different, but can become very similar at large magnification. Since microscopic lenses are usually classified by their numerical aperture (NA) rather than $f^{\#}$, it is useful to express $d_{spot\ size}^{\infty}$ in terms of NA. From Fig. 5.3,

$$f_{OL}^{\#} = \frac{f_{OL}}{D_a} = \frac{s_i}{D_a} = \frac{1}{2 \tan\theta}. \tag{5.4}$$

Recall the trigonometry identity $\cot^2\theta + 1 = \csc^2\theta$ and simplifying,

$$\cot^2\theta + 1 = \csc^2\theta;$$

$$\cot^2\theta = \csc^2\theta - 1;$$

$$\frac{1}{\tan^2\theta} = \frac{1}{\sin^2\theta} - 1;$$

$$\tan^2\theta = \left(\frac{1}{\sin^2\theta} - 1\right)^{-1};$$

$$\tan\theta = \left(\frac{1}{\sin^2\theta} - 1\right)^{-\frac{1}{2}}. \tag{5.5}$$

Since $NA = n_0 \sin\theta$, where n_0 is the refractive index of the medium and θ is the half angle subtended by the objective lens, Eq. (5.4), Eq (5.5), and the expression of NA yields

$$f_{OL}^{\#} = \frac{1}{2\left(\frac{1}{\sin^2\theta} - 1\right)^{-\frac{1}{2}}} = \frac{1}{2}\left(\frac{1}{\sin^2\theta} - 1\right)^{\frac{1}{2}} = \frac{1}{2}(\sin^{-2}\theta - 1)^{\frac{1}{2}} = \frac{1}{2}\left[\left(\frac{n_0}{NA}\right)^2 - 1\right]^{\frac{1}{2}}. \tag{5.6}$$

Therefore, $d_{spot\ size}$ and $d_{spot\ size}^{\infty}$ expressed in terms of NA is given as

$$d_{spot\ size} = 1.22(M + 1)\frac{\lambda}{NA}, \tag{5.7}$$

and

$$d^{\infty}_{spot\ size} = 1.22M\lambda\frac{1}{2}\left[\left(\frac{n_0}{NA}\right)^2 - 1\right]^{\frac{1}{2}}. \tag{5.8}$$

5.3 Spatial resolution

The resolution of an imaging system is defined as the minimum distance of separation between two closely spaced points, such that they can be distinguished as two entities, rather than one. The effective resolution of the proposed system is similar to the conventional diffraction limit of wide field microscopy. It is bounded by three critical design characteristics and is given by $\frac{\lambda_{ex}}{2n(sin\theta)}$, where λ_{ex} is the excitation wavelength, n is the refractive index of the imaging medium, and θ is one-half of the angular aperture of the light cone captured by the objective. The term $n(sin\theta)$ is also known as the NA and it gives an indication to the light-gathering ability of the objective lens. The conventional diffraction limit of wide field microscopy can therefore be written as $\frac{\lambda_{ex}}{2NA_{det}}$, where NA_{det} is the numerical aperture of the detection objective. Experimentally, the spatial lateral resolution is determined by the imaging of the U.S. Air Force bar target (USAF1951 chart) [154]. The proposed configuration is able to image up to group 7, the highest spatial frequency on the USAF1951 chart. Fig. 5.4 shows the resolution achievable at group 7, element 6. This corresponds to a lateral resolution of about 2.19 μm in air and 1.59 μm in corneal tissue (n = 1.376) after calculations. No attempts were made to image test targets of higher spatial frequencies due to the limiting magnification and respective NA of the objective lens [155].

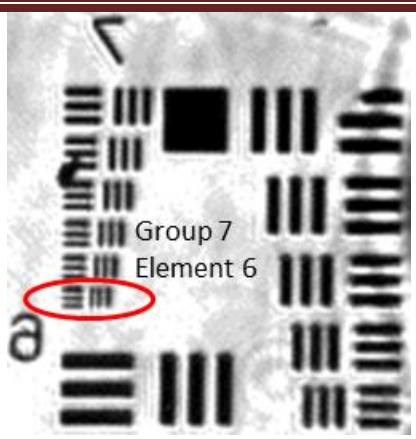

Fig. 5.4 Measurement of lateral resolution using USAF1951 chart.

5.4 Scale and region of interrogation

The scale and region of interrogation are determined using USAF1951 chart as shown in Fig. 5.5.

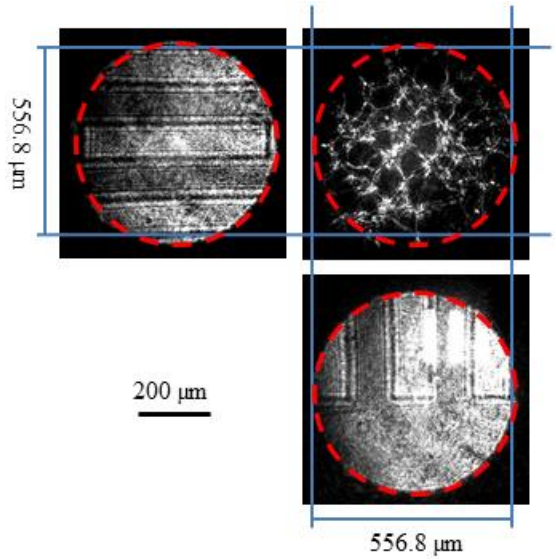

Fig. 5.5 Scale and region of interrogation determination using USAF1951 chart.

The horizontal and vertical bars of Group 2, element 2 are imaged. A 200 µm scale bar is derived and used for subsequent image acquisitions. The circular dashed lines in red indicate the

approximated region of interrogation with the 20X infinity-corrected long working distance objective lens.

5.5 Imaging with porcine samples and New Zealand white rabbit

Porcine eye is chosen as an *ex vivo* animal model in this study because of its similarity in morphology to that of the human eye. It has been used in vision sciences research involving but not limited to glaucoma and corneal transplant studies [122, 156]. The parameters of the porcine eyeball have been covered in a few studies, some of which provide information about the similarities and differences between porcine and human eyes [122, 157, 158]. Major differences between the porcine and human eye include the absence of the Bowman's layer in the porcine eye and the corneal thickness. Porcine corneal thickness is found to be twice that of human cornea.

The New Zealand white rabbit is used as an *in vivo* animal model because of the ease of manipulation and the similarity in corneal size with human [159]. Though keratometric readings and elevation values at the anterior and posterior are comparable to human, the corneal thickness and anterior chamber depth values are found to be lower than those in human [160]. Similar epithelium, stroma, and endothelium layers were identified in human and rabbit corneas, though the Bowman's and Descement layers were not as developed in rabbits [161, 162].

The most obvious advantage of using near infrared (NIR) illumination over white light is the possibility of examining eye parameters in its most natural and dynamic states, since there is no change in the eye anatomy with respect to lighting conditions. Compared to the longer wavelength that is employed in the various anterior segment optical coherence tomograohy (AS-OCT) systems, the proposed system has higher scattering in tissue and thus, a lower penetration

through scattering ocular structures such as the sclera and iris. In addition, retinal protection is decreased due to the lower absorption by water in ocular media [62, 163, 164]. High power illumination is therefore not desirable in the proposed system, and this sets a constraint to high-speed imaging, which eliminates motion artifacts and reduces examination time. The shorter wavelength of the proposed system however, promises a higher theoretical lateral reslolution, based on the conventional diffraction limit of wide field microscopy. The optical power of the system is kept within the maximum permissible exposure (MPE) limit recommended by the American National Standards Institute (ANSI) and other safety standards [116, 143, 165]. Subsequent confocal images of the rabbit also shows that the cells were not damaged due to exposure to laser light at this wavelength and power (see Appendix J).

The upright positioning of the sample and non-contact nature of the proposed system also allow viewing of the cornea in its natural and dynamic states. Operation of the proposed system does not require much expertise since there is no requirement for any sample preparation or coupling medium. Unlike the ultrasound biomicroscopy (UBM) or confocal system, application of this procedure does not expose the patient to risk of corneal abrasion and infections. This procedure is therefore suitable for pre- and post-operative eyes, and for patients with prior ocular injuries. Similar to the current OCTs, visualization of the sulcus is not possible because the posterior layer of the iris is not transparent for the infrared light. Also, the ciliary body will not be entirely visible, as the infrared light will be absorbed on its way through the sclera. The proposed system combines the non-contact feature of the OCTs, with the high spatial resolution of the confocal microscope. While the performance of the proposed system is limited in cases of corneal opacities or abnormalities, it is able to provide resolution up to the cellular level, and this

allows the characterization and identification of the infectious agent in the case of an inflammatory response. Subsequent treatment response can then be evaluated objectively and this contributes indirectly to the cost-effective factor.

A 45:55 (R:T) pellicle beam splitter is placed in the infinity space to reflect the collimated output from the fiber onto the sample surface via the long working distance infinity-corrected objective lens. The reflected image signal from the sample is collected by the same objective lens in this epi-illumination configuration, before passing through the tube lens onto the CCD camera. The CCD camera is highly sensitive, and can detect reflected signals that are several orders smaller than the incident optical power. The amount of optical backscatter changes with respect to the gradient of the refractive indices of the various structures in the cornea, whereby a large difference in the refractive indices corresponds to a larger reflectance and hence, a higher contrast [166]. Fig. 5.6 and 5.7 show the images of the porcine and rabbit cornea across its entire thickness, respectively, along with their cross-sectional images. The images are captured by moving the objective lens gradually towards the eye, hence moving the focal plane along the optical axis, towards the corneal stroma and endothelium. Even though the rabbit was under general anesthesia, its breathing motion caused slight movements between individual frame acquisitions, and this result in significant motion artifacts. The problem of motion artifacts were not as significant in the *ex vivo* porcine model since the eye samples were secured firmly on the custom mount.

It is evident from Fig. 5.6 and 5.7 that the images have become obscured at the endothelium due to light emanating from regions above and below the focal plane. Unlike the commercial laser confocal microscope system, this proposed system is unable to eliminate the out-of-focus

blurs and achieve the optical sectioning. Further processing of the two dimensional (2D) images is required in order to enhance image quality, followed by the development of software for the three dimensional (3D) reconstruction of the cornea across its entire thickness. These research directions will be explored in future.

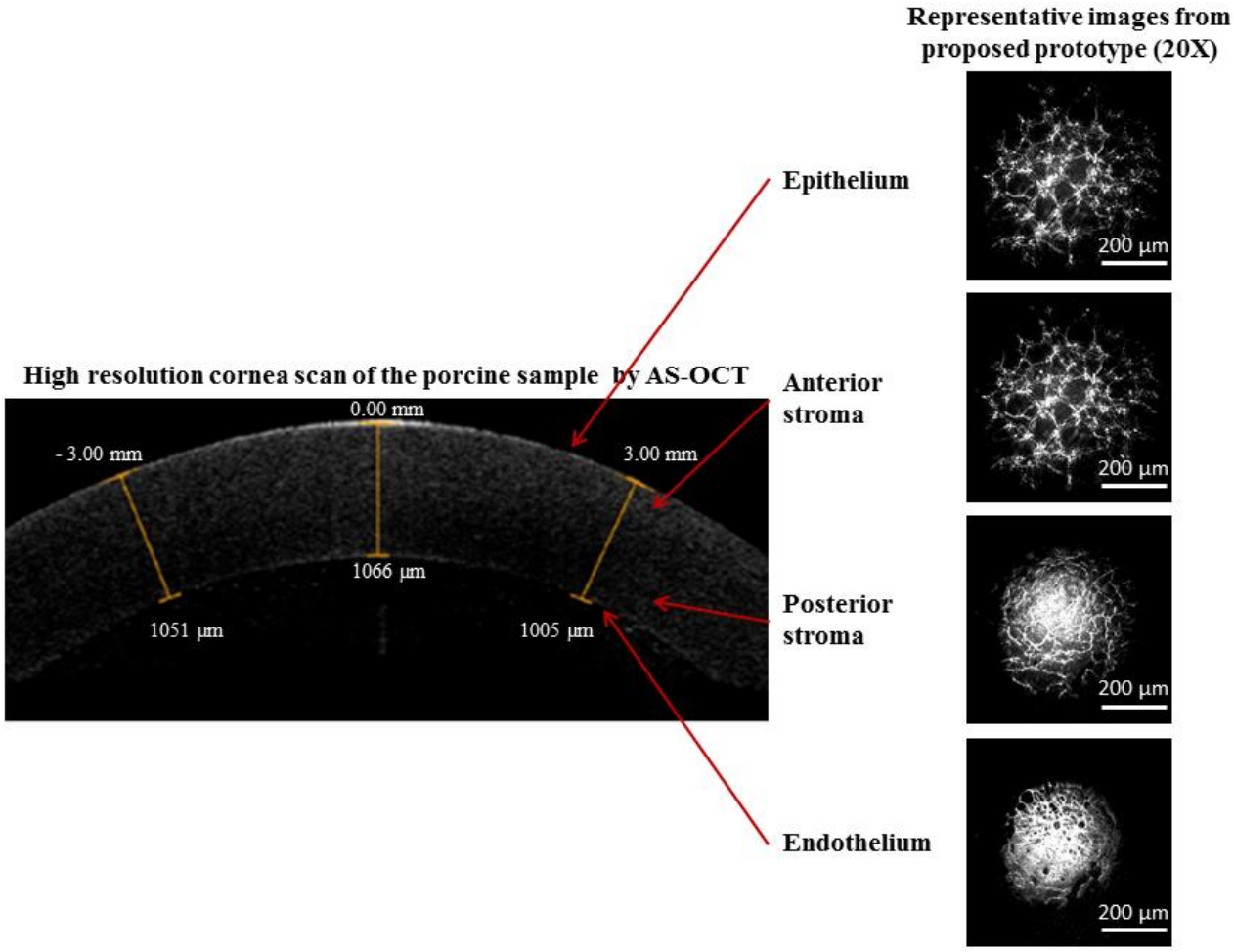

Fig. 5.6 Digital images of the porcine cornea at different depths and its OCT image.

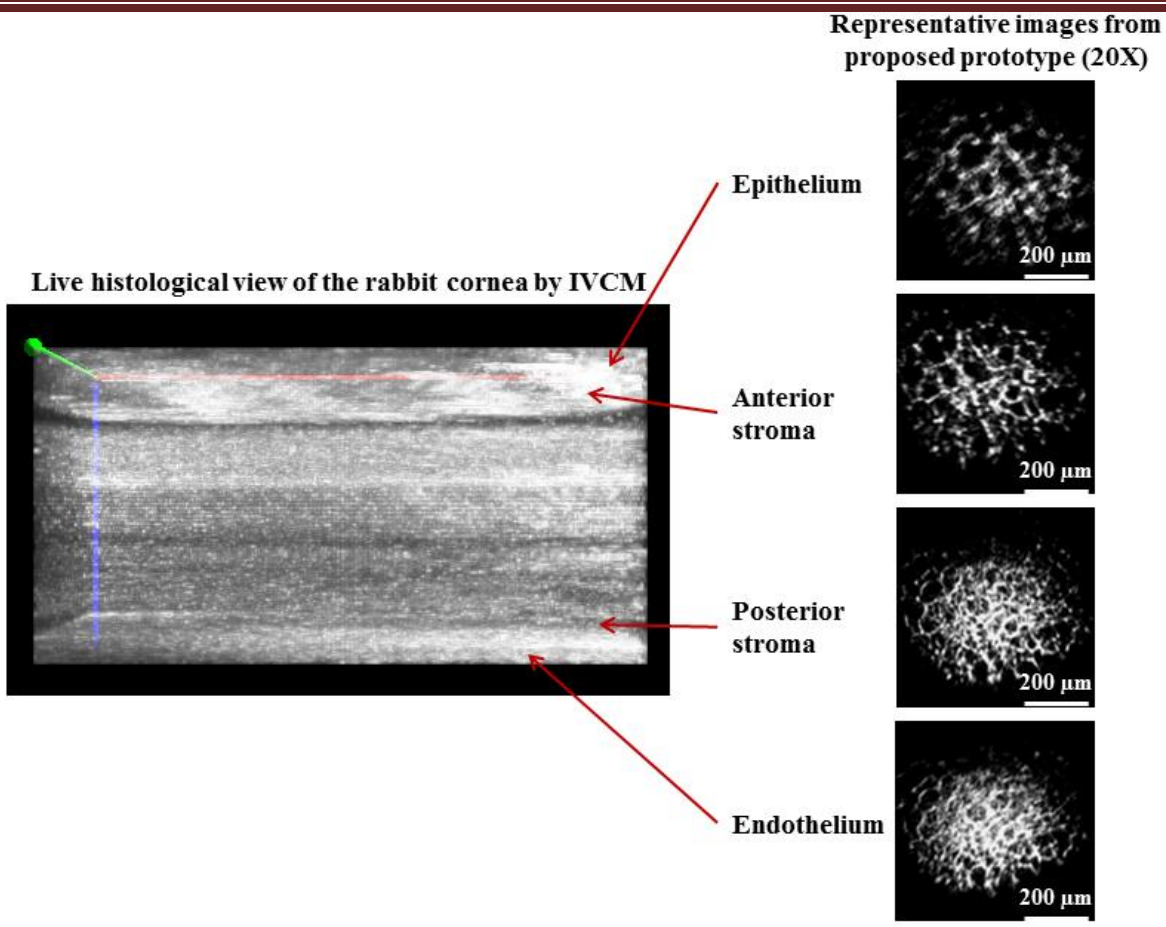

Fig. 5.7 Digital images of the rabbit cornea at different depths and its IVCM image.

Two sets of measurements were taken for each sample, and the procedure was repeated on forty different samples, with low variation in contrast. Though the proposed system demonstrates high repeatability, further studies are required to determine whether there are discrepancies with results obtained from other non-contact methodologies. An agreement suggests that the proposed system will complement existing imaging modalities in the assessment and evaluation of corneal diseases, so as to decrease morbidity and improve the effectiveness of subsequent treatment. Another limitation of the proposed system is that the 2D images cover only an area equivalent to the laser spot size. This means that multiple sections and hence, a longer image acquisition process is necessary in order to image the entire cornea. The average white to white cornea

diameter of a healthy adult is ~11 mm [167]. Assuming a laser spot size of ~0.4 mm, as least 28 laser spots are needed to scan across the diameter of the cornea. This problem can be easily overcome by introducing a galvanometer and scanning optics. A larger area then can be analyzed by sweeping the focused Gaussian beam in a raster fashion. This will be discussed further in section 5.7.

5.6 Imaging of the rabbit's cornea infected with *Pseudomonas*

The efficacy of the proposed system is further demonstrated by studying the rabbit's cornea infected with *Pseudomonas* as per the approved guidelines. The imaging of the infected eye was performed 10 days after the infection and the results are as shown in Fig. 5.8. *Pseudomonas* multiplies rapidly and crowd out the host tissues, hence disrupting the normal physiology of the eye. The more densely populated epithelium and higher reflectivity of Fig. 5.8(b) can be associated with hallmarks of bacteria keratitis such as loss of corneal transparency, peripheral epithelial edema, and deep stroma abscesses.

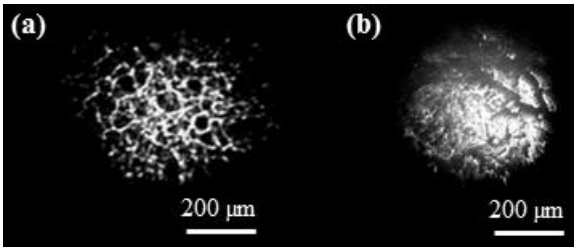

Fig. 5.8 Imaging of (a) a healthy cornea and (b) a cornea infected with *Pseudomonas*.

5.7 Integration of scanning optics

A schematic of the modified configuration with scanning optics is shown in Fig. 5.9.

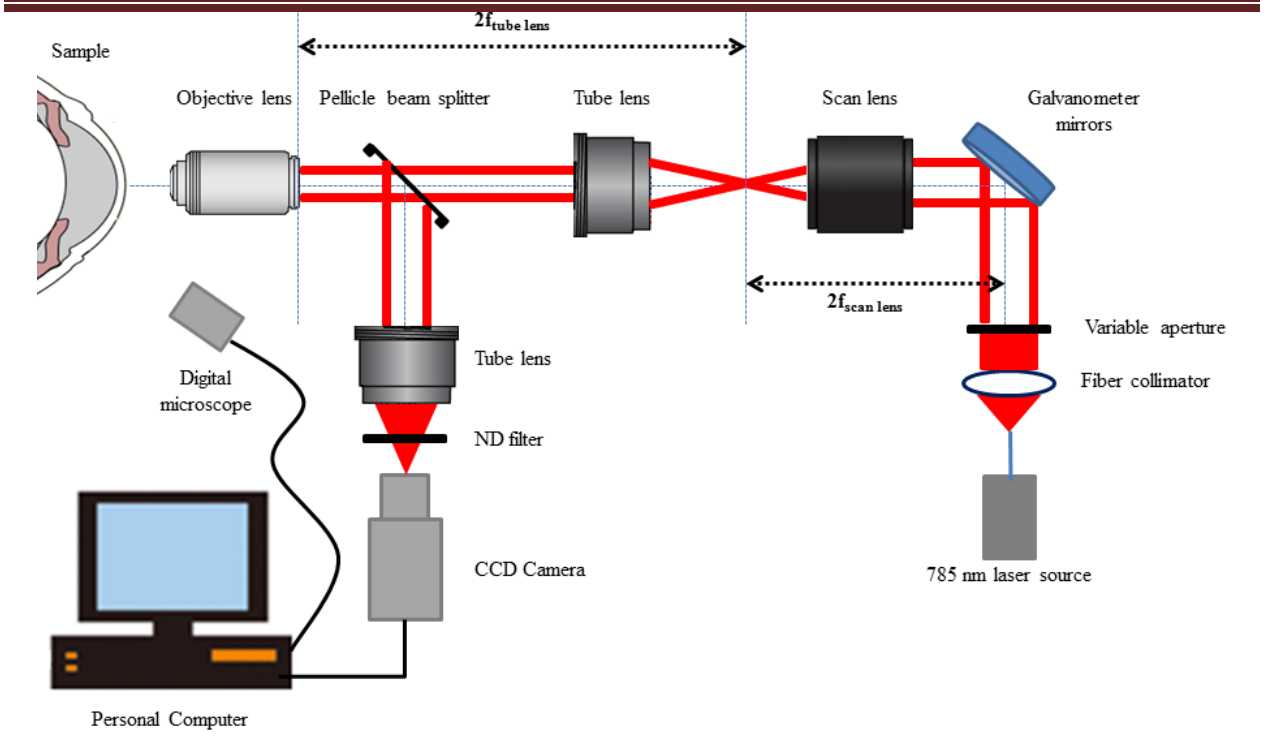

Fig. 5.9 Modified configuration with scanning optics.

The 785 nm diode laser (LBX-785, Oxxius, Wessling, Germany) is used an illuminating source. The laser beam is coupled into an optical fiber, and the output is collimated using a fiber collimator (NA = 0.25, f = 36.01 mm). The collimated Gaussian beam is incident onto the two-axis galvanometer mirror before passing through the scan lens (f = 70mm, working distance = 54 mm), infinity-corrected tube lens (f = 200 mm, working distance = 148 mm), and infinity-corrected long working distance objective lens (Plan Apo, magnification = 20X, NA = 0.42, f = 10 mm, working distance = 20 mm) configuration. In contrast to the orthogonal excitation and detection axes in Chapter 4, the corneal imaging scheme is based on an epi-illumination configuration. Images from the laser illuminated samples are collected through the same objective lens and then reflected by a 45:55 (R:T) pellicle beam splitter. The reflected images then pass through a second infinity-corrected tube lens and refocus onto the PixeLINK CCD

camera. A neutral density filter is placed between the tube lens and the CCD camera in order to control the light intensity. The acquired images are digitally displayed on the computer display monitor. The first image is captured when the first superficial cells are seen. Similarly, a small digital microscope is used to assess and document the alignment of eye with laser beam.

5.8 Scanning optics configuration

In this configuration, scanning optics and software-controlled galvanometer mirrors are incorporated to reduce the time required to image a desired region of interest (ROI). The tele-centricity of the scan lens results in a flat imaging plane that is desirable for laser scanning applications. It should be noted that in a point-by-point laser scanning system, the focal spot does not necessary coincides with the optical axis of the scan lens. In contrast to a conventional lens that will result in serious aberrations and poor image quality, the scan lens is designed to produce uniform spot size and OPL at every scan position. A uniform spot size over the entire FOV translates to high quality and uniform image. Geometrically correct images are produced and image distortion is minimized as the laser beam is scanned across the back aperture of the scan lens. The tube lens on the other hand, consists of two doublets that are corrected for lateral and axial aberration across the entire FOV. The scan lens and infinity-corrected tube lens are configured in a 4F arrangement. The scan lens is precisely aligned at eyepoint with the galvanometer mirrors, and the focal point coincides with field aperture plane. The galvanometer mirrors sweeps the focused Gaussian beam across the corneal surface in a raster fashion as shown in Fig. 5.10. The intensity profile of the beam, ROI, and scanning speed can be controlled using software.

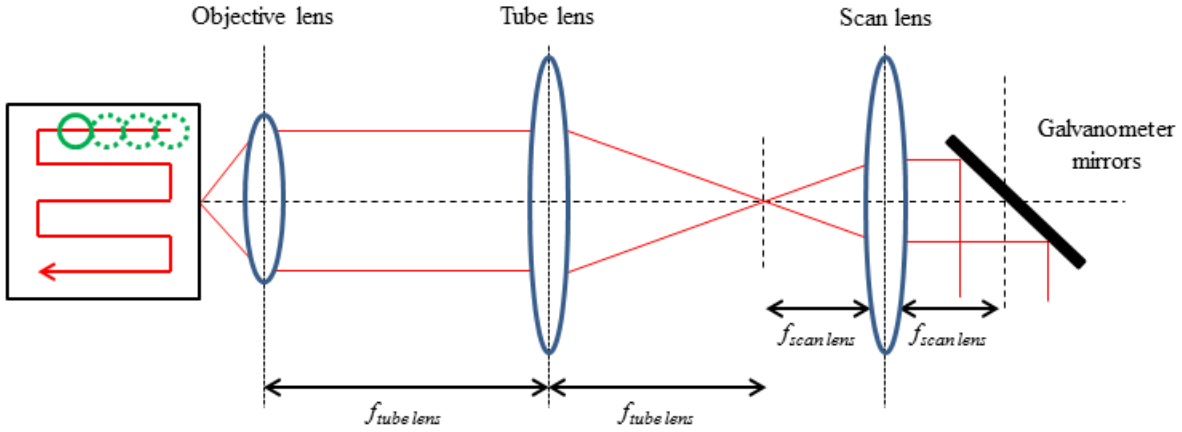

Fig. 5.10 Scanning optics configuration.

Since the working distance of an objective decreases as its magnification and NA increases, it can be understood that the working distance of an objective is limited by the need for a high NA and hence, a high resolving power. In this study, the efficiencies of two Mitutoyo infinity-corrected objective lenses were considered at the distal end of the optical probe configuration. The effective spatial lateral resolution of the proposed configuration can be determined experimentally by imaging the USAF1951 bar target chart. The system is capable of imaging up to group 7, element 6, with the 20X objective, and up to group 8, element 6, with the 50X objective (Plan Apo, magnification = 50X, NA = 0.55, f = 4 mm, working distance = 13 mm), as shown in Fig. 5.11. These correspond to estimated lateral resolutions of 2.19 µm and 1.10 µm respectively with air as an imaging medium, and 1.59 µm and 0.80 µm in the corneal tissue after calculations. While a higher magnification offers better lateral resolution, it comes at the expense of the ROI. This is because the FOV of the proposed configuration is limited by the inverse ratio of the objective magnification and the field number of the scan lens.

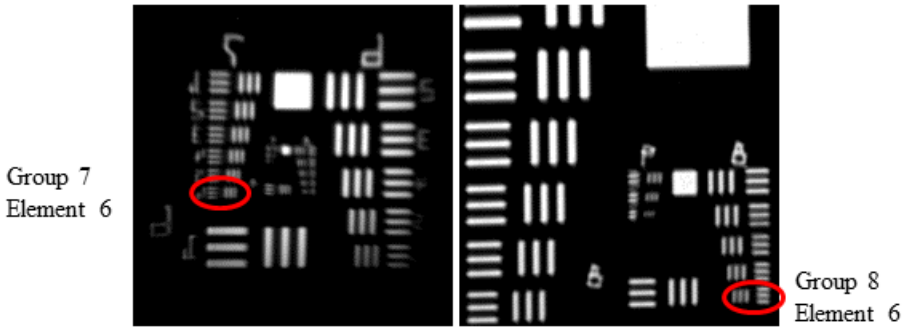

Fig. 5.11 Measurement of lateral resolutions with (a) 20X and (b) 50X objectives.

Fig. 5.12(a) shows a schematic representation of raster scanning across the ROI, while Fig. 5.12(b) shows a series of images acquired from *ex vivo* porcine sample. Fig. 5.12(c) shows a reconstructed image from the scan. The solid red lines in Fig. 5.12(a) represent the direction of scan whereas the solid green lines correspond to the image position relative to Fig. 5.12(b). Stitching of images from the ROI can reveal the corneal topography. However, direct superposition of images is not ideal because of background light and noise. One possible solution is to select the scanned images with minimal overlapping, and then merged them to get the final image.

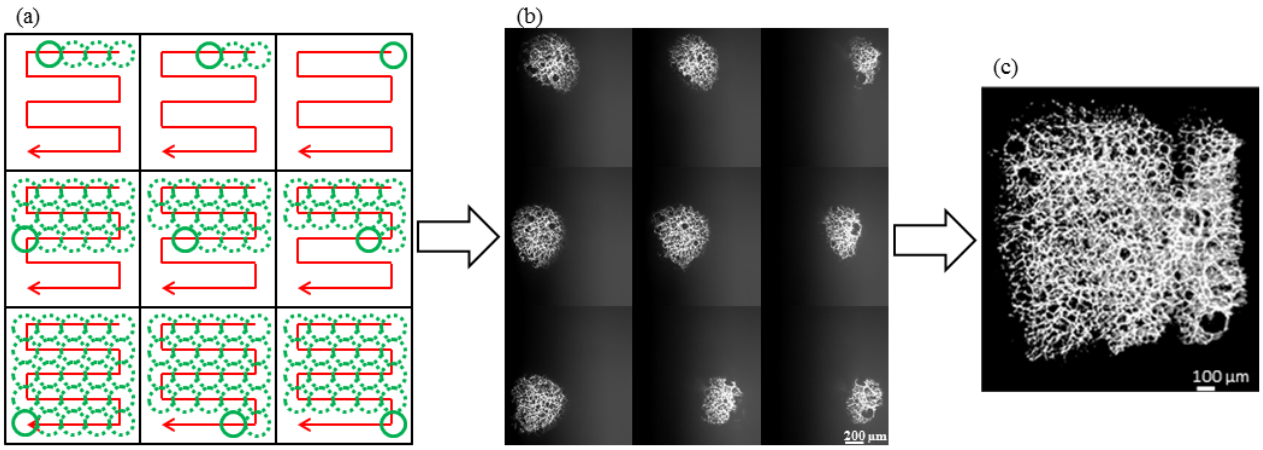

Fig. 5.12 (a) Schematic of raster scanning across the ROI, (b) series of images acquired, and (c) the reconstructed image.

5.9 Summary

An optical method to examine and characterize the different layers of the cornea is proposed and illustrated in this chapter. An initial lab prototype is developed based on a NIR epi-illumination configuration. The images acquired are believed to show the collagen fibrillary structures as well as the individual cellular structures at a higher resolution than current clinical devices. These images can be saved into computer database for further image processing and segmentation to allow clinicians to evaluate and capture the disease progression and treatment response overtime.

Corneal topography is achieved by incorporating scanning optics and software-controlled galvanometer mirror. The system exhibits a spatial lateral resolution of 1.59 μm and 0.80 μm, and a FOV of ~1.3 mm and ~0.5 mm, with the 20X and 50X long working distance objective lenses respectively. Image reconstruction can be realized using the proposed algorithm and related methodology. The results obtained are quite promising as detailed in the earlier sections. It is envisaged that this proposed prototype can in the long run enable accurate data analysis and diagnostic procedures of infections and inflammatory corneal diseases involving but not limited to viral, bacterial, or fungal keratitis.

Chapter 6: Conclusions and recommendations for future work

This chapter concludes this thesis. It highlights the major contributions and provides the guidelines and recommendations for future research work.

6.1 Conclusions

An ocular photographic imaging probe to record, capture, and display images of the iridocorneal angle (ICA) region and fundus is designed and fabricated. In this work, two variations of the probe are realized. The first variation consists of a 3 mm × 3 mm charged-coupled device (CCD) camera surrounded by a circular ring array of four white light emitting diodes (LEDs). The second variation is a 3 mm × 3 mm CCD camera surrounded by a circular ring array of two white light LEDs, one near infrared (NIR) LED with 940 nm peak emission wavelength, and an 808 nm NIR diode laser source. All the light sources have Lambertian radiation pattern. The complex non-rotational symmetric irradiance distribution of LEDs tilted at an angle is simplified using a geometrical model. Critical design parameters such as the LED viewing angle, working distance, illumination angle, and ring array radius were chosen after performing a theoretical investigation. The design parameters are as stated in Table 3.1. The imaging probes have field of view (FOV) of 140°, which is sufficient to image an entire quadrant of eye. The maximum achievable spatial lateral resolution at the ICA region and fundus are 10.08 lp/mm (~49.61 μm) and 5.04 lp/mm (~99.21 μm), respectively. At these resolutions, it is possible to delineate critical anatomical structures in the aqueous outflow system (AOS) such as the iris root (IR), ciliary body band (CBB), trabecular meshwork (TM) and scleral spur (SS), and the arteries, veins, and optic disc in the posterior segment. Experiments with validated animal

models of glaucoma such as porcine, New Zealand white rabbit, and cynomolgus monkey demonstrate high repeatability and reproducibility. Intra-observer reliability on assessments of primary angle closure is high since dark room provocation test can be used to elicit primary angle closure. In addition to its ability to objectively differentiate an open angle from a close angle, the imaging probes can also note pathological conditions such as appositional and synechial closure through contact lens assisted indentation imaging. This allows the proper classification and appropriate management. The imaging probes have a good safety profile, are easy to implement, reduce image acquisition time and patient discomfort as compared to conventional gonioscopic photography.

A Gaussian illuminated and a digitally scanned Bessel-Gauss beam light sheet fluorescence configurations to image the TM is conceptualized and developed. Optical ray tracing with Zemax software illustrates the ability of Bessel-Gauss beam to generate thinner light sheets with extended depth of field. The imaging systems generate two dimensional (2D) optical sections in large FOV, and at the same time reduce photobleaching and photodamage to the minimal. This is possible because the efficiency of the illumination source is maximized and irradiation is restricted to the plane under observation. The parallelization of image collection on the image sensor allows high image acquisition speed and hence further reduces photodamage. Both systems have an array size of 512 × 512, a rolling shutter mode and global (snapshot) shutter mode of 412 frames s^{-1} and 200 frames s^{-1}, and spatial lateral resolution of about 2.19 μm. The digitally scanned Bessel-Gauss light sheet is thinner than the depth of field of the detection objective, and this result in higher axial resolution. Unique property of the Bessel-Gauss beam to reconstruct increases the image contrast at the TM and minimizes the scattering and shadowing artifacts. Proof-of-concept studies were conducted with *ex vivo* porcine eye samples and New

Zealand white rabbit. An indirect axicon assisted gonioscopy imaging system is also conceptualized and developed in this chapter. Theoretical modelling and simulation were performed using Zemax software. As a proof of concept, the diagnostic bio-imaging capability of the proposed configuration was tested with enucleated porcine eye samples with anatomically open angles and compared against established medical photographic instruments and the flexible ocular imaging probe discussed in Chapter 3.

An optical method to examine and characterize the cornea is proposed and developed. An initial lab prototype for point imaging is developed based on the principle of reversibility of light. It consists of an NIR epi-illumination configuration with infinity optics in a 4F arrangement. Theoretical studies on conventional optics and infinity optics in 4F configuration were performed. Depth-sensitive measurements were performed by moving the objective lens gradually towards the eye, hence moving the focal plane along the optical axis, towards the corneal stroma and endothelium. The amount of optical backscatter changes with respect to the gradient of the refractive indices of the various structures in the cornea, whereby a large difference in the refractive indices corresponds to a larger reflectance and hence, a higher contrast. The optical setup was then modified to include scanning optics. Topography measurements were realized by sweeping the focused Gaussian beam across the corneal surface in a raster fashion. With a 20X objective, the imaging system has spatial lateral resolutions of 2.19 µm and a maximum FOV of ~1.3 mm. With a 50X objective, it has spatial lateral resolution of 1.10 µm and a maximum FOV of ~0.5 mm. Proof-of-concept studies were conducted with enucleated porcine eye and New Zealand white rabbit. The efficacy of the proposed system was further demonstrated by studying the rabbit's cornea infected with *Pseudomonas*. It is envisaged that this proposed prototype can in the long run enable accurate data analysis and diagnostic procedures of corneal diseases and post-surgical evaluation of wound healing responses.

A method and apparatus for the non-contact sequential imaging of cornea and AOS is proposed and demonstrated, based on a Gaussian beam epi-illumination configuration and a Bessel-Gauss beam plane illumination configuration, respectively. This apparatus is essentially a combination of Chapter 4 and Chapter 5. With innovative optical engineering of the Bessel-Gauss beam plane illumination configuration, the illumination arm of the light sheet configuration can be used for the high resolution imaging and characterization of cornea. For corneal imaging, the 488 nm diode laser and fiber collimator F810FC-543 are replaced with the 785 nm diode laser and fiber collimator F810FC-780, respectively. The 176° apex angle plano-convex axicon lens and collimation lens are removed while the pellicle beam splitter, tube lens, neutral density filter, and CCD camera are added. The laser marking software can be used to create a raster scan or virtual light sheet for corneal or ICA imaging respectively. The imaging capabilities of this apparatus are the same as those stated in Chapter 4 and Chapter 5. More translational and clinical investigations are necessary, in order to determine whether the proposed system will complement existing imaging modalities in clinical settings. Comparative studies with other established methodologies can improve the effectiveness of subsequent treatments and decrease morbidity. It is envisaged that this proposed methodology can be popular among clinicians and vision researchers in the evaluation and management of corneal diseases and glaucoma in the near future.

6.2 Major contributions

The major contributions of this thesis are as follows:

(i) Design and fabrication of flexible ocular imaging probes with specifications to record, capture, and display ICA images and posterior segment images. The handheld imaging

probes consists of a 3 mm × 3 mm CCD camera, surrounded by a circular ring array of white/ NIR LED light sources and NIR laser source. The strategy to optimize critical design parameters such as LED viewing angle, working distance, illumination angle, and ring array radius are discussed. The imaging probes have resolutions of 10.08 lp/mm (~49.61 μm) at the ICA region and 5.04 lp/mm (~99.21 μm) at the fundus. Critical anatomical structures can be identified, and the flexible ocular imaging probes can objectively differentiate an open angle from a closed angle and note pathological conditions.

(ii) Static Gaussian and digitally scanned Bessel-Gauss beam plane illumination configurations to image TM are conceptualized and verified experimentally. Digitally scanned light sheet offers more efficient and convenient method to adjust the height and intensity of the light sheet whereas Bessel-Gauss beam has a thin and long focus to overcome the trade-off between the length and thickness of a Gaussian light sheet. This is the first application of SPIM in ocular imaging. The system has spatial lateral resolution of 3 μm, an array size of 512 × 512, a rolling shutter mode and global (snapshot) shutter mode of 412 frames s^{-1} and 200 frames s^{-1} respectively, high speed of image acquisition, intrinsic optical sectioning capabilities, and low photobleaching and photodamage.

(iii) Conceptualization, development and demonstration of an indirect axicon assisted gonioscopy imaging system. This is achieved by integrating the concept of Bessel beam microscopy with conventional gonioscopy imaging. Theoretical modelling and simulation studies were performed to investigate the efficacy of the imaging system. This is followed by experimental validation with enucleated porcine eyes. This instrument has

spatial lateral resolution of 3 μm. It can resolve the TM structures and even quantify the pigmentation.

(iv) Concepts and methodologies for the simple, non-contact examination and characterization of cornea are proposed and demonstrated based on the principle of reversibility of light. Point imaging and scanning assisted configurations are developed for depth and topography measurements respectively. The amount of optical backscatter changes with respect to the gradient of the refractive indices of the various structures in the cornea, whereby a large difference in the refractive indices corresponds to a larger reflectance and hence, a higher contrast. Corneal topography is achieved by incorporating scanning optics and software-controlled galvanometer mirror. At 20X magnification, the systems have spatial resolution of 2.19 μm and a maximum FOV of ~1.3 mm. At 50X magnification, the systems have spatial resolution of 1.10 μm and a maximum FOV of ~0.5 mm.

(v) A method and apparatus for the non-contact sequential imaging of cornea and AOS is proposed and demonstrated. This integrated platform is based on a Gaussian beam epi-illumination configuration and a Bessel-Gauss beam plane illumination configuration, respectively. Illumination arm of the SPIM can be modified to perform corneal imaging. The laser marking software can create a raster scan for corneal topography or a virtual light sheet for ICA imaging. The imaging capabilities of this apparatus are as stated above. This imaging system is expected to find potential applications in the evaluation and diagnosis of glaucoma and corneal related diseases.

6.3 Recommendations for future work

This thesis sets the foundation for multiple study opportunities. The recommendations for future work are listed below.

- The aim of the flexible ocular imaging probe is to provide an alternative to gonioscopic photography that has a better safety profile, is easier to implement, and reduces image acquisition time and patient discomfort. The flexible ocular imaging probe in Chapter 3 was optimized by fixing two variables – the viewing angle of LEDs, and the working distance of imaging probe. LEDs of 20° viewing angles were selected while the working distance was set at 10 mm, considering the distance from the limbal of eye to the opposite ICA region. Though images of reasonable quality were obtained for fundus imaging, it should be noted that the circular ring array of LEDs was not optimized for fundus imaging. The approximate distance from the anterior cornea to the fundus is 20 mm. One solution is to employ a pair of two linear LED arrays at 0° illumination for future prototype. In this case, the irradiance E is given by the sum of the irradiances of the individual LEDs, and s is the distance between the two LEDs, where

$$E(x,y,l) = l^m A_{LED} L_{LED} \left\{ \left[\left(x - \frac{s}{2}\right)^2 + y^2 + l^2 \right]^{-\frac{(m+2)}{2}} + \left[\left(x + \frac{s}{2}\right)^2 + y^2 + l^2 \right]^{-\frac{(m+2)}{2}} \right\}. \quad (6.1)$$

  The concept discussed in Section 3.3 can also be applied here to achieve uniform irradiance distribution for linear LED array. The aim is to optimize the separation distance, s, such that the irradiance slope variation is minimal, and the implicit second-order term of Eq. (6.1)

disappears. In order to achieve the maximally flat condition for s, E is partially differentiated twice with respect to x, and set $\frac{\partial^2 E}{\partial x^2} = 0$ at $x = 0$ and $y = 0$. Therefore,

$$s_0 = \sqrt{\frac{4}{m+3}}\, l. \tag{6.2}$$

The detailed derivation can be found in Appendix K. A possible configuration based on Eq. (6.2) is shown in Fig. 6.1.

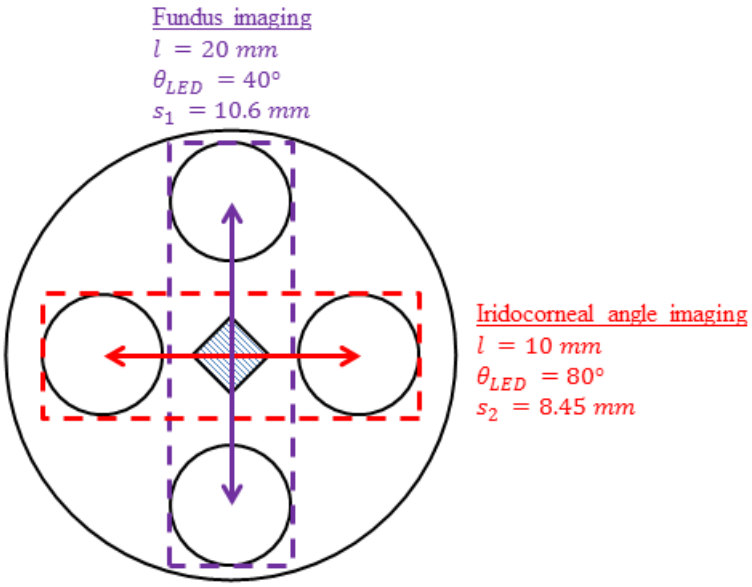

Fig. 6.1 A pair of two linear LED arrays at 0° illumination.

Design Eq. (6.2), when coupled with optical design and analysis program such as TracePro, can be useful for a quick estimation to optimize LED arrays for uniform near field irradiance. An image detector with higher sensitivity in the NIR region can also be considered in the next prototype. It is also possible to extend its application to the surgical management and follow-up procedures of micro-invasive glaucoma surgeries and goniosynechiolysis. Discussions with clinicians regarding miniaturization of the imaging probe and clinical studies are underway.

- The Bessel-Gauss beam plane illumination configuration is a desktop lab prototype that uses bulk optics and only allows the viewing of up to a quadrant of the eye. For a full 360° view, the eye sample has to be rotated, which is impractical in clinical ophthalmology. In this context, a hand-held probe would offer the convenience of evaluating angle parameters from all quadrants. Customized fibers with a Gradient-index (GRIN) lens and an axicon at the distal end can be used to generate a Bessel-Gauss beam. A schematic of the proposed illumination arm with customized fibers is shown in Fig. 6.2. Optical fibers are ideal choice for miniaturization and wave guide since the optical paths realized by optical fibers provide flexibility and compactness, as well as excellent signal quality. In addition, the current lab prototype uses a 488 nm laser for illumination and fluorescence excitation. It should be noted that during the imaging of live subjects, the laser illumination will result in constriction of pupil, hence causing slight changes in the angle anatomy. NIR contrast agent that is compatible for ocular imaging such as indocyanine green will enable the imaging of ICA region in the most natural and dynamic state.

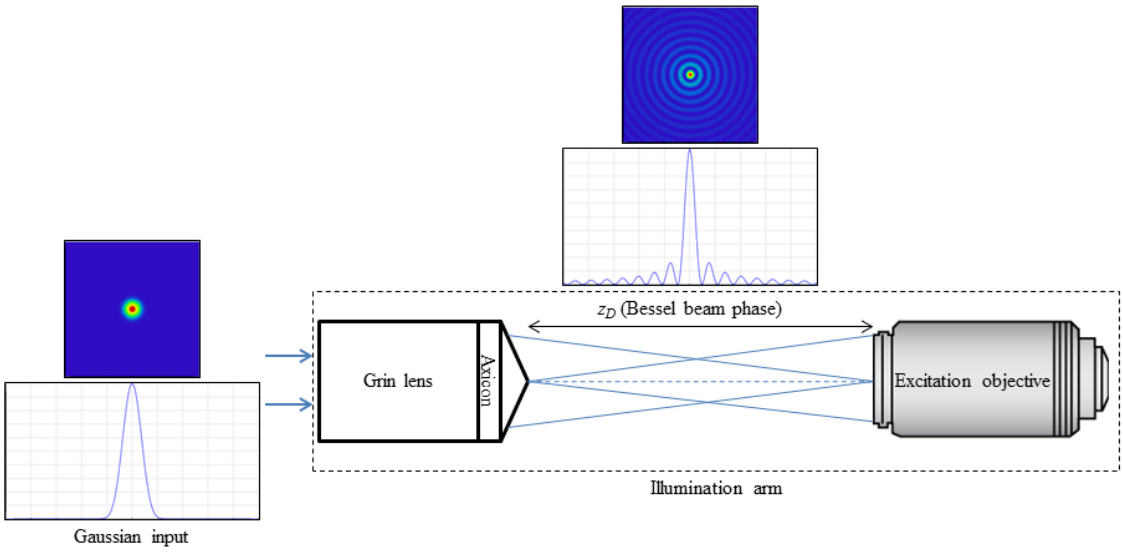

Fig. 6.2 Schematic of the proposed illumination arm with customized fibers.

- TM imaging with Bessel-Gauss beam plane illumination is limited to two spatial dimensions. It is necessary to digitally unite a stack of these 2D optical sections in order to obtain an accurate and complete understanding of the AOS in three dimensions (3D). Image processing algorithms that can accurately stack and register the optical slices, provide filtering and binning function, perform segmentation etc. can be of great value to clinicians and vision researchers. Similarly for corneal imaging, further processing of the 2D images is required in order to enhance image quality, followed by the development of software for the 3D reconstruction of across its entire thickness.
- The indirect axicon assisted gonioscopy imaging system aims at enhancing resolution of TM structures as well as the assessment and evaluation of TM pigmentation. Pigment quantification is critical in many protocols and grading techniques for glaucoma [168-170]. The level of pigmentation varies among individuals, and may change overtime due to exfoliation syndrome, pigment dispersion syndrome, surgery, or trauma. In exfoliation syndrome and pigment dispersion syndrome for example, the exfoliative material and excessive iris pigment settle into the TM and disrupt the aqueous outflow through the drainage canal. Accurate documentation of findings allows the proper classification and appropriate management. Nonetheless, there are only a few relevant studies which statistically analyzed the amount of TM pigmentation [171-173]. Initial pigmentation quantification studies were conducted with *ex vivo* porcine samples. The results are shown in Appendix L. This research thesis focuses mainly on hardware conceptualization and development for high resolution imaging. It should be fairly noted that development and advancement in computational toolkit for data analysis and image processing methodology is

as significant. For example, algorithms that can accurately measure the average amount of pigmentation in a targeted region of interest (ROI) divided by the ROI itself, can negate the influence of the size and shape of the selected ROI. This, followed by statistical analysis of data, can allow more accurate grading standards for glaucoma and hence allowing qualitative and quantitative analysis of TM structures. Hardware innovation when coupled with software novelty can enable predictive and objective evaluation of the AOS.

- Specialty beam profiles such as optical Bottle beam [174] can be used to generate thinner light sheets to further enhance axial resolution. Unlike Bessel beam, optical Bottle beam has on-axis intensity minima and is surrounded by regions of higher intensity. It can be generated by the interference or superposition of two or more Bessel beams with different radial or longitudinal propagation constants. Ahluwalia *et.al.* have demonstrated self-imaging optical bottle beams with a narrower diameter of the central core of a diffractive pattern [174].

It is envisaged that the major findings and original contributions of this thesis can contribute well towards the diagnostic bio-imaging applications of glaucoma and corneal diseases. Future work directions include translational and clinical investigations such as chairside validation with human patients and the statistical analysis of data. These will allow clinicians and vision researchers to understand the effectiveness of the developed systems. Comparative studies with established methodologies can improve the effectiveness of subsequent treatments, decrease morbidity, and complement existing imaging modalities in clinical settings. Initial comparative studies have been conducted and they can be found in Table 3.3, 4.1, and 4.2.

Appendices

Appendix A: Parameters of the anterior segment

One important parameter for measurement of angle anatomy is angle opening distance (AOD) [175]. It is defined as the perpendicular distance drawn from the trabecular meshwork (TM) anterior of scleral spur (SS) to the anterior iris surface. The AOD is measured at 500 µm and 750 µm. The shorter distance corresponds to the theoretical location of TM from SS, while the larger distance measures a more extensive region from SS that is less influenced by irregularities of iris surface.

Angle recess area (ARA) [176] is a triangular area that is bounded by the angle recess at the apex, with AOD 500/ 750 as the base, and inner-cornealscleral wall and iris surface at the sides. This parameter takes into consideration the entire contour of iris surface, unlike AOD which only measures at a single point on iris. Measurement of ARA is limited due to the poor visualization of angle recess at SS, which anatomically represents the junction between sclera and inner wall of TM. SS is a critical landmark in the calculation of angle parameters. It is the connecting point between the curvature of sclera and posterior curvature of cornea. TM and Schwalbe's line (SL) are located anterior to SS, whereas ciliary body and iris root are posterior to SS.

Trabecular-iris space area (TISA) [164] is a more accurate indicator of the actual filtering area as compared to ARA. Its calculation does not require clear visualization of angle recess and excludes the non-filtering area that is behind SS. It is a trapezoidal area that is bounded by AOD, iris surface, inner-cornealscleral wall, and inner scleral wall. An anatomically closed angle can be indicated by another parameter known as trabecular-iris contact length (TICL) [164]. It is

defined as the linear distance from SS to the last common point of corneal endothelium and iris towards the vertex. TICL is zero if there is no angle closure, since no common points will exist.

Despite the fact that anterior chamber angle (ACA) is a classic parameter in the assessment of anterior chamber, it is a subjective assessment compared to AOD and TISA, which are measured from anatomical landmarks. ACA is defined by three points, with the angle rays beginning at the AOD endpoints. The rays are extrapolated back toward the angle to form the apex of the triangle. Fig. A1 shows an illustration of the AOD, ARA, TISA, scleral spur angle, and ACA.

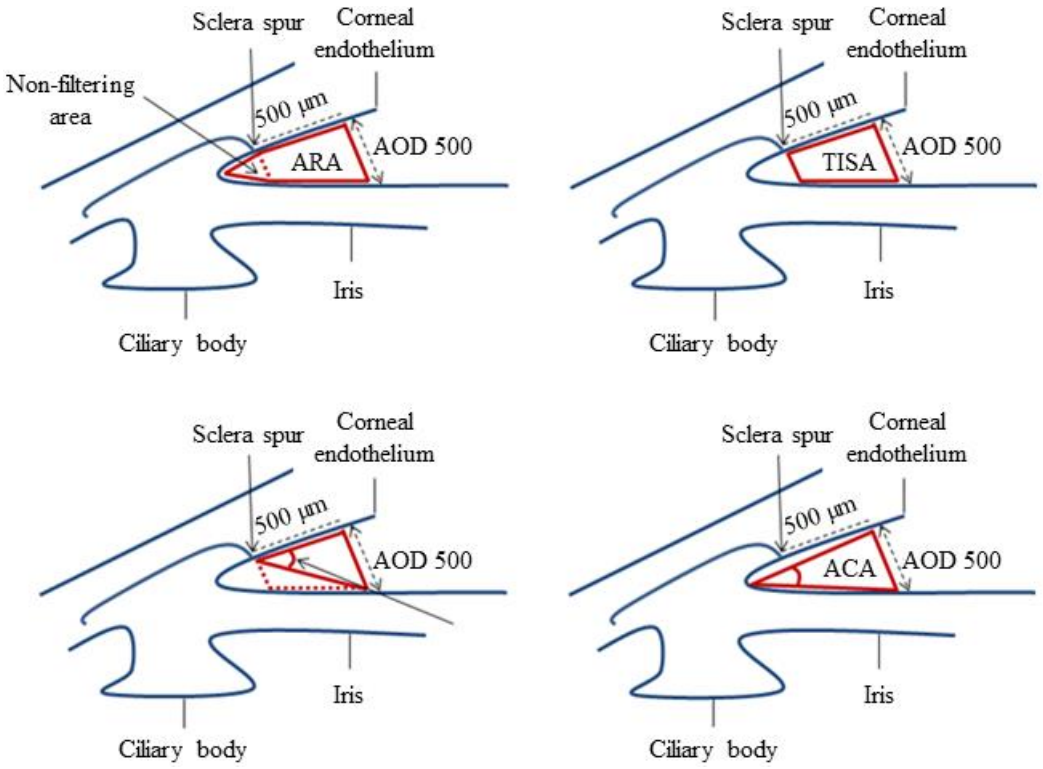

Fig. A1 Illustration of AOD, ARA, TISA, scleral spur angle and ACA.

Other parameters of the anterior segment include central corneal thickness (CCT), anterior chamber depth (ACD), angle to angle distance (ATA), and crystalline lens rise (CLR). CCT measures the entire corneal thickness from epithelium layer to endothelium. ACD is defined as

the distance from the corneal endothelium to anterior lens surface. CLR is the distance between the ATA bisector and anterior lens surface. It can be positive or negative depending on whether the lens protrudes forward or behind the bisector.

Appendix B: MATLAB® script for Snell's law

With respect to Fig. 3.1 and Eq. (3.3), real and imaginary values of the angle of refraction, θ_4, are plotted as a function of the incident angle, θ_1, and refractive index of medium outside the eye, n_3, using MATLAB®.

For real values of θ_4

```
% Setting the values of refractive indices and angles
n1 = 1.336;
n3 = 1;
theta_1 = [40:1:90];

% Working out the angle of refraction in air (Theta_4) using Eq. (3.3)
theta_4 = asind((n1/n3)*(sind(theta_1)));

% Plot graph of Theta_4 against Theta_1
plot(theta_1,theta_4);
hold on;

% Plot Theta_4 against Theta_1 for values of n3 from 1 to 1.4
% For n3 = 1.05
n3 = 1.05;
theta_4 = asind((n1/n3)*(sind(theta_1)));

% For n3 = 1.1
n3 = 1.1;
theta_4 = asind((n1/n3)*(sind(theta_1)));
plot(theta_1,theta_4);

% For n3 = 1.15
n3 = 1.15;
theta_4 = asind((n1/n3)*(sind(theta_1)));
plot(theta_1,theta_4);

% For n3 = 1.2
n3 = 1.2;
theta_4 = asind((n1/n3)*(sind(theta_1)));
plot(theta_1,theta_4);
```

```
% For n3 = 1.25
n3 = 1.25;
theta_4 = asind((n1/n3)*(sind(theta_1)));
plot(theta_1,theta_4);

% For n3 = 1.3
n3 = 1.3;
theta_4 = asind((n1/n3)*(sind(theta_1)));
plot(theta_1,theta_4);

% For n3 = 1.35
n3 = 1.35;
theta_4 = asind((n1/n3)*(sind(theta_1)));
plot(theta_1,theta_4);

% For n3 = 1.4
n3 = 1.4;
theta_4 = asind((n1/n3)*(sind(theta_1)));
plot(theta_1,theta_4);
```

For imaginary values of θ_4

```
% Setting the values of the refractive indices and angles
n1 = 1.336;
n3 = 1;
theta_1 = [40:1:90];

% Working out the angle of refraction in air (Theta_4) using Eq. (3.3)
theta_4 = asind((n1/n3)*(sind(theta_1)));

% Plot graph of Theta_4 against Theta_1
plot(theta_1,imag(theta_4));
hold on

% Plot Theta_4 against Theta_1 for values of n3 from 1 to 1.4
% For n3 = 1.05
n3 = 1.05;
theta_4 = asind((n1/n3)*(sind(theta_1)));
plot(theta_1,imag(theta_4));

% For n3 = 1.1
n3 = 1.1;
theta_4 = asind((n1/n3)*(sind(theta_1)));
plot(theta_1,imag(theta_4));
```

```
% For n3 = 1.15
n3 = 1.15;
theta_4 = asind((n1/n3)*(sind(theta_1)));
plot(theta_1,imag(theta_4));

% For n3 = 1.2
n3 = 1.2;
theta_4 = asind((n1/n3)*(sind(theta_1)));
plot(theta_1,imag(theta_4));

% For n3 = 1.25
n3 = 1.25;
theta_4 = asind((n1/n3)*(sind(theta_1)));
plot(theta_1,imag(theta_4));

% For n3 = 1.3
n3 = 1.3;
theta_4 = asind((n1/n3)*(sind(theta_1)));
plot(theta_1,imag(theta_4));

% For n3 = 1.35
n3 = 1.35;
theta_4 = asind((n1/n3)*(sind(theta_1)));
plot(theta_1,imag(theta_4));

% For n3 = 1.4
n3 = 1.4;
theta_4 = asind((n1/n3)*(sind(theta_1)));
plot(theta_1,imag(theta_4));
```

Appendix C: Specifications of LM520A

High luminous white light emitting diodes (LEDs) (LM520A, Seoul Semiconductor Co., Ltd) are used in Chapter 3. The physical dimensions, radiation diagram, spectral characteristics and photograph of LM520A are shown in Fig. C.1.

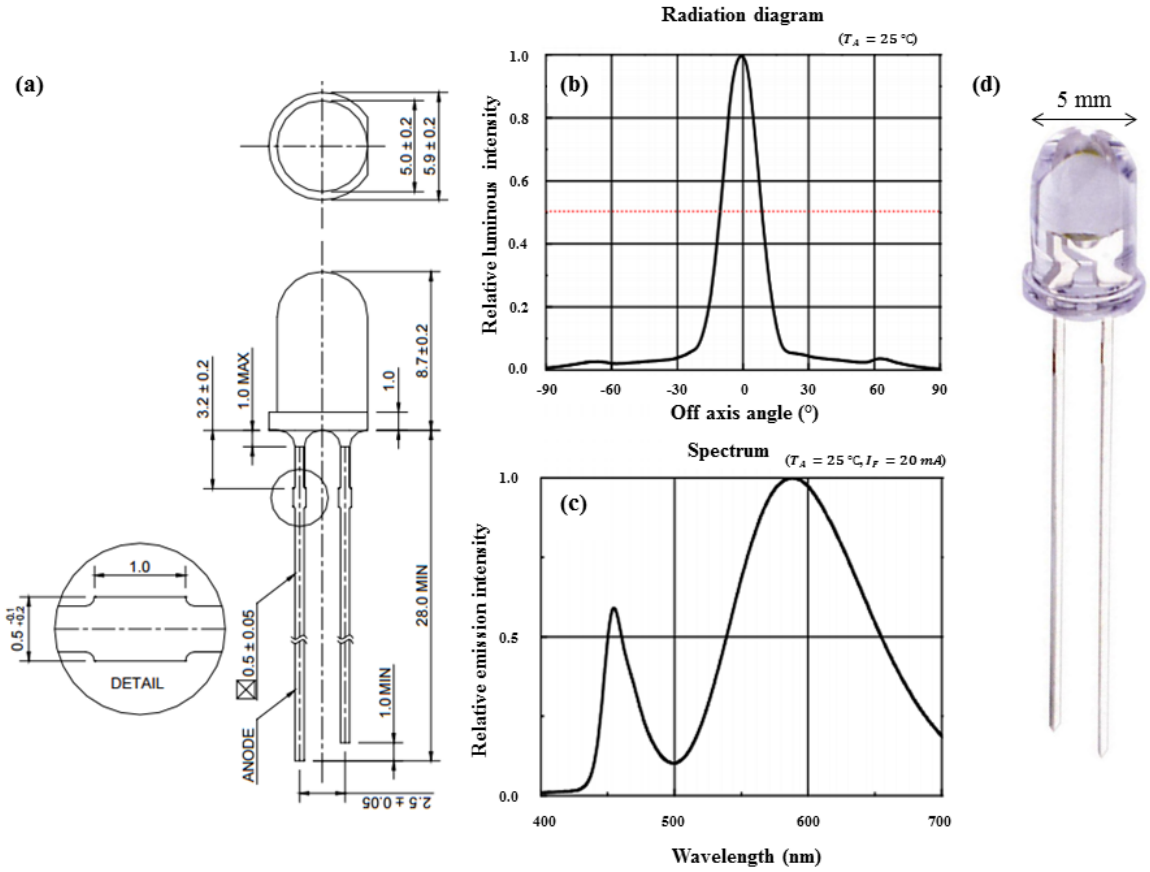

Fig. C.1 (a) Physical dimensions, (b) radiation diagram, (c) spectral characteristics, and (d) photograph of LM520A.

Appendix D: Derivation for circular ring array

The irradiance, E, of a circular ring array of four light emitting diodes (LEDs) at 0° illumination angle and radius r_0 can be written as the sum of the irradiances for $N \geq 3$ LEDs [108]. Since the *z*-axis in the Cartesian coordinates is essentially the working distance, l, of the imaging system, E can be expressed as

$$E(x, y, l) = l^m L_{LED} A_{LED} \sum_{n=1}^{N} \left\{ \left[x - r_0 \cos\left(\frac{2\pi n}{N}\right) \right]^2 + \left[y - r_0 \sin\left(\frac{2\pi n}{N}\right) \right]^2 + l^2 \right\}^{-(m+2)/2}, \tag{3.7}$$

where L_{LED} is the radiance in watts per meters squared per steradian ($W\ m^{-2}\ sr^{-1}$), and A_{LED} is the LED emitting area in meters squared (m^2).

The variable r_0 can be optimized in order to achieve uniform irradiance distribution over the central region, particularly along the directions of $\cos\left(\frac{2\pi n}{4}\right)$ and $\sin\left(\frac{2\pi n}{4}\right)$. The concept here is same as the Sparrow's criterion in imaging resolution [108, 110]. The aim is to separate the irradiance patterns of the four LEDs, such that the irradiance slope variation is minimal over the central region (i.e. eliminating the implicit second-order term of Eq. (3.7)). The LED chips in the ring array should be coplanar, so that the symmetrical arrangement reduces the problem to one dimension. The maximally flat condition along the radial axis that crosses a LED can then be calculated without any loss of generality. In order to achieve the maximally flat condition [111] for r_0, E is partially differentiated twice with respect to x. Then, set $\frac{\partial^2 E}{\partial x^2} = 0$ at $x = 0$ and $y = 0$. Lastly, solve for r_0 with respect to m and l. The detailed derivation is shown below.

$$E(x,y,l) = l^m L_{LED} A_{LED} \sum_{n=1}^{N} \left\{ \left[x - r_0 \cos\left(\frac{2\pi n}{N}\right) \right]^2 + \left[y - r_0 \sin\left(\frac{2\pi n}{N}\right) \right]^2 + l^2 \right\}^{-(m+2)/2}$$

Since $(a-b)^2 = a^2 - 2ab + b^2$;

$$E(x,y,z) = l^m A_{LED} L_{LED} \sum_{n=1}^{N} \left\{ \left[x^2 - 2(x) r_0 \cos\left(\frac{2\pi n}{N}\right) + r_0^2 \cos^2\left(\frac{2\pi n}{N}\right) \right] + \left[y^2 - 2(y) r_0 \sin\left(\frac{2\pi n}{N}\right) + r_0^2 \sin^2\left(\frac{2\pi n}{N}\right) \right] + l^2 \right\}^{-(m+2)/2}$$

Given that $\sin^2\left(\frac{2\pi n}{N}\right) + \cos^2\left(\frac{2\pi n}{N}\right) = 1$,

$$E(x,y,z) = l^m A_{LED} L_{LED} \sum_{n=1}^{N} \left\{ \left[x^2 + y^2 - 2r_0 \left[(x) \cos\left(\frac{2\pi n}{N}\right) + (y) \sin\left(\frac{2\pi n}{N}\right) \right] + r_0^2 + l^2 \right] \right\}^{-(m+2)/2}$$

$$\frac{\partial E}{\partial x} = l^m A_{LED} L_{LED} \sum_{n=1}^{N} \left\{ \left(-\frac{(m+2)}{2} \right) \left[x^2 + y^2 - 2r_0 \left[(x) \cos\left(\frac{2\pi n}{N}\right) + (y) \sin\left(\frac{2\pi n}{N}\right) \right] + r_0^2 + l^2 \right]^{-(m+4)/2} \left[2x - 2r_0 \cos\left(\frac{2\pi n}{N}\right) \right] \right\}$$

$$\frac{\partial^2 E}{\partial x^2} = l^m A_{LED} L_{LED} \sum_{n=1}^{N} \left\{ \left(-\frac{(m+4)}{2} \right) \left(-\frac{(m+2)}{2} \right) \left[x^2 + y^2 \right. \right.$$

$$\left. - 2r_0 \left[(x) \cos\left(\frac{2\pi n}{N}\right) + (y) \sin\left(\frac{2\pi n}{N}\right) \right] + r_0^2 + l^2 \right]^{-(m+6)/2} \left[2x \right.$$

$$\left. - 2r_0 \cos\left(\frac{2\pi n}{N}\right) \right] \left[2x - 2r_0 \cos\left(\frac{2\pi n}{N}\right) \right]$$

$$+ 2 \left(-\frac{(m+2)}{2} \right) \left[x^2 + y^2 - 2r_0 \left[(x) \cos\left(\frac{2\pi n}{N}\right) + (y) \sin\left(\frac{2\pi n}{N}\right) \right] + r_0^2 \right.$$

$$\left. \left. + l^2 \right]^{-(m+4)/2} \right\}$$

$$\frac{\partial^2 E}{\partial x^2} = l^m A_{LED} L_{LED} \sum_{n=1}^{N} \left\{ \left(-\frac{(m+2)}{2} \right) \left(-\frac{(m+4)}{2} \right) \left[x^2 + y^2 \right. \right.$$

$$\left. - 2r_0 \left[(x) \cos\left(\frac{2\pi n}{N}\right) + (y) \sin\left(\frac{2\pi n}{N}\right) \right] + r_0^2 + l^2 \right]^{-(m+6)/2} \left[2x \right.$$

$$\left. - 2r_0 \cos\left(\frac{2\pi n}{N}\right) \right]^2$$

$$+ 2 \left(-\frac{(m+2)}{2} \right) \left[x^2 + y^2 - 2r_0 \left[(x) \cos\left(\frac{2\pi n}{N}\right) + (y) \sin\left(\frac{2\pi n}{N}\right) \right] + r_0^2 \right.$$

$$\left. \left. + l^2 \right]^{-(m+4)/2} \right\}$$

Let $\frac{\partial^2 E}{\partial x^2} = 0, x = y = 0$, and since $l^m A_{LED} L_{LED} \neq 0$,

$$0 = \sum_{n=1}^{N}\left(-\frac{(m+2)}{2}\right)\left(-\frac{(m+4)}{2}\right)(r_0^2 + l^2)^{-(m+6)/2}\left[-2r_0^2\cos\left(\frac{2\pi n}{N}\right)\right]^2$$

$$+ \sum_{n=1}^{N} 2\left(-\frac{(m+2)}{2}\right)(r_0^2 + l^2)^{-(m+4)/2}$$

$$0 = \sum_{n=1}^{N}\left(\frac{(m+2)}{2}\right)\left(\frac{(m+4)}{2}\right)(r_0^2 + l)^{-(m+6)/2}\left[4r_0^2\cos^2\left(\frac{2\pi n}{N}\right)\right]$$

$$- \sum_{n=1}^{N} 2\left(\frac{(m+2)}{2}\right)(r_0^2 + l^2)^{-(m+4)/2}$$

$$0 = \sum_{n=1}^{N}(m+2)(m+4)(r_0^2 + l^2)^{-(m+6)/2}\left[r_0^2\cos^2\left(\frac{2\pi n}{N}\right)\right]$$

$$- \sum_{n=1}^{N}(m+2)(r_0^2 + l^2)^{-(m+4)/2}$$

$$\sum_{n=1}^{N}(m+2)(m+4)(r_0^2 + l^2)^{-(m+6)/2}\left[r^2\cos^2\left(\frac{2\pi n}{N}\right)\right] = \sum_{n=1}^{N}(m+2)(r_0^2 + l^2)^{-(m+4)/2}$$

$$\sum_{n=1}^{N}(m+2)(m+4)(r_0^2 + l^2)^{-(m+6)/2}\left[r^2\cos^2\left(\frac{2\pi n}{N}\right)\right] = N(m+2)(r_0^2 + l^2)^{-(m+4)/2}$$

Divide throughout by $(m+2)(r_0^2 + l^2)^{-(m+6)/2}$ such that

$$(m+4)r_0^2\sum_{n=1}^{N}\left[\cos^2\left(\frac{2\pi n}{N}\right)\right] = N(r_0^2 + l^2)^{-(m+4)/2-[-(m+6)/2]}$$

$$(m+4)r_0^2\sum_{n=1}^{N}\left[\cos^2\left(\frac{2\pi n}{N}\right)\right] = N(r_0^2 + l^2)$$

$$\sum_{n=1}^{N}\left[\cos^2\left(\frac{2\pi n}{N}\right)\right] = \frac{1}{(m+4)r_0^2}N(r_0^2 + l^2)$$

$$\frac{N}{2} = \frac{1}{(m+4)r_0^2}N(r_0^2 + l^2)$$

Divide by N throughout, therefore

$$\frac{1}{2} = \frac{1}{(m+4)r_0^2}(r_0^2 + l^2)$$

$$mr^2 + 4r_0^2 = 2{r_0}^2 + 2l^2$$

$$2l^2 = (m + 4 - 2)r_0^2$$

$$2l^2 = (m+2)r_0^2$$

$$r_0^2 = \frac{2l^2}{m+2}$$

$$r_0 = \sqrt{\frac{2l^2}{m+2}}$$

$$r_0 = \sqrt{\frac{2}{m+2}}\,l$$

Appendix E: MATLAB® script for LED design equation

As seen from Eq. (3.10), the design equation for circular ring array of light emitting diodes (LEDs) at an angle is bounded by four parameters. Because the viewing angle of LED and hence m, cannot be continuously adjusted, it is more convenient to consider only three variables for optimization. Therefore, for a given value of m, the illumination angle α, ring array radius r, and working distance l, have to be carefully considered in order to achieve uniform irradiance. LEDs with viewing angles of 20°, 30°, and 40° were considered for this analysis.

For 20° viewing angle LED

```
% Setting the values of the working distance, illumination angle, and LED viewing angle
L = 5;
a = [0:1:60];
LED = 20;

%% Working out the values of m
m = ((-log(2))/(log(cosd(LED/2))));

%% Working out the value of array radius (r1) using Eq. (3.10)
r1 = ((tand(a))+(sqrt(2/(m+2))))*L;

%% Plot graph of array radius against illumination angle
plot(a,r1);
hold on

%% Repeat for different values of L
% For L = 10
L = 10;
r1 = ((tand(a))+(sqrt(2/(m+2))))*L;
plot(a,r1);

% For L = 15
L = 15;
r1 = ((tand(a))+(sqrt(2/(m+2))))*L;
plot(a,r1);
```

```
% For L = 20
L = 20;
r1 = ((tand(a))+(sqrt(2/(m+2))))*L;
plot(a,r1);
```

For 30° viewing angle LED

```
% Setting the values of the working distance, illumination angle, and LED viewing angle
L = 5;
a = [0:1:60];
LED = 30;

%% Working out the values of m
m = ((-log(2))/(log(cosd(LED/2))));

%% Working out the value of array radius (r1) using Eq. (3.10)
r1 = ((tand(a))+(sqrt(2/(m+2))))*L;

%% Plot graph of array radius against illumination angle
plot(a,r1);
hold on

%% Repeat for different values of L
% For L = 10
L = 10;
r1 = ((tand(a))+(sqrt(2/(m+2))))*L;
plot(a,r1);

% For L = 15
L = 15;
r1 = ((tand(a))+(sqrt(2/(m+2))))*L;
plot(a,r1);

% For L = 20
L = 20;
r1 = ((tand(a))+(sqrt(2/(m+2))))*L;
plot(a,r1);
```

For 40° viewing angle LED

```
% Setting the values of the working distance, illumination angle, and LED viewing angle
L = 5;
a = [0:1:60];
LED = 40;
```

```
%% Working out the values of m
m = ((-log(2))/(log(cosd(LED/2))));

%% Working out the value of array radius (r1) using Eq. (3.10)
r1 = ((tand(a))+(sqrt(2/(m+2))))*L;

%% Plot graph of array radius against illumination angle
plot(a,r1);
hold on

%% Repeat for different values of L
% For L = 10
L = 10;
r1 = ((tand(a))+(sqrt(2/(m+2))))*L;
plot(a,r1);

% For L = 15
L = 15;
r1 = ((tand(a))+(sqrt(2/(m+2))))*L;
plot(a,r1);

% For L = 20
L = 20;
r1 = ((tand(a))+(sqrt(2/(m+2))))*L;
plot(a,r1);
```

Appendix F: Photograph of micro ScoutCam™ 3.0 and processor

The photograph of the micro ScoutCam™ 3.0 and processor is shown in Fig. F.1.

Fig. F.1 Photograph of micro ScoutCam™ 3.0 and processor.

Appendix G: Spatial resolution characterization test for Bessel beam microscopy

Using a 1951 USAF resolution test target as reference, spatial resolution characterization tests were performed with various optical configurations as shown in Fig. G.1.

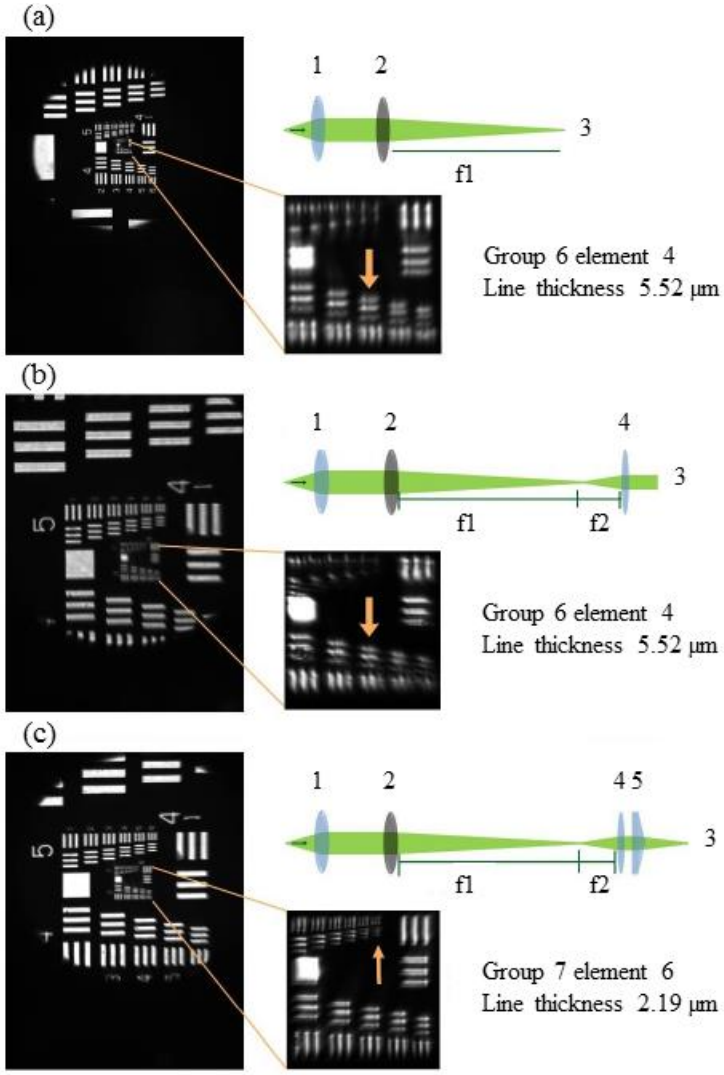

Fig. G.1 (a) Classical system, (b) classical system with bi-convex lens, and (c) Bessel beam microscopy.

These configurations include a classical system consisting of an objective lens (LSM03-VIS, ThorLabs Inc., NJ, USA) and an infinity-corrected tube lens (ITL200, ThorLabs Inc., NJ, USA), the above mentioned classical system and a N-BK7 bi-convex lens (LB1844-A, ThorLabs Inc., NJ, USA), and the above mentioned classical system with a N-BK7 bi-convex lens and a 176° apex angle plano-convex axicon lens (Altechna Co. Ltd.,Vilnius, Lithuania). The infinity-corrected tube lens and the bi-convex lens are separated by a distance equal to the sum of their focal lengths. The results of the spatial resolution characterization test are shown in Fig. G.1.

Comparing Fig. G.1(a) and Fig. G.1(b), it is noted that the presence of the bi-convex lens merely increases the magnification (~2.66X). Image resolution is not improved. Both configurations were able to image up to group 6, element 4 of the 1951 USAF resolution test target. For Fig. G.1(c) however, the optical configuration was able to image up to group 7, element 6, the highest spatial frequency on the 1951 USAF resolution test target. This corresponds to a spatial resolution of about 2.19 μm. Theoretically, the spatial resolution of the Bessel beam microscopy configuration is [177]

$$d_{min} = f_{LSM03-VIS}\frac{2.405\,\lambda D}{2\pi\gamma(n-1)L}, \tag{4.1}$$

where d_{min} is the minimum resolvable distance between two point sources, $f_{LSM03-VIS}$ is the effective focal length of the LSM03-VIS, λ is the wavelength of light, D is the degree to which the point spread function is focused or defocused, γ is the physical angle of the plano-convex axicon lens, n is the refractive index of the axicon lens, and L is the distance between the plano-convex axicon lens and the camera. The values of these parameters are given in Table G.1. Using these values, $d_{min} = 2.01\ \mu m$, and the theoretical result corroborates with the experimental

result. The improvement in resolution is evident as seen from Fig. G.1(c). It is also noted that there is a demagnification of ~0.86X compared to Fig. G.1(b).

Table G.1 Parameters for Bessel beam microscopy configuration.

Parameters for Bessel beam microscopy configuration	
$f_{LSM03-VIS}$	25.1 mm
λ	540 nm
D	1
γ	2°
n	1.46
L	160 mm

Appendix H: Simulated eye model and goniotomy lens

Here, an eye model with four centered aspheric surfaces is simulated in Zemax [178]. Each surface is defined by its asphericity and radius. The asphericities values are anatomical measurements of the human eyes [179]. The three dimensional (3D) model of the simulated eye and its parameters are shown in Table H.1.

Table H.1 3D model of simulated eye and its parameters.

Surface type	Radius (mm)	Thickness (mm)	Refractive index	Aspherical
Anterior cornea	7.72	0.55	1.367	-0.26
Posterior cornea (aqueous)	6.50	3.05	1.3374	0
Anterior lens	10.20	4	1.42	-3.1316
Posterior lens (vitreous)	-6.00	16.4	1.336	-1.0

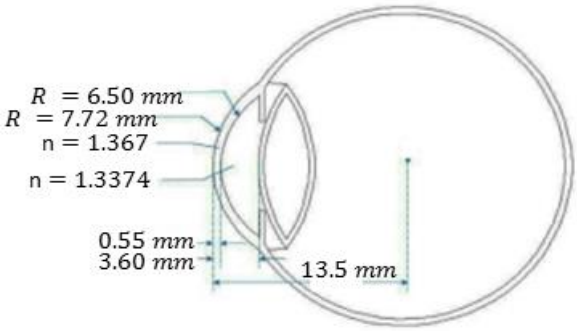

A Zemax model of the Hoskins-Barkan Adult Goniotomy Lens is created based on its design specifications. Fig. H.1 shows the 3D model of the simulated goniotomy lens and eye model. Only the chief ray is illustrated in Fig. H.1.

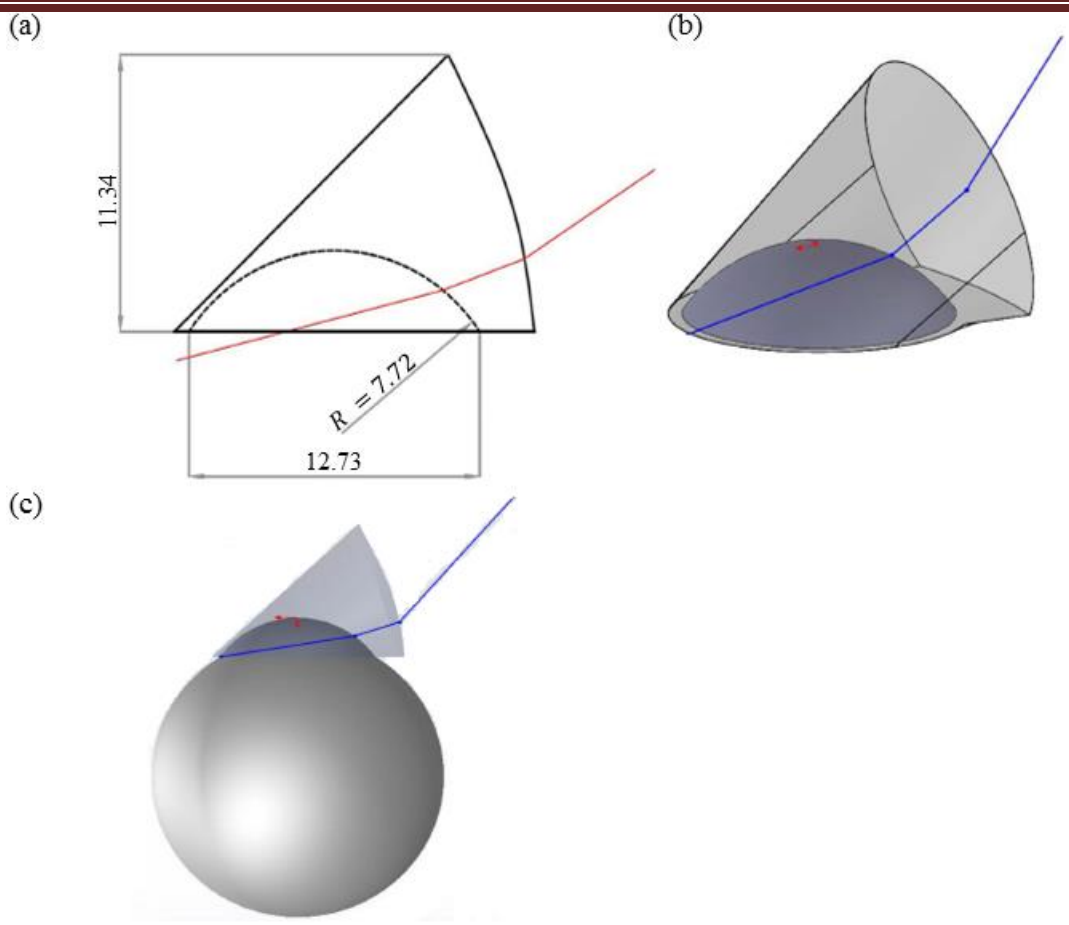

Fig. H.1 (a) Cross section, (b) 3D model, and (c) illustration of goniotomy lens on eye.

Appendix I: Design and fabrication of system packaging

The apparatus for the non-contact imaging of cornea and aqueous outflow system (AOS) is shown in Fig. 6.13. The system packaging for the illumination and detection arms are designed and fabricated using computer-aided design software, SolidWorks, and are shown in Fig. I.1 and Fig. I.2 respectively.

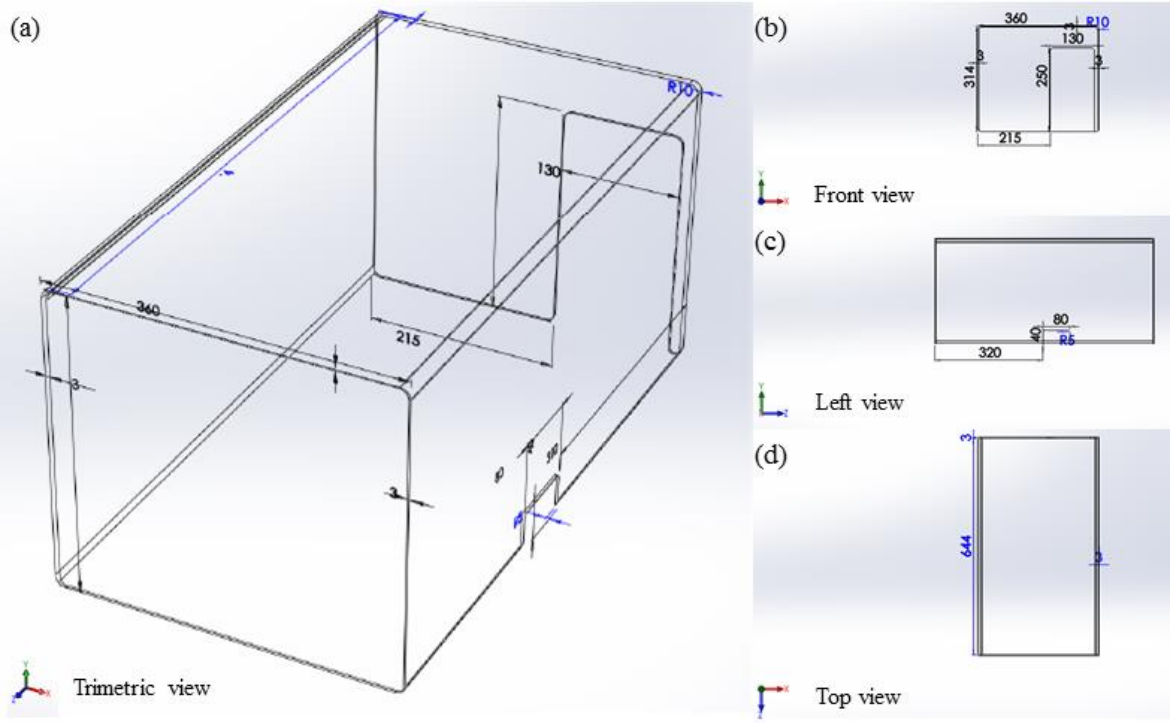

Fig. I.1 (a) Trimetric view, (b) front view, (c) left view, and (d) top view of system packaging for illumination arm/ corneal imaging module.

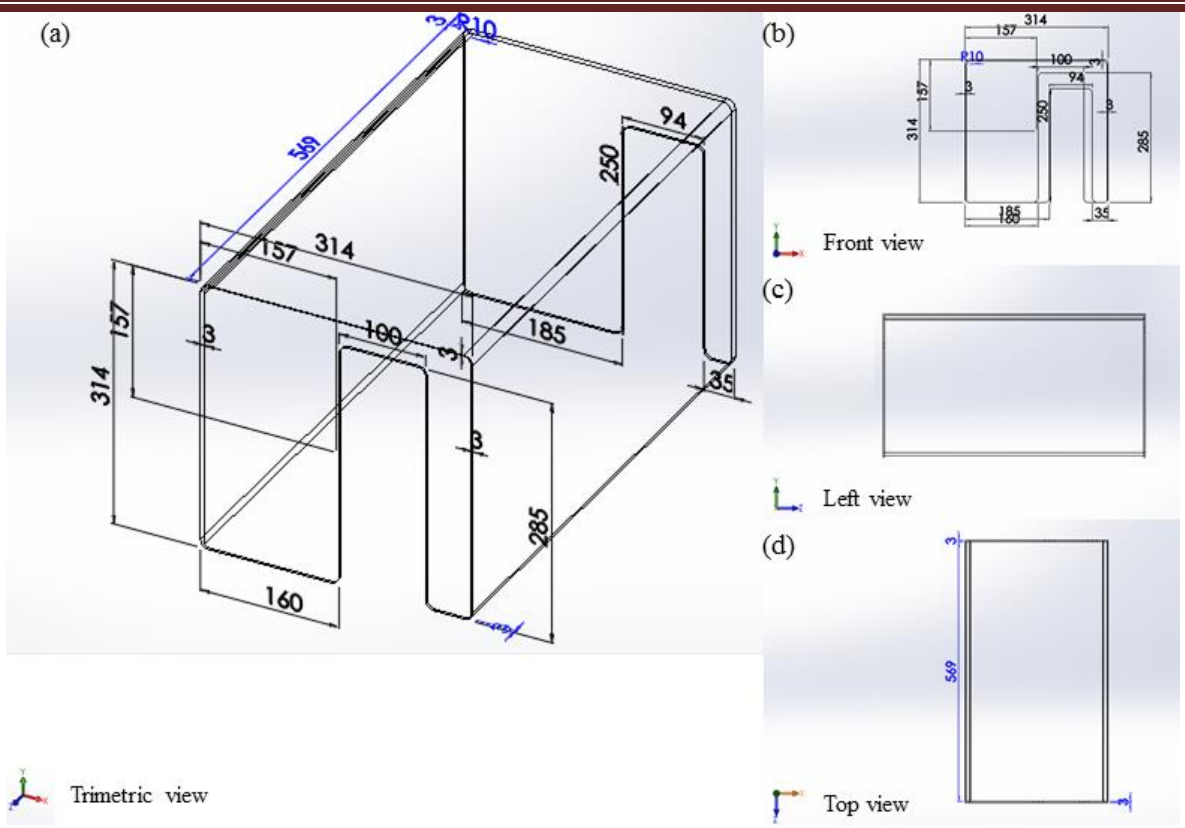

Fig. I.2 (a) Trimetric view, (b) front view, (c) left view, and (d) top view of system packaging for detection arm.

Appendix J: *In vivo* confocal microscopy of New Zealand white rabbit

In vivo confocal microscopy of the cornea was conducted with a commercial laser scanning confocal microscopy (LSCM) system after exposing the New Zealand white rabbit to near infrared laser at 785 nm wavelength. This was to ensure that the cells were not damaged due to exposure to laser light at this wavelength and power. The procedure was conducted with Heidelberg Retinal Tomography III Rostock Cornea Module as stated in Section 2.3.2.3 and the results are shown in Fig. J.1.

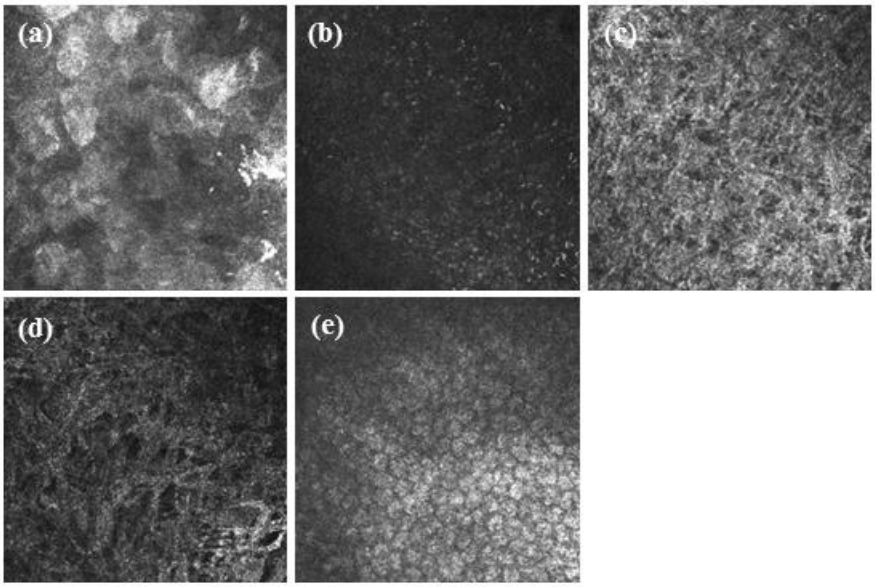

Fig. J.1 LSCM images of the New Zealand white rabbit showing the (a) superficial epithelium, (b) basal membrane, (c) anterior stroma, (d) posterior stroma, and (e) endothelium cells.

Appendix K: Derivation for linear array

For two linear light emitting diodes (LEDs) array at 0° illumination, the irradiance E is given by the sum of the irradiances of the individual LEDs, and s is the distance between the two LEDs, where

$$E(x,y,l) = l^m A_{LED} L_{LED} \left\{ \left[\left(x - \frac{s}{2} \right)^2 + y^2 + l^2 \right]^{-\frac{(m+2)}{2}} + \left[\left(x + \frac{s}{2} \right)^2 + y^2 + l^2 \right]^{-\frac{(m+2)}{2}} \right\}. \quad (7.1)$$

The concept discussed in Section 3.3 can also be applied here to achieve uniform irradiance distribution for linear LED array. The aim is to optimize the separation distance, s, such that the irradiance slope variation is minimal, and the implicit second-order term of Eq. (7.1) disappears. In order to achieve the maximally flat condition for s, E is partially differentiated twice with respect to x. Then, set $\frac{\partial^2 E}{\partial x^2} = 0$ at $x = 0$ and $y = 0$. Lastly, solve for s with respect to m and l. The detailed derivation is shown below.

$$E(x,y,l) = l^m A_{LED} L_{LED} \left\{ \left[\left(x - \frac{s}{2} \right)^2 + y^2 + l^2 \right]^{-\frac{(m+2)}{2}} + \left[\left(x + \frac{s}{2} \right)^2 + y^2 + l^2 \right]^{-\frac{(m+2)}{2}} \right\}$$

$$\frac{\partial E}{\partial x} = l^m A_{LED} L_{LED} \left\{ \left(-\frac{(m+2)}{2} \right) \left[\left(x - \frac{s}{2} \right)^2 + y^2 + l^2 \right]^{-\frac{(m+4)}{2}} (2) \left(x - \frac{s}{2} \right) \right.$$

$$\left. + \left(-\frac{(m+2)}{2} \right) \left[\left(x + \frac{s}{2} \right)^2 + y^2 + l^2 \right]^{-\frac{(m+4)}{2}} (2) \left(x + \frac{s}{2} \right) \right\}$$

$$\frac{\partial^2 E}{\partial x^2} = l^m A_{LED} L_{LED} \left\{ \left[\left(-\frac{(m+4)}{2} \right) \left(-\frac{(m+2)}{2} \right) \left[\left(x - \frac{s}{2} \right)^2 + y^2 + l^2 \right]^{-\frac{(m+6)}{2}} (2) \left(x \right. \right. \right.$$

$$\left. - \frac{s}{2} \right) (2) \left(x - \frac{s}{2} \right) + \left(-\frac{(m+2)}{2} \right) \left[\left(x - \frac{s}{2} \right)^2 + y^2 + l^2 \right]^{-\frac{(m+4)}{2}} (2) \Bigg]$$

$$+ \left[\left(-\frac{(m+4)}{2} \right) \left(-\frac{(m+2)}{2} \right) \left[\left(x + \frac{s}{2} \right)^2 + y^2 + l^2 \right]^{-\frac{(m+6)}{2}} (2) \left(x \right. \right.$$

$$\left. \left. \left. + \frac{s}{2} \right) (2) \left(x + \frac{s}{2} \right) + \left(-\frac{(m+2)}{2} \right) \left[\left(x + \frac{s}{2} \right)^2 + y^2 + l^2 \right]^{-\frac{(m+4)}{2}} (2) \right] \right\}$$

Let $\frac{\partial^2 E}{\partial x^2} = 0$, $x = y = 0$, and since $l^m A_{LED} L_{LED} \neq 0$,

$$0 = \left\{\left(-\frac{(m+4)}{2}\right)\left(-\frac{(m+2)}{2}\right)\left[\left(-\frac{s}{2}\right)^2 + l^2\right]^{-\frac{(m+6)}{2}}(2)\left(-\frac{s}{2}\right)(2)\left(-\frac{s}{2}\right)\right.$$

$$\left. + \left(-\frac{(m+2)}{2}\right)\left[\left(-\frac{s}{2}\right)^2 + l^2\right]^{-\frac{(m+4)}{2}}(2)\right\}$$

$$+ \left\{\left(-\frac{(m+4)}{2}\right)\left(-\frac{(m+2)}{2}\right)\left[\left(\frac{s}{2}\right)^2 + l^2\right]^{-\frac{(m+6)}{2}}(2)\left(\frac{s}{2}\right)(2)\left(\frac{s}{2}\right)\right.$$

$$\left. + \left(-\frac{(m+2)}{2}\right)\left[\left(\frac{s}{2}\right)^2 + l^2\right]^{-\frac{(m+4)}{2}}(2)\right\}$$

$$0 = \left[\left(\frac{(m+4)}{2}\right)\left(\frac{(m+2)}{2}\right)\left(\frac{s^2}{4} + l^2\right)^{-\frac{(m+6)}{2}}(s^2) - \left(\frac{(m+2)}{2}\right)\left(\frac{s^2}{4} + l^2\right)^{-\frac{(m+4)}{2}}(2)\right]$$

$$+ \left[\left(\frac{(m+4)}{2}\right)\left(\frac{(m+2)}{2}\right)\left(\frac{s^2}{4} + l^2\right)^{-\frac{(m+6)}{2}}(s^2)\right.$$

$$\left. - \left(\frac{(m+2)}{2}\right)\left(\frac{s^2}{4} + l^2\right)^{-\frac{(m+4)}{2}}(2)\right]$$

Divide throughout by $\left(\frac{(m+2)}{2}\right)$, we get

$$0 = \left(\frac{(m+4)}{2}\right)\left(\frac{s^2}{4} + l^2\right)^{-\frac{(m+6)}{2}}(s^2) - \left(\frac{s^2}{4} + l^2\right)^{-\frac{(m+4)}{2}}(2)$$

$$+ \left(\frac{(m+4)}{2}\right)\left(\frac{s^2}{4} + l^2\right)^{-\frac{(m+6)}{2}}(s^2) - \left(\frac{s^2}{4} + l^2\right)^{-\frac{(m+4)}{2}}(2)$$

$$(2)\left(\frac{(m\ +4)}{2}\right)\left(\frac{s^2}{4}\ +\ l^2\right)^{-\frac{(m\ +6)}{2}}(s^2)\ =\ (2)(2)\left(\frac{s^2}{4}\ +\ l^2\right)^{-\frac{(m\ +4)}{2}}$$

Divide throughout by $\left(\frac{s^2}{4}\ +\ l^2\right)^{-\frac{(m\ +6)}{2}}$

$$(2)\left(\frac{(m\ +4)}{2}\right)(s^2)\ =\ (2)(2)\left(\frac{s^2}{4}\ +\ l^2\right)$$

Divide throughout by 4, and make s the subject such that

$$\left(\frac{(m\ +4)}{4}\right)(s^2)\ =\ \frac{s^2}{4}\ +\ l^2$$

$$\left(\frac{(m\ +4)}{4}\right)(s^2)\ -\ \frac{s^2}{4}\ =\ l^2$$

$$s^2\left[\left(\frac{m\ +\ 4}{4}\right)\ -\ \frac{1}{4}\right]\ =\ l^2$$

$$s^2\left(\frac{m\ +\ 3}{4}\right)\ =\ l^2$$

$$s^2\ =\ \left(\frac{4}{m\ +3}\right)l^2$$

$$s\ =\ \sqrt{\frac{4}{m\ +3}}$$

Appendix L: Quantifying trabecular meshwork pigmentation

The potential of the axicon assisted gonioscopy imaging system in quantifying the trabecular meshwork (TM) pigmentation is demonstrated here. Six anatomically open angles of the *ex vivo* porcine samples are chosen for this study. The results are shown in Fig. L.1.

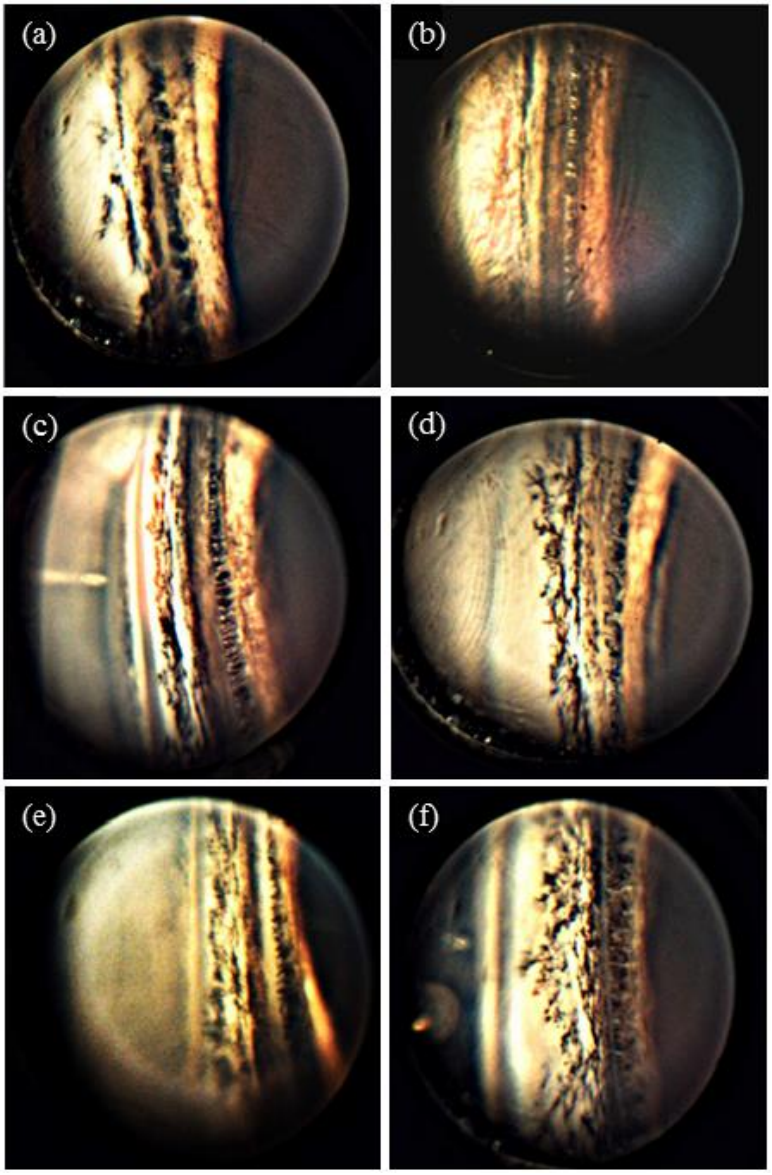

Fig. L.1 ICA images of *ex vivo* porcine samples with different levels of pigmentation.

List of publications

Journal papers

[1]. **Xun Jie Jeesmond Hong**, V.K. Shinoj, V.M. Murukeshan, M. Baskaran, and T. Aung, "A simple and non-contact optical imaging probe for evaluation of corneal diseases," *Review of Scientific Instruments* **86**(9), 093702 (2015).

[2]. **Xun Jie Jeesmond Hong**, V.K. Shinoj, V.M. Murukeshan, M. Baskaran, and Tin Aung, "Imaging of trabecular meshwork using Bessel-Gauss light sheet with fluorescence," *Laser Physics Letter* **14**(3), 035602 (2017).

[3]. **Xun Jie Jeesmond Hong**, Vengalathunadakal K. Shinoj, Vadakke Matham Murukeshan, Mani Baskaran, and Tin Aung, "Preclinical imaging of iridocorneal angle and fundus using a modified integrated flexible handheld probe," *Journal of Medical Imaging* **4**(2), 026001 (2017).

[4]. V.K. Shinoj, **Xun Jie Jeesmond Hong**, V.M. Murukeshan, M. Baskaran, Tin Aung, "Progress in anterior chamber angle imaging for glaucoma risk prediction – A review on clinical equipment, practice and research," *Medical Engineering and Physics* **38**(12), 1383-1391 (2016).

[5]. Sandeep Menon Perinchery, Anant Shinde, Chan Yiu Fu, **Xun Jie Jeesmond Hong**, Mani Baskaran, Tin Aung, and Vadakke Matham Murukeshan, "High resolution iridocorneal angle imaging system by axicon lens assisted gonioscopy," *Scientific Reports* **6**, 30844 (2016).

[6]. **Xun Jie Jeesmond Hong**, Vengalathunadakal K. Shinoj, Vadakke Matham Murukeshan, Mani Baskaran, and Tin Aung, "A method and apparatus for the non-contact imaging of cornea and aqueous outflow system," To be communicated.

Conference papers

[1]. **Xun Jie Jeesmond Hong**, V.K. Shinoj, V.M. Murukeshan, M. Baskaran, and Tin Aung, "*In-vivo* high resolution corneal imaging and analysis on animal models for clinical applications," *Proc. of SPIE* **9524**, 95241J (2015).

[2]. **Xun Jie Jeesmond Hong**, V.K. Shinoj, V.M. Murukeshan, M. Baskaran, and Tin Aung, "Contact lens assisted imaging with integrated flexible handheld probe for glaucoma diagnosis," *Proc. of SPIE* **10449**, 1044908 (2017).

[3]. **Xun Jie Jeesmond Hong**, V.K. Shinoj, V.M. Murukeshan, M. Baskaran, and Tin Aung, "Geometric approach to the design of an imaging probe to evaluate the iridocorneal angle structures," *Proc. of SPIE* **10449**, 104490B (2017).

[4]. V.K. Shinoj, **Xun Jie Jeesmond Hong**, V.M. Murukeshan, M. Baskaran, and Tin Aung, "Dual-illumination mode, wide-field probe imaging scheme for imaging irido-corneal angle region inside eye," *Proc. of SPIE* **9524**, 95241L (2015).

[5]. V.M. Murukeshan, **Xun Jie Jeesmond Hong**, V.K. Shinoj, M. Baskaran, and Tin Aung, "Non-contact high resolution Bessel beam probe for diagnostic imaging of cornea and trabecular meshwork region in eye," *Proc. of SPIE* **9537**, 953728 (2015).

Patent and technical disclosure

Patent

[1]. V.M. Murukeshan, V.K. Shinoj, **Xun Jie Jeesmond Hong**, M. Baskaran and Aung Tin, "Imaging device and method for imaging specimens", **PCT/SG2016/050089** (2016).

Technical disclosure

[1]. V.M. Murukeshan, V.K. Shinoj, **Xun Jie Jeesmond Hong**, M. Baskaran and Aung Tin, "A method and apparatus for high resolution corneal imaging and aqueous outflow system inside eye using Bessel-beam based light sheet configuration", Nanyang Innovation & Enterprise Office (NIEO), **TD/200/14** (2014).

References

1. Leung, C.K.-s., et al., *Anterior chamber angle measurement with anterior segment optical coherence tomography: a comparison between slit lamp OCT and Visante OCT.* Investigative ophthalmology & visual science, 2008. **49**(8): p. 3469-3474.
2. Brennen, P.M., L. Kagemann, and T.R. Friberg, *Comparison of StratusOCT and Cirrus HD-OCT imaging in macular diseases.* Ophthalmic surgery, lasers & imaging: the official journal of the International Society for Imaging in the Eye, 2009. **40**(1): p. 25.
3. Baskaran, M., et al., *Assessment of Circumferential Angle-Closure by the Iris–Trabecular Contact Index with Swept-Source Optical Coherence Tomography.* Ophthalmology, 2013. **120**(11): p. 2226-2231.
4. Kurbanyan, K., et al., *Corneal nerve alterations in acute Acanthamoeba and fungal keratitis: an in vivo confocal microscopy study.* Eye, 2012. **26**(1): p. 126-132.
5. Pavlin, C., et al., *Clinical use of ultrasound biomicroscopy.* Ophthalmology, 1991. **98**(3): p. 287-295.
6. Sakata, L.M., et al., *Comparison of gonioscopy and anterior segment ocular coherence tomography in detecting angle closure in different quadrants of the anterior chamber angle.* Ophthalmology, 2008. **115**(5): p. 769-774.
7. Oliveira, C.M., C. Ribeiro, and S. Franco, *Corneal imaging with slit-scanning and Scheimpflug imaging techniques.* Clinical and Experimental Optometry, 2011. **94**(1): p. 33-42.
8. Oliver, J.E., et al., *Blindness and glaucoma: a comparison of patients progressing to blindness from glaucoma with patients maintaining vision.* American journal of ophthalmology, 2002. **133**(6): p. 764-772.
9. Resnikoff, S., et al., *Global data on visual impairment in the year 2002.* Bulletin of the world health organization, 2004. **82**(11): p. 844-851.
10. Whitcher, J.P., M. Srinivasan, and M.P. Upadhyay, *Corneal blindness: a global perspective.* Bulletin of the World Health Organization, 2001. **79**(3): p. 214-221.
11. Keay, L., et al., *Microbial keratitis: predisposing factors and morbidity.* Ophthalmology, 2006. **113**(1): p. 109-116.
12. Yorston, D., M. Wood, and A. Foster, *Penetrating keratoplasty in Africa: graft survival and visual outcome.* British Journal of Ophthalmology, 1996. **80**(10): p. 890-894.
13. Weisbrod, D.J., et al., *Outcomes of repeat penetrating keratoplasty and risk factors for graft failure.* Cornea, 2003. **22**(5): p. 429-434.
14. Schwartz, E., et al., *Blindness and visual impairment in a region endemic for onchocerciasis in the Central African Republic.* British Journal of Ophthalmology, 1997. **81**(6): p. 443-447.
15. Pizzarello, L., et al., *Vision 2020: The right to sight: a global initiative to eliminate avoidable blindness.* Archives of Ophthalmology, 2004. **122**(4): p. 615-620.

16. Lagali, N., et al., *Laser-scanning in vivo confocal microscopy of the cornea: imaging and analysis methods for preclinical and clinical applications*. 2013: INTECH Open Access Publisher.
17. Jalbert, I., et al., *In vivo confocal microscopy of the human cornea.* British Journal of Ophthalmology, 2003. **87**(2): p. 225-236.
18. Fung, M.W., et al., *Corneal Topography and Imaging.* Netscape: eMedicine Specialties, Clinical Procedures, Ophthalmologic Procedures. Net article, an overview, 2009. **1196836**.
19. Ishikawa, H., et al., *Inadvertent corneal indentation can cause artifactitious widening of the iridocorneal angle on ultrasound biomicroscopy.* Ophthalmic surgery and lasers, 1999. **31**(4): p. 342-345.
20. Huang, D., et al., *Optical coherence tomography.* Science, 1991. **254**(5035): p. 1178-1181.
21. Keller, P.J., et al., *Fast, high-contrast imaging of animal development with scanned light sheet-based structured-illumination microscopy.* Nature methods, 2010. **7**(8): p. 637-642.
22. Planchon, T.A., et al., *Rapid three-dimensional isotropic imaging of living cells using Bessel beam plane illumination.* Nature methods, 2011. **8**(5): p. 417-423.
23. Gao, L., et al., *3D live fluorescence imaging of cellular dynamics using Bessel beam plane illumination microscopy.* nature protocols, 2014. **9**(5): p. 1083-1101.
24. Wolf, E., *Anatomy of the eye orbit.* 1976.
25. Kolb, H., *Gross anatomy of the eye.* 2007.
26. Johnson, M. and R. Kamm, *The role of Schlemm's canal in aqueous outflow from the human eye.* Investigative ophthalmology & visual science, 1983. **24**(3): p. 320-325.
27. Hoyng, P.F. and L.M. van Beek, *Pharmacological therapy for glaucoma.* Drugs, 2000. **59**(3): p. 411-434.
28. Quigley, H.A., D.S. Friedman, and N.G. Congdon, *Possible mechanisms of primary angle-closure and malignant glaucoma.* Journal of glaucoma, 2003. **12**(2): p. 167-180.
29. Stone, E.M., et al., *Identification of a gene that causes primary open angle glaucoma.* Science, 1997. **275**(5300): p. 668-670.
30. Nolan, W.P., et al., *Detection of primary angle closure using anterior segment optical coherence tomography in Asian eyes.* Ophthalmology, 2007. **114**(1): p. 33-39.
31. Janssen, S.F., et al., *The vast complexity of primary open angle glaucoma: disease genes, risks, molecular mechanisms and pathobiology.* Progress in retinal and eye research, 2013. **37**: p. 31-67.
32. Gordon, M.O., et al., *The Ocular Hypertension Treatment Study: baseline factors that predict the onset of primary open-angle glaucoma.* Archives of ophthalmology, 2002. **120**(6): p. 714-720.
33. Mitchell, P., et al., *Open-angle glaucoma and diabetes: the Blue Mountains eye study, Australia.* Ophthalmology, 1997. **104**(4): p. 712-718.
34. Wang, N., H. Wu, and Z. Fan, *Primary angle closure glaucoma in Chinese and Western populations.* Chinese medical journal, 2002. **115**(11): p. 1706-1715.
35. Campbell, D.G., *Ghost cell glaucoma following trauma.* Ophthalmology, 1981. **88**(11): p. 1151-1158.

36. Parisi, V. *Correlation between morphological and functional retinal impairment in patients affected by ocular hypertension, glaucoma, demyelinating optic neuritis and Alzheimer’ s disease*. in *Seminars in ophthalmology*. 2003. Informa UK Ltd UK.
37. Kaushik, S., et al., *Intractable glaucoma following intravitreal triamcinolone in central retinal vein occlusion.* American journal of ophthalmology, 2004. **137**(4): p. 758-760.
38. Doughty, M.J. and M.L. Zaman, *Human corneal thickness and its impact on intraocular pressure measures: a review and meta-analysis approach.* Survey of ophthalmology, 2000. **44**(5): p. 367-408.
39. Devereux, J.G., et al., *Anterior chamber depth measurement as a screening tool for primary angle-closure glaucoma in an East Asian population.* Archives of ophthalmology, 2000. **118**(2): p. 257.
40. Alsbirk, P., *Primary angle-closure glaucoma. Oculometry, epidemiology, and genetics in a high risk population.* Acta ophthalmologica. Supplementum, 1976(127): p. 5.
41. Lowe, R.F., *Aetiology of the anatomical basis for primary angle-closure glaucoma. Biometrical comparisons between normal eyes and eyes with primary angle-closure glaucoma.* The British journal of ophthalmology, 1970. **54**(3): p. 161.
42. Sihota, R., et al., *Ocular parameters in the subgroups of angle closure glaucoma.* Clinical & experimental ophthalmology, 2000. **28**(4): p. 253-258.
43. Weinreb, R.N., T. Aung, and F.A. Medeiros, *The pathophysiology and treatment of glaucoma: a review*. Jama, 2014. **311**(18): p. 1901-1911.
44. Quigley, H.A. and A.T. Broman, *The number of people with glaucoma worldwide in 2010 and 2020.* British journal of ophthalmology, 2006. **90**(3): p. 262-267.
45. Chew, P.T. and T. Aung, *Primary angle-closure glaucoma in Asia.* Journal of glaucoma, 2001. **10**(5): p. S7-S8.
46. Foster, P.J. and G.J. Johnson, *Glaucoma in China: how big is the problem?* British Journal of Ophthalmology, 2001. **85**(11): p. 1277-1282.
47. Dandona, L., et al., *Angle-closure glaucoma in an urban population in southern India: the Andhra Pradesh Eye Disease Study.* Ophthalmology, 2000. **107**(9): p. 1710-1716.
48. Hattenhauer, M.G., et al., *The probability of blindness from open-angle glaucoma.* Ophthalmology, 1998. **105**(11): p. 2099-2104.
49. Scheimpflug, T., *Improved method and apparatus for the systematic alteration or distortion of plane pictures and images by means of lenses and mirrors for photography and for other purposes.* GB patent, 1904. **1196**.
50. Jain, R. and S. Grewal, *Pentacam: Principle and Clinical Applications.* Journal of Current Glaucoma Practice, 2009. **3**(2): p. 20-32.
51. See, J.L.S., *Imaging of the anterior segment in glaucoma.* Clinical & experimental ophthalmology, 2009. **37**(5): p. 506-513.
52. Quek, D.T., et al., *Angle imaging: Advances and challenges.* Indian journal of ophthalmology, 2011. **59**(Suppl1): p. S69.
53. Coleman, A.L., F. Yu, and S.J. Evans, *Use of gonioscopy in medicare beneficiaries before glaucoma surgery.* Journal of glaucoma, 2006. **15**(6): p. 486-493.
54. Baskaran, M., et al., *Angle assessment by EyeCam, goniophotography, and gonioscopy.* Journal of glaucoma, 2012. **21**(7): p. 493-497.

55. Cheng, J., et al. *Closed angle glaucoma detection in RetCam images*. in *2010 Annual International Conference of the IEEE Engineering in Medicine and Biology Society, EMBC'10*. 2010.
56. Ahmed, I. and L. MacKeen, *A new approach to imaging the angle.* Glaucoma Today, 2007. **4**: p. 1-3.
57. Azad, R.V., et al., *Comparative evaluation of RetCam vs. gonioscopy images in congenital glaucoma.* Indian journal of ophthalmology, 2014. **62**(2): p. 163.
58. Sakata, L.M., et al., *Assessment of the scleral spur in anterior segment optical coherence tomography images.* Archives of Ophthalmology, 2008. **126**(2): p. 181.
59. Shinoj, V., et al., *Note: A gel based imaging technique of the iridocorneal angle for evaluation of angle-closure glaucoma.* Review of Scientific Instruments, 2014. **85**(6): p. 066105.
60. Radhakrishnan, S., et al., *Real-time optical coherence tomography of the anterior segment at 1310 nm.* Archives of Ophthalmology, 2001. **119**(8): p. 1179.
61. Fujimoto, J.G., et al., *Optical coherence tomography: an emerging technology for biomedical imaging and optical biopsy.* Neoplasia (New York, NY), 2000. **2**(1-2): p. 9.
62. Ahmed, I.I.K., *Anterior Segment Optical Coherence Tomography in Glaucoma.* Journal of Current Glaucoma Practice, 2009. **3**(1): p. 14-23.
63. Dorairaj, S., J.M. Liebmann, and R. Ritch, *Quantitative evaluation of anterior segment parameters in the era of imaging.* Transactions of the American Ophthalmological Society, 2007. **105**: p. 99.
64. Dinc, U.A., et al., *Quantitative assessment of anterior chamber parameters in pigmentary glaucoma using slit-lamp optical coherence tomography.* European journal of ophthalmology, 2009. **20**(4): p. 702-707.
65. Li, H., et al., *Comparative study of central corneal thickness measurement with slit-lamp optical coherence tomography and visante optical coherence tomography.* Ophthalmology, 2008. **115**(5): p. 796-801. e2.
66. Fontana, S.T. and R.F. Brubaker, *VOlume and depth of the anterior chamber in the normal aging human eye.* Archives of Ophthalmology, 1980. **98**(10): p. 1803-1808.
67. Lee, D.A., R.F. Brubaker, and D.M. Ilstrup, *ANterior chamber dimensions in patients with narrow angles and angle-closure glaucoma.* Archives of Ophthalmology, 1984. **102**(1): p. 46-50.
68. Forte, R., et al., *Comparison of time domain Stratus OCT and spectral domain SLO/OCT for assessment of macular thickness and volume.* Eye, 2008. **23**(11): p. 2071-2078.
69. Rodrigues, E.B., M. Johanson, and F.M. Penha, *Anterior segment tomography with the cirrus optical coherence tomography.* Journal of ophthalmology, 2012. **2012**.
70. Jing, T., P. Marziliano, and H.-T. Wong. *Automatic detection of Schwalbe's line in the anterior chamber angle of the eye using HD-OCT images*. in *Engineering in Medicine and Biology Society (EMBC), 2010 Annual International Conference of the IEEE*. 2010. IEEE.
71. Wong, H.-T., et al., *High-definition optical coherence tomography imaging of the iridocorneal angle of the eye.* Archives of ophthalmology, 2009. **127**(3): p. 256.

72. Ho, S.-W., et al., *Swept source optical coherence tomography measurement of the iris–trabecular contact (ITC) index: a new parameter for angle closure.* Graefe's Archive for Clinical and Experimental Ophthalmology, 2013. **251**(4): p. 1205-1211.
73. Liu, S., et al., *Anterior chamber angle imaging with swept-source optical coherence tomography: an investigation on variability of angle measurement.* Investigative ophthalmology & visual science, 2011. **52**(12): p. 8598-8603.
74. Kruger, R.A., *Photoacoustic ultrasound.* Medical Physics-New York-Institute of Physics, 1994. **21**(1): p. 127-132.
75. Xu, M. and L.V. Wang, *Photoacoustic imaging in biomedicine.* Review of scientific instruments, 2006. **77**(4): p. 041101-041101-22.
76. Silverman, R.H., et al. *Fine-resolution photoacoustic imaging of the eye*. in *BiOS*. 2010. International Society for Optics and Photonics.
77. Bassukas, I., et al., *Melanin absorption spectroscopy: new method for noninvasive skin investigation and melanoma detection.* Journal of Biomedical Optics, 2008. **13**(1): p. 014017-014017-8.
78. Silverman, R.H., et al., *High-resolution photoacoustic imaging of ocular tissues.* Ultrasound in medicine & biology, 2010. **36**(5): p. 733-742.
79. de la Zerda, A., et al., *Photoacoustic ocular imaging.* Optics Letters, 2010. **35**(3): p. 270-272.
80. Cairns, G. and C.N. McGhee, *Orbscan computerized topography: attributes, applications, and limitations.* Journal of Cataract & Refractive Surgery, 2005. **31**(1): p. 205-220.
81. Karpecki, P., *Bausch & Lomb Orbscan II/IIz anterior segment analysis system.* Corneal Topography in the wavefront Era: A Guide for Clinical Application, Slack Inc., Thorofare, 2006: p. 191-206.
82. Snook, R.K., *Pachymetry and true topography using the Orbscan system.* Corneal Topography: The State of the Art. Thorofare, NJ: SLACK Inc, 1995: p. 89-103.
83. Buehl, W., et al., *Comparison of three methods of measuring corneal thickness and anterior chamber depth.* American journal of ophthalmology, 2006. **141**(1): p. 7-12. e1.
84. Keller, H.E., *Objective Lenses for Confocal Microscopy*, in *Handbook Of Biological Confocal Microscopy*, J.B. Pawley, Editor. 2006, Springer US. p. 145-161.
85. Kino, G.S. and T.R. Corle, *Confocal scanning optical microscopy and related imaging systems*. 1996: Academic Press.
86. Wilson, T. and C. Sheppard, *Theory and practice of scanning optical microscopy*. London: Academic Press,| c1984, 1984. **1**.
87. Minsky, M., *Microscopy apparatus*. 1961, Google Patents.
88. Siedentopf, H. and R. Zsigmondy, *Uber Sichtbarmachung und Größenbestimmung ultramikoskopischer Teilchen, mit besonderer Anwendung auf Goldrubingläser.* Annalen der Physik, 1902. **315**(1): p. 1-39.
89. Voie, A., D. Burns, and F. Spelman, *Orthogonal-plane fluorescence optical sectioning: Three-dimensional imaging of macroscopic biological specimens.* Journal of microscopy, 1993. **170**(3): p. 229-236.
90. Fuchs, E., et al., *Thin laser light sheet microscope for microbial oceanography.* Optics Express, 2002. **10**(2): p. 145-154.

91. Huisken, J., et al., *Optical sectioning deep inside live embryos by selective plane illumination microscopy.* Science, 2004. **305**(5686): p. 1007-1009.
92. Holekamp, T.F., D. Turaga, and T.E. Holy, *Fast three-dimensional fluorescence imaging of activity in neural populations by objective-coupled planar illumination microscopy.* Neuron, 2008. **57**(5): p. 661-672.
93. Dunsby, C., *Optically sectioned imaging by oblique plane microscopy.* Optics express, 2008. **16**(25): p. 20306-20316.
94. Keller, P.J., et al., *Reconstruction of zebrafish early embryonic development by scanned light sheet microscopy.* science, 2008. **322**(5904): p. 1065-1069.
95. Spalteholz, W., *Über das Durchsichtigmachen von menschlichen und tierischen Präparaten: nebst Anhang, Über Knochenfärbung*. 1911: Verlag von S. Hirzel.
96. Kalender, W.A., *X-ray computed tomography.* Physics in medicine and biology, 2006. **51**(13): p. R29.
97. Lauterbur, P.C., *Image formation by induced local interactions: examples employing nuclear magnetic resonance.* Nature, 1973. **242**(5394): p. 190-191.
98. Denk, W., J.H. Strickler, and W.W. Webb, *Two-photon laser scanning fluorescence microscopy.* Science, 1990. **248**(4951): p. 73-76.
99. Siegman, A.E., *Lasers University Science Books.* Mill Valley, CA, 1986. **37**.
100. Engelbrecht, C.J. and E.H. Stelzer, *Resolution enhancement in a light-sheet-based microscope (SPIM).* Optics letters, 2006. **31**(10): p. 1477-1479.
101. Krzic, U., et al., *Multiview light-sheet microscope for rapid in toto imaging.* Nature methods, 2012. **9**(7): p. 730-733.
102. Tomer, R., et al., *Quantitative high-speed imaging of entire developing embryos with simultaneous multiview light-sheet microscopy.* Nature methods, 2012. **9**(7): p. 755-763.
103. Durnin, J., J. Miceli Jr, and J. Eberly, *Diffraction-free beams.* Physical review letters, 1987. **58**(15): p. 1499.
104. Durnin, J., *Exact solutions for nondiffracting beams. I. The scalar theory.* JOSA A, 1987. **4**(4): p. 651-654.
105. Masihzadeh, O., et al., *Direct trabecular meshwork imaging in porcine eyes through multiphoton gonioscopy.* Journal of biomedical optics, 2013. **18**(3): p. 036009-036009.
106. Kashima, S. and Y. Kishi, *Laser scanning microscope*. 2000, Google Patents.
107. Sheppard, C.J.R. and D.M. Shotton, *Confocal laser scanning microscopy*. 1997: BIOS Scientific Publishers.
108. Moreno, I., M. Avendaño-Alejo, and R.I. Tzonchev, *Designing light-emitting diode arrays for uniform near-field irradiance.* Applied optics, 2006. **45**(10): p. 2265-2272.
109. Qin, Z., et al., *Analysis of condition for uniform lighting generated by array of light emitting diodes with large view angle.* Optics express, 2010. **18**(16): p. 17460-17476.
110. Moreno, I. and R. Ivanov, *Uniform illumination of distant targets using a spherical light-emitting diode array.* Optical Engineering, 2007. **46**(3): p. 033001-033001-7.
111. Reynolds, G.O., et al., *The new physical optics notebook: tutorials in Fourier optics*. Vol. 61. 1989: SPIE Optical Engineering Press New York.
112. Yoshizawa, T., *Handbook of optical metrology: Principles and Applications*. 2015: CRC Press.

113. Protection, I.C.o.N.-I.R., *Guidelines on limits of exposure to broad-band incoherent optical radiation (0.38 to 3 µm).* Health Phys, 1997. **73**(3): p. 539-554.
114. Ham, W.T., et al., *Action spectrum for retinal injury from near-ultraviolet radiation in the aphakic monkey.* American journal of ophthalmology, 1982. **93**(3): p. 299-306.
115. Ham, W.T., H.A. Mueller, and D.H. Sliney, *Retinal sensitivity to damage from short wavelength light.* Nature, 1976. **260**(5547): p. 153-155.
116. Sliney, D., et al., *Adjustment of guidelines for exposure of the eye to optical radiation from ocular instruments: statement from a task group of the International Commission on Non-Ionizing Radiation Protection (ICNIRP).* Applied optics, 2005. **44**(11): p. 2162-2176.
117. Heitz, R. and J. Enoch, *Leonardo da Vinci: An assessment on his discourses on image formation in the eye.* Advances in Diagnostic Visual Optics, 1987: p. 19-26.
118. Stapleton, F., et al., *The incidence of contact lens–related microbial keratitis in Australia.* Ophthalmology, 2008. **115**(10): p. 1655-1662.
119. Dart, J., et al., *Risk factors for microbial keratitis with contemporary contact lenses: a case-control study.* Ophthalmology, 2008. **115**(10): p. 1647-1654. e3.
120. Moezzi, A., et al., *Open-eye corneal swelling with etafilcon a daily disposable hydrogel contact lenses compared to no lens wear.* Contact Lens and Anterior Eye, 2015(38): p. e22-e23.
121. Chalmers, R.L., et al., *Rates of Adverse Events With Hydrogel and Silicone Hydrogel Daily Disposable Lenses in a Large Postmarket Surveillance Registry: The TEMPO RegistryAEs With Hydrogel and Silicone Hydrogel DD Lenses.* Investigative Ophthalmology & Visual Science, 2015. **56**(1): p. 654-663.
122. Ruiz-Ederra, J., et al., *The pig eye as a novel model of glaucoma.* Experimental eye research, 2005. **81**(5): p. 561-569.
123. Fernandez-Bueno, I., et al., *Müller and macrophage-like cell interactions in an organotypic culture of porcine neuroretina.* 2008.
124. Kolker, A.E., et al., *The development of glaucoma in rabbits.* Investigative Ophthalmology & Visual Science, 1963. **2**(4): p. 316-321.
125. Dawson, W.W., et al., *Primary open angle glaucomas in the rhesus monkey.* British journal of ophthalmology, 1993. **77**(5): p. 302-310.
126. A Bouhenni, R., et al., *Animal models of glaucoma.* BioMed Research International, 2012. **2012**.
127. Tripathi, R.C., *Ultrastructure of the exit pathway of the aqueous in lower mammals:(A preliminary report on the "angular aqueous plexus").* Experimental eye research, 1971. **12**(3): p. 311IN23313-312IN28314.
128. Iester, M., et al., *Diagnosis of glaucoma.* 2013.
129. Koo, B.S., *Diagnosis of glaucoma.* Journal of the Korean Ophthalmological Society, 1974. **15**(1): p. 77-82.
130. Quigley, H.A., et al., *An evaluation of optic disc and nerve fiber layer examinations in monitoring progression of early glaucoma damage.* Ophthalmology, 1992. **99**(1): p. 19-28.

131. Shinoj, V., et al., *Progress in anterior chamber angle imaging for glaucoma risk prediction–A review on clinical equipment, practice and research.* Medical Engineering & Physics, 2016. **38**(12): p. 1383-1391.
132. Baskaran, M., et al., *Comparison of EyeCam and anterior segment optical coherence tomography in detecting angle closure.* Acta ophthalmologica, 2012. **90**(8): p. e621-e625.
133. Wu, C., R.A. Petersen, and D.K. VanderVeen, *RetCam imaging for retinopathy of prematurity screening.* Journal of American Association for Pediatric Ophthalmology and Strabismus, 2006. **10**(2): p. 107-111.
134. Perera, S.A., et al., *Use of EyeCam for imaging the anterior chamber angle.* Investigative ophthalmology & visual science, 2010. **51**(6): p. 2993-2997.
135. Ishikawa, H., et al., *Inadvertent corneal indentation can cause artifactitious widening of the iridocorneal angle on ultrasound biomicroscopy.* Ophthalmic Surgery, Lasers and Imaging Retina, 2000. **31**(4): p. 342-345.
136. Andersson-Engels, S., et al., *In vivo fluorescence imaging for tissue diagnostics.* Physics in medicine and biology, 1997. **42**(5): p. 815.
137. Engelbrecht, C.J., et al., *Ultra-compact fiber-optic two-photon microscope for functional fluorescence imaging in vivo.* Optics express, 2008. **16**(8): p. 5556-5564.
138. Reynaud, E.G., et al., *Light sheet based fluorescence microscopy: More dimensions, more photons, and less photodamage.* HFSP journal, 2008. **2**(5): p. 266-275.
139. Mertz, J. and J. Kim, *Scanning light-sheet microscopy in the whole mouse brain with HiLo background rejection.* Journal of biomedical optics, 2010. **15**(1): p. 016027-016027-7.
140. Baumgart, E. and U. Kubitscheck, *Scanned light sheet microscopy with confocal slit detection.* Optics Express, 2012. **20**(19): p. 21805-21814.
141. Lee, K.-S. and J.P. Rolland, *Bessel beam spectral-domain high-resolution optical coherence tomography with micro-optic axicon providing extended focusing range.* Optics letters, 2008. **33**(15): p. 1696-1698.
142. Olarte, O.E., et al., *Image formation by linear and nonlinear digital scanned light-sheet fluorescence microscopy with Gaussian and Bessel beam profiles.* Biomedical optics express, 2012. **3**(7): p. 1492-1505.
143. Delori, F.C., R.H. Webb, and D.H. Sliney, *Maximum permissible exposures for ocular safety (ANSI 2000), with emphasis on ophthalmic devices.* JOSA A, 2007. **24**(5): p. 1250-1265.
144. Herman, R. and T. Wiggins, *Production and uses of diffractionless beams.* JOSA A, 1991. **8**(6): p. 932-942.
145. Arimoto, R., et al., *Imaging properties of axicon in a scanning optical system.* Applied optics, 1992. **31**(31): p. 6653-6657.
146. Verveer, P.J., et al., *High-resolution three-dimensional imaging of large specimens with light sheetâ€“based microscopy.* Nature methods, 2007. **4**(4): p. 311-313.
147. Fahrbach, F.O., P. Simon, and A. Rohrbach, *Microscopy with self-reconstructing beams.* Nature Photonics, 2010. **4**(11): p. 780-785.
148. Fahrbach, F.O. and A. Rohrbach, *Propagation stability of self-reconstructing Bessel beams enables contrast-enhanced imaging in thick media.* Nature communications, 2012. **3**: p. 632.

149. Ahrens, M.B., et al., *Whole-brain functional imaging at cellular resolution using light-sheet microscopy.* Nature methods. **10**(5): p. 413-420.
150. Weisbecker, C., F. Fraunfelder, and R. Tipperman, *Physician's Desk Reference for Ophthalmic Medicines*. 2001, Montvale, NJ: Medical Economics.
151. Wolfe, D.R., *Fluorescein angiography basic science and engineering.* Ophthalmology, 1986. **93**(12): p. 1617-1620.
152. Maurice, D. and A. Giardini, *A simple optical apparatus for measuring the corneal thickness, and the average thickness of the human cornea.* The British journal of ophthalmology, 1951. **35**(3): p. 169.
153. Born, M. and E. Wolf, *Principles of optics: electromagnetic theory of propagation, interference and diffraction of light*. 2013: Elsevier.
154. Maitland, K.C., et al., *Single fiber confocal microscope with a two-axis gimbaled MEMS scanner for cellular imaging.* Optics express, 2006. **14**(19): p. 8604-8612.
155. Standard, M., *Military Standard Photograph Lenses*. 1959, MIL-STD-150A.
156. Faber, C., et al., *Orthotopic porcine corneal xenotransplantation using a human graft.* Acta ophthalmologica, 2009. **87**(8): p. 917-919.
157. Wong, K.-H., et al., *Changes in spherical aberration after lens refilling with a silicone oil.* Investigative ophthalmology & visual science, 2007. **48**(3): p. 1261-1267.
158. Sanchez, I., et al., *The parameters of the porcine eyeball.* Graefe's Archive for Clinical and Experimental Ophthalmology, 2011. **249**(4): p. 475-482.
159. Bozkir, G., et al., *Measurements of axial length and radius of corneal curvature in the rabbit eye.* Acta Medica Okayama, 1997. **51**(1): p. 9-11.
160. Yüksel, H., et al., *Anterior segment parameters of rabbits with rotating Scheimpflug camera.* Veterinary ophthalmology, 2014.
161. Hayashi, S., T. Osawa, and K. Tohyama, *Comparative observations on corneas, with special reference to Bowman's layer and Descemet's membrane in mammals and amphibians.* Journal of morphology, 2002. **254**(3): p. 247-258.
162. Ojeda, J.L., J.A. Ventosa, and S. Piedra, *The three-dimensional microanatomy of the rabbit and human cornea. A chemical and mechanical microdissection-SEM approach.* Journal of Anatomy, 2001. **199**(5): p. 567-576.
163. Li, H., et al., *Anterior Segment Optical Coherence Tomography and its Clinical Applications in Glaucoma.* Journal of Current Glaucoma Practice, 2012. **6**(2): p. 68-74.
164. Radhakrishnan, S., et al., *Comparison of optical coherence tomography and ultrasound biomicroscopy for detection of narrow anterior chamber angles.* Archives of Ophthalmology, 2005. **123**(8): p. 1053.
165. Protection, I.C.o.N.-I.R. and I.C.o.N.-I.R. Protection, *Guidelines on limits of exposure to broad-band incoherent optical radiation (0.38 to 3 µm).* Health Phys, 1997. **73**(3): p. 539-554.
166. Cheng, P. and A. Kriete, *Image contrast in confocal light microscopy*, in *Handbook of biological confocal microscopy*. 1995, Springer. p. 281-310.
167. Rüfer, F., A. Schröder, and C. Erb, *White-to-white corneal diameter: normal values in healthy humans obtained with the Orbscan II topography system.* Cornea, 2005. **24**(3): p. 259-261.

168. Richardson, T.M., B.T. Hutchinson, and W.M. Grant, *The outflow tract in pigmentary glaucoma: a light and electron microscopic study.* Archives of Ophthalmology, 1977. **95**(6): p. 1015-1025.
169. Kupfer, C., T. Kuwabara, and M. Kaiser-Kupfer, *The histopathology of pigmentary dispersion syndrome with glaucoma.* American journal of ophthalmology, 1975. **80**(5): p. 857-862.
170. Sugar, H.S., *Pigmentary glaucoma: a 25-year review.* American journal of ophthalmology, 1966. **62**(3): p. 499-507.
171. Kinori, M., et al., *A novel method for quantifying the amount of trabecular meshwork pigment in glaucomatous and nonglaucomatous eyes.* Journal of glaucoma, 2014. **23**(1): p. e13-e17.
172. Nakamura, Y., et al., *Assessment of chamber angle pigmentation during longterm latanoprost treatment for open-angle glaucoma.* Acta Ophthalmologica Scandinavica, 2004. **82**(2): p. 158-160.
173. Chun, Y.S., et al., *Iris and trabecular meshwork pigment changes after posterior chamber phakic intraocular lens implantation.* Journal of Cataract & Refractive Surgery, 2006. **32**(9): p. 1452-1458.
174. Ahluwalia, B., X. Yuan, and S. Tao, *Generation of self-imaged optical bottle beams.* Optics communications, 2004. **238**(1): p. 177-184.
175. ChJ, P., K. Harasiewicz, and F. FSt, *Ultrasound biomicroscopy of anterior segment structures in normal and glaucomatous eyes.* Am J Ophthalmol, 1992. **113**(4): p. 381-389.
176. Ishikawa, H., J.M. Liebmann, and R. Ritch, *Quantitative assessment of the anterior segment using ultrasound biomicroscopy.* Current opinion in ophthalmology, 2000. **11**(2): p. 133-139.
177. Snoeyink, C., *Imaging performance of Bessel beam microscopy.* Optics letters, 2013. **38**(14): p. 2550-2553.
178. Navarro, R., J. Santamaría, and J. Bescós, *Accommodation-dependent model of the human eye with aspherics.* JOSA A, 1985. **2**(8): p. 1273-1280.
179. Howcroft, M.J. and J.A. Parker, *Aspheric curvatures for the human lens.* Vision Research, 1977. **17**(10): p. 1217-1223.